

The ubiquity of variable radio emission and spin-down rates in pulsars

M. E. Lower,^{1,2}★ A. Karastergiou,^{3,4} S. Johnston², P. R. Brook,⁵ S. Dai,² M. Kerr,⁶ R. N. Manchester,² L. S. Oswald,⁷ R. M. Shannon,^{1,8} C. Sobey,^{9,10} and P. Weltevrede¹¹

¹Centre for Astrophysics and Supercomputing, Swinburne University of Technology, PO Box 218, Hawthorn, VIC 3122, Australia

²Australia Telescope National Facility, CSIRO, Space and Astronomy, PO Box 76, Epping, NSW 1710, Australia

³Department of Astrophysics, University of Oxford, Denys Wilkinson Building, Keble Road, Oxford OX1 3RH, UK

⁴Department of Physics and Electronics, Rhodes University, PO Box 94, Grahamstown 6140, South Africa

⁵Institute for Gravitational Wave Astronomy and School of Physics and Astronomy, University of Birmingham, Edgbaston, Birmingham B15 2TT, UK

⁶Space Science Division, Naval Research Laboratory, Washington, DC 20375, USA

⁷School of Physics and Astronomy, University of Southampton, Southampton SO17 1BJ, UK

⁸OzGrav: The ARC Centre of Excellence for Gravitational-wave Discovery

⁹SKAO, ARRC Building, 26 Dick Perry Avenue, Kensington, WA 6151, Australia

¹⁰CSIRO, Space and Astronomy, PO Box 1130 Bentley, WA 6102, Australia

¹¹Jodrell Bank Centre for Astrophysics, The University of Manchester, Alan Turing Building, Manchester, M13 9PL, United Kingdom

Accepted XXXX. Received YYYY; in original form ZZZZ

ABSTRACT

Pulsars are often lauded for their (relative) rotational and radio emission stability over long time scales. However, long-term observing programmes are identifying an increasing number of pulsars that deviate from this preconceived notion. Using Gaussian process regression and Bayesian inference techniques, we investigated the emission and rotational stability of 259 isolated radio pulsars that have been monitored using Murriyang, the Parkes 64 m radio telescope, over the past three decades. We found that 238 pulsars display significant variability in their spin-down rates, 52 of which also exhibit changes in profile shape. Including 23 known state-switching pulsars, this represents the largest catalogue of variable pulsars identified to date and indicates that these behaviours are ubiquitous among the wider population. The intensity of spin-down fluctuations positively scales with increasing pulsar spin-down rate, with only a marginal dependence on spin-frequency. This may have substantial implications for ongoing searches for gravitational waves in the ensemble timing of millisecond pulsars. We also discuss challenges in explaining the physical origins of quasi-periodic and transient profile/spin-down variations detected among a subset of our pulsars.

Key words: radiation mechanisms: non-thermal – stars: neutron – pulsars: general

1 INTRODUCTION

The highly predictable, periodic nature of radio pulsars makes them excellent tools for studying a variety of astrophysical phenomena. These include measuring fluctuations in the electron column density and turbulence of the interstellar medium within our Galaxy (e.g. Petroff et al. 2013), testing theories of gravity (Freire & Wex 2024), and the direct detection of nanohertz-frequency gravitational waves (Sazhin 1978; Detweiler 1979). The key to the success of such studies are the relative stability of both the pulsar emission mechanism and the rate at which pulsars spin down. While individual pulses from a given pulsar can vary wildly in intensity and shape (e.g. Johnston et al. 2001), integrating over many rotations will typically return an average profile that is more or less constant from one observation to the next. Yet long-term monitoring programmes and observations with newer, more sensitive instruments have revealed a growing number of cases that deviate from ideal clock assumptions.

Mode or state switching between two or more discrete radio emission states was identified soon after the discovery of the first pulsars,

manifesting as changes in the observed intensity, or shape or position in pulse longitude of the pulse profile components (see Backer 1970b,c; Lyne 1971). It is a broadband phenomenon, having been detected both at radio and X-ray wavelengths (Hermsen et al. 2013, 2017, 2018), and takes place over a wide range of timescales. This can be as short as one or several rotations of a neutron star, or slow secular variations that take place over many months or years. In some cases the emission appears to briefly switch off and back on again (nulls; Backer 1970a) or remain off for extended periods of time (intermittency; Kramer et al. 2006). Long-term monitoring experiments found that the timing of some pulsars displayed quasi-periodic processes with a range of apparent periods (e.g. Cordes & Greenstein 1981; Cordes & Downs 1985; Stairs et al. 2000). Fluctuations in both radio emission and spin-down rate were eventually linked, initially through observations of the intermittent pulsar PSR B1931+24 (Kramer et al. 2006), and later through increasingly large samples of pulsars that switch between two or more quasi-stable spin-down levels or undergo transient spin-down events (Kramer et al. 2006; Hobbs et al. 2010; Lyne et al. 2010; Brook et al. 2014, 2016; Shaw et al. 2022). Other studies have revealed pulsars with variations in either spin-down or pulse shape (and even polarization) that appear

★ E-mail: mlower@swin.edu.au

uncorrelated with one another (Brook et al. 2016; Shaw et al. 2022; Basu et al. 2024), though this may be a selection effect imparted by limited telescope sensitivity and observing cadence.

Exactly what mechanism drives these behaviours, and whether they originate from the interior dynamics or magnetospheric fluctuations of neutron stars, is presently unknown. Free precession of a non-axisymmetric neutron star was once a popular hypothesis for explaining highly periodic changes in pulsar profile shapes and spin-down rates (Stairs et al. 2000). However, the discovery that such spin-down rate changes were linked to short-term emission variations has cast doubt on whether free precession is the true, or only, mechanism behind these behaviours (Lyne et al. 2010; Jones 2012; Kerr et al. 2016; Stairs et al. 2019). Simultaneous emission switching at radio and X-ray wavelengths point toward a magnetospheric reconfiguration being responsible for at least some of the mode-switching behaviour (Hermesen et al. 2013). Emission and spin-down variations that seemingly coincided with glitches in several pulsars (e.g. Weltevrede et al. 2011; Keith et al. 2013) may point to crustal events such as starquakes that couple the internal dynamics of the neutron star to the magnetosphere (Akbal et al. 2015; Yuan et al. 2021). Indeed, the 2016 glitch in the Vela pulsar (PSR J0835–4510/B0833–45) was associated with a short-lived quenching of its radio emission (Palfreyman et al. 2018), speculated to be due to a quake-induced magnetic disturbance (Bransgrove et al. 2020). External triggers such as interactions between pulsars and minor bodies are another popular hypothesis. These include interactions with individual in-falling asteroids (Brook et al. 2014), debris disks (Li 2006; Shannon et al. 2013; Jennings et al. 2020b), and impacts from interstellar objects (Pham et al. 2024). In such cases, the ionised remains of a wayward minor body alter the plasma content of the pulsar magnetosphere, subsequently enhancing or attenuating the radio emission and altering the spin-down state. Many previous attempts to explain pulsar variability focussed on either individual objects or small samples with similar characteristics (e.g., Brook et al. 2014, 2016; Lower et al. 2023; Basu et al. 2024). Understanding whether one or more of these processes are responsible for these profile/spin-down variations requires population-level studies of a large ensemble of pulsars.

Determining the prevalence of pulsar rotation/emission state changes across the population is vital to building a complete picture of the processes that contribute to the overall noise budget of a pulsar. Knowing how these behaviours scale as functions of spin frequency and spin-down rate is particularly important for pulsar timing array experiments that utilise an ensemble of millisecond pulsars to search for nanohertz-frequency gravitational waves (Manchester et al. 2013; Manchester & IPTA 2013; Kramer & Champion 2013; McLaughlin 2013). Even the most stable millisecond pulsars have been found to display profile shape variations and emission state switching that can hamper such experiments (Shannon et al. 2016; Brook et al. 2018; Goncharov et al. 2021; Miles et al. 2022; Nathan et al. 2023; Jennings et al. 2024). It may also bring us a step closer to determining the origins of unexpected time-dependent changes in the common noise process seen by pulsar timing array experiments (see Reardon et al. 2023).

In this work, we present the largest sample of pulsars found to display emission and spin-down variations to date, by applying the Gaussian process regression techniques of (Brook et al. 2016, 2018) to observations collected over the past three decades by Murriyang, the CSIRO Parkes 64 m radio telescope. In Section 2 we briefly describe the data collection and reduction process. Section 3 details the methodologies used for obtaining updated pulsar timing solutions and modelling the pulse profile shape and spin-down variations, the results of which are presented in Section 4. We discuss how these

effects vary across the population and the implications for pulsar timing array experiments in Section 5. Finally, we summarise the results and make concluding statements in Section 6.

2 OBSERVATIONS AND DATA REDUCTION

The pulsar data analysed in this work were collected using Murriyang between 2007–2023 under the ‘young’ pulsar timing (P574) programme (Weltevrede et al. 2010; Johnston et al. 2021). Our sample covers 259 isolated, non-recycled, rotation-powered pulsars with characteristic ages ranging from 1.6 kyr (PSR J1513–5908) to 0.4 Gyr (PSR J0820–4114). In Figure 1 we show the positions of our pulsar sample in period-period-derivative space alongside those of the broader ATNF Pulsar Catalogue (Manchester et al. 2005)¹. Note that there is a slight bias towards pulsars with high rotational kinetic energy loss rates due to the programme’s continued support of the Fermi mission (Smith et al. 2023). Pulsar observations were undertaken with the 10/50², 20-cm Multibeam, H-OH and Ultra-Wideband Low (UWL) receivers (Granet et al. 2001; Staveley-Smith et al. 1996; Granet et al. 2011; Hobbs et al. 2020) and saved to PSRFITS format archives (Hotan et al. 2004; van Straten et al. 2012). Details of the specific observing set-up, radio-frequency excision, and calibration steps can be found in Namkham et al. (2019); Parthasarathy et al. (2019); Lower et al. (2021); Johnston et al. (2021). Where possible, we also made use of extended timing datasets collected using legacy signal processors going back to the 1990s, which are available in the Parkes Observatory Pulsar Data Archive (Hobbs et al. 2011)³.

Pulse times of arrival (ToAs) were obtained following the prescription outlined previously in Parthasarathy et al. (2019), Lower et al. (2021) and Lower et al. (2023). We averaged the individual observations in time and frequency to form one-dimensional pulse profiles, which were then cross-correlated against a noise-free template using the Fourier-domain Monte Carlo (FDM) method built into the PAT tool in PSRCHIVE (Hotan et al. 2004; van Straten et al. 2012). Note that we employed observing band-specific templates for each pulsar.

3 METHODS

3.1 Updated pulsar timing

A substantial fraction of the pulsars required updates to their timing models over those published in the ATNF Pulsar Catalogue. Phase coherent solutions were derived following the manual procedures outlined in Parthasarathy et al. (2019) and Lower et al. (2021), where pulsar positions, proper motions, spin frequency (ν), spin-down rate ($\dot{\nu}$) and on occasion, second spin-frequency derivative ($\ddot{\nu}$), were re-fit using a combination of TEMPO2 and TEMPONEST (Hobbs et al. 2006; Lentati et al. 2014). The majority of pulsars that required inclusion of $\ddot{\nu}$ were those previously studied in Parthasarathy et al. (2020) and Lower et al. (2021). Glitch events were identified by eye as discontinuities or sharp features in the timing residuals. These were corrected for by fitting the corresponding changes in ν and $\dot{\nu}$ using TEMPO2. Obtaining accurate measurements of the recovery parameters is challenging and imperfectly removed recovery signals will introduce unwanted artefacts in our spin-down analysis. A detailed analysis of the new glitch events and overall updates to the timing of

¹ <https://www.atnf.csiro.au/research/pulsar/psrcat/>

² Later re-tuned to cover the 40-cm band due to increased interference.

³ <https://data.csiro.au/domain/atnf>

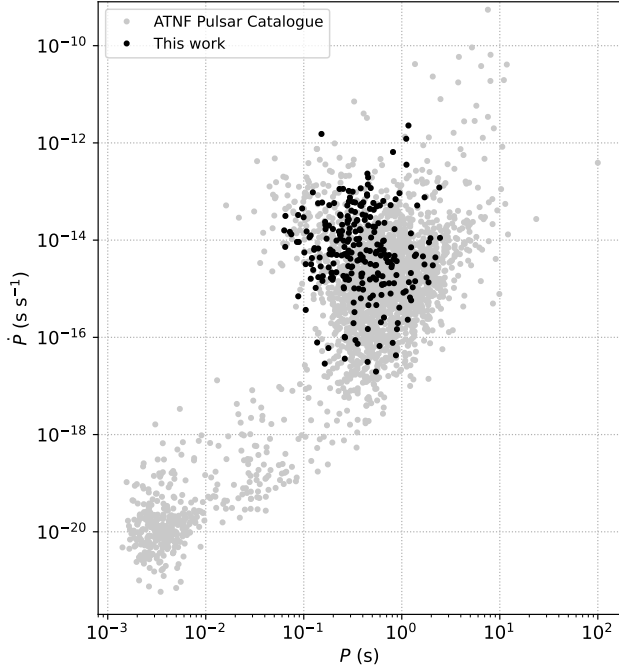


Figure 1. A pulsar period (P) and period-derivative (\dot{P}) diagram, where the pulsars sample analysed in this work are highlighted by black circles. Light-grey circles indicate all known pulsars published in v2.5.1 of the ATNF Pulsar Catalogue.

these pulsars is beyond the scope of this work, and will be reported elsewhere. Once a coherent solution was obtained, we then applied pulse numbering to the ToAs to maintain an accurate record of every single rotation over our timing baseline. In Figure 2 we show the corresponding timing residuals for our final sample of 259 pulsars.

3.2 Profile variability maps

In order to model the observed variations in the pulsar profiles and spin-down rates, we followed the general methodology devised by Brook et al. (2016). To detect and then study changes in the radio profile shape, we created profile variability maps that display variations in profile intensity as functions of rotational phase and observation date. Only the total intensity radio profiles collected by the Parkes Multibeam, H-OH and 1216–1600 MHz UWL subband were used in the shape variation analysis. Observations that were visually affected by residual RFI, instrumental artefacts, or displayed an anomalously low signal-to-noise (S/N) ratio were manually flagged and excluded. As in Lower et al. (2023), we performed an initial coarse alignment of the profiles by maximising the correlation between each observation with the highest S/N profile. The alignment was then refined using the iterative scaling and shifting approach outlined in Brook et al. (2018). We created standard templates for each pulsar by computing the median normalised flux within each phase bin, which were then subtracted from our observations to produce profile residuals. These profile residuals were then fitted with non-parametric models on a per phase bin basis via Gaussian process regression to produce profile variability maps. Variability maps where the absolute peak phase-bin standard deviation ($\max|\sigma_{\text{prof}}|$) was greater than three times the median off-pulse root-mean-square often indicated the presence of substantial profile shape variability above random noise fluctuations in the data. However, this metric is sensitive to distortions in the data

caused by residual RFI, hence visual inspection of the variability maps and profiles was used to filter out these outliers. We also note that apparent shape changes due to the different central frequencies of the multibeam (2007–2016, 2017–2019), H-OH (2016–2017) and UWL (2019 onwards) receivers limits our sensitivity to more subtle temporal shape changes.

We made use of the Matérn and white noise kernels implemented in SCIKIT-LEARN (Pedregosa et al. 2011) for modelling the differences in profile shapes after subtracting a median template. This is the same kernel that was used by Shaw et al. (2022), which is better at capturing short-duration profile shape changes than the squared-exponential kernel. For the Matérn kernel, we used a positive covariance exponent of $\mu = 3/2$

$$C_{3/2}(t, t') = \sigma_f^2 \left(1 + \frac{\sqrt{3}|t - t'|}{\lambda} \right) \exp \left(- \frac{\sqrt{3}|t - t'|}{\lambda} \right), \quad (1)$$

where σ_f^2 is the maximum allowed covariance, $|t - t'|$ is the time separating two data points, and λ is the kernel length scale. We computed the optimal kernel hyperparameters using a maximum-likelihood approach where the kernel length scale was allowed to vary between $30 \text{ d} < \lambda < 300 \text{ d}$. An exception is PSR J1359–6038, which required the use of two separate kernels with respective length scales of $30 \text{ d} < \lambda_1 < 600 \text{ d}$ and $600 \text{ d} < \lambda_2 < 3000 \text{ d}$ to correctly capture the short and long-term profile variations displayed by this pulsar. In general, we found the SCIKIT-LEARN implementations of the Matérn and white noise kernels provided more accurate representations of the underlying profile variations in our pulsars when compared to a similar variant implemented in the GEORGE Python package (Ambikasaran et al. 2015). The latter would often miss rapid changes in the profile shape.

3.3 Modelling spin-down rate variations

Our approach to modelling the spin-down rates followed that of Shaw et al. (2022), where we used the GP_NUDOT.PY script in PULSARPVC⁴ to fit a squared exponential kernel to the timing residuals for each pulsar. Spin-down timeseries were then generated by taking the second derivative of the resulting model of the timing residuals. As with the profile variability, this made use of the Gaussian process regression functionality of SCIKIT-LEARN. Similar to the analyses of Brook et al. (2016) and Shaw et al. (2022), about half of our pulsars required the addition of a second squared exponential kernel to account for both long- and short-term variations. Several dozen pulsars in our sample displayed a sinusoidal signal with a 1-yr period in their resulting spin-down timeseries that resulted from small offsets from their assumed position on the sky. For some pulsars, this was corrected through updated timing model parameters obtained via TEMPO2 and TEMPO^{NEST}. Yet for others, a degeneracy between the annual sinusoid and quasi-periodic pulsar timing noise, combined with the limitations of the red power-law timing noise model in TEMPO^{NEST}⁵, prevented us from making such positional corrections for a substantial number of pulsars. To overcome this, we also conducted a set of Gaussian process regression fits that included a sinusoidal kernel with a fixed 1-yr period. In order to determine which pulsars had residuals best described by a one-kernel or two-kernel fit,

⁴ <https://gitlab.com/benjaminshaw/pulsarpvc>

⁵ Modelling of quasi-periodic and non-stationary timing behaviours as a red power-law process can result in biased measurements of the pulsar properties (cf. Keith & Ntzi 2023).

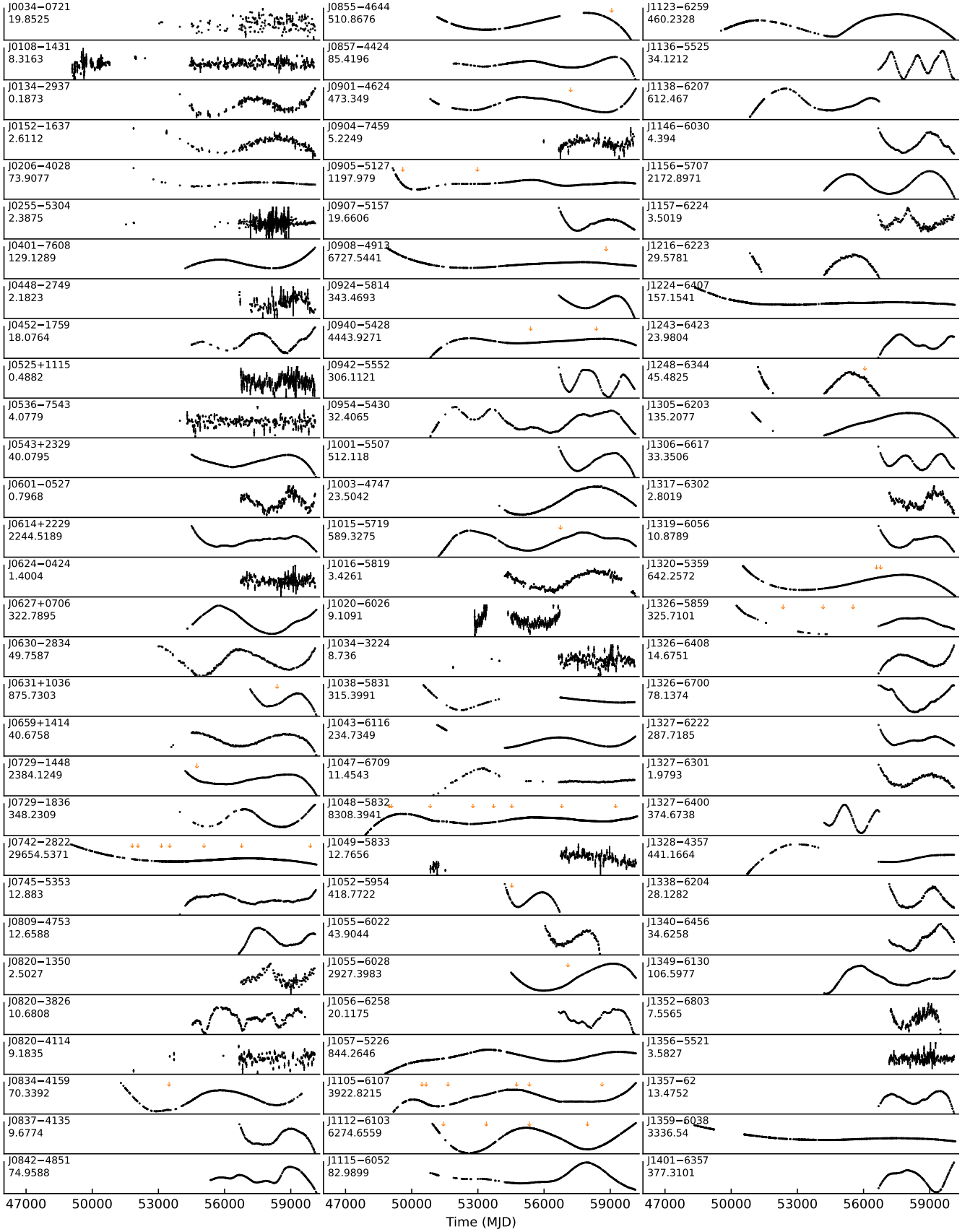


Figure 2. Timing residuals for all 259 pulsars after subtracting the best-fit timing model. Labels on the left-hand side of each panel indicates the pulsar J2000 name and the maximum-to-minimum range of the residuals in milliseconds. The downward pointing arrows indicate the epochs of detected glitches.

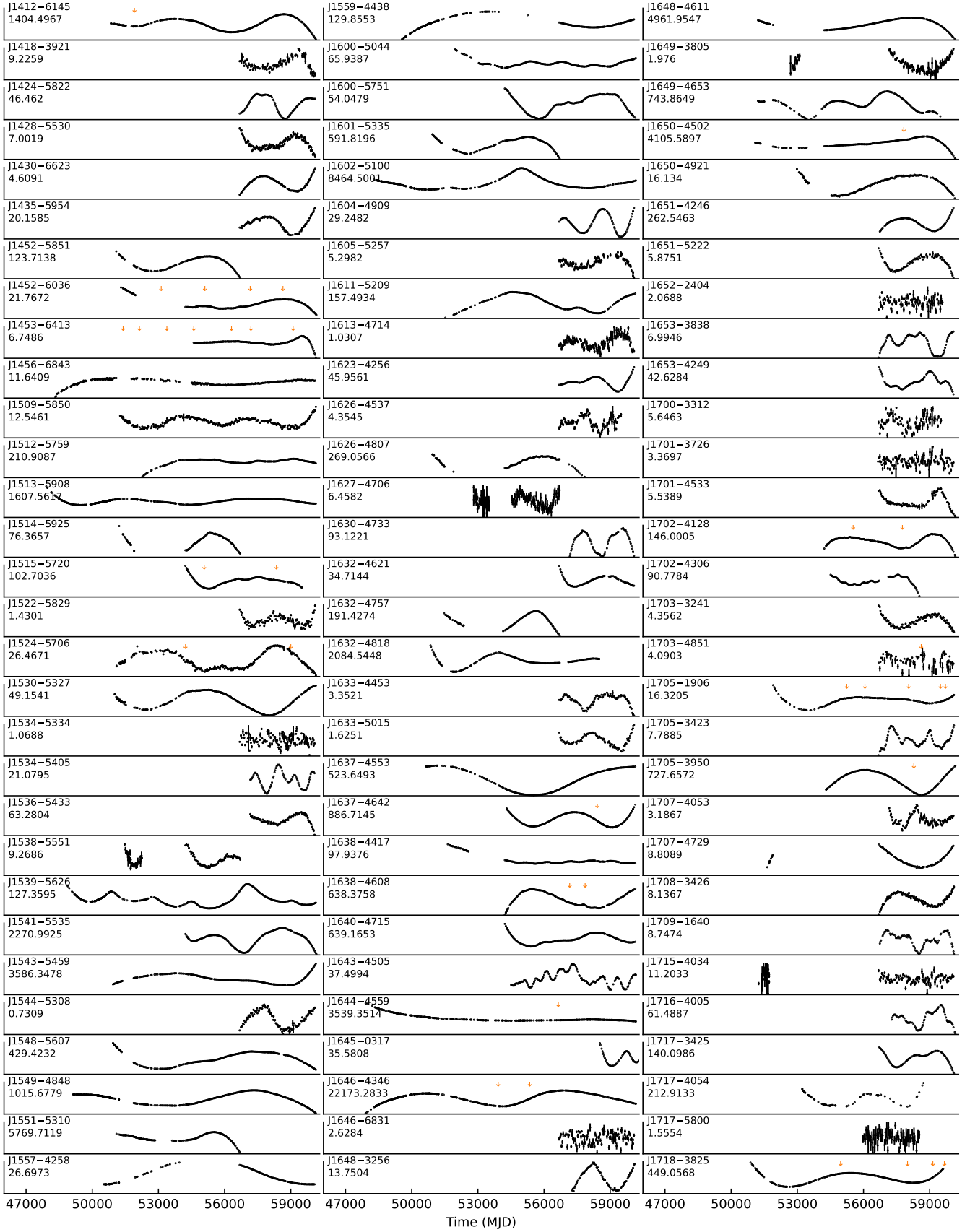
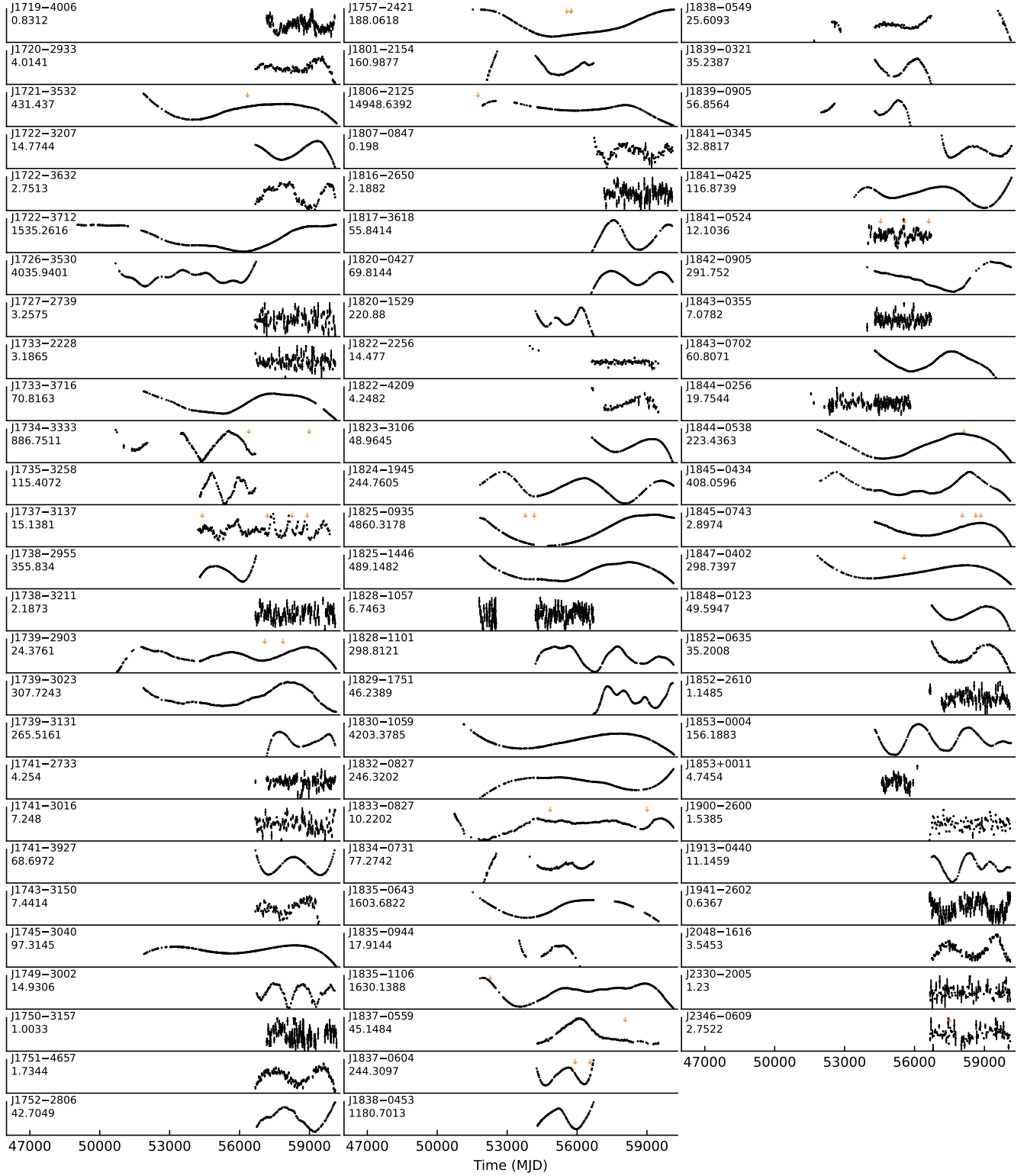


Figure 2 – continued

Figure 2 – *continued*

or required an annual sinusoid to correct for positional offsets, we compared the Bayesian information criterion (BIC) for each model. We first computed the BIC as

$$\text{BIC} = k \ln(N) - 2 \ln(\mathcal{L}_{\text{max}}), \quad (2)$$

where k is the number of free parameters in the model, N is the number of data points, and \mathcal{L}_{max} is the maximum likelihood value for the data given the model. A smaller BIC indicates a better match between the model and the data. The statistical significance for which one model is preferred over the other can be inferred from the differ-

ence in BICs for each model

$$\Delta\text{BIC} = \text{BIC}(\mathcal{M}_2) - \text{BIC}(\mathcal{M}_1), \quad (3)$$

where the subscripts 2 and 1 refer to the two models being compared. The second model is preferred when $\Delta\text{BIC} < 0$, while $\Delta\text{BIC} > 0$ favours the first model. This BIC-informed model selection approach worked well for most pulsars. However, on occasion we had to make by-eye judgement calls when one model visually matched the data better than another in spite of the reported BIC. This often occurred in instances where two squared exponential kernels and a sinusoidal kernel were needed to fit both the spin-down variations plus an incorrect position. After determining which set of kernels provided the best match to the timing residuals, continuous models of the pulsar spin-down rate were computed by taking the second derivative of the resulting non-parametric model (see Brook et al. 2016 for details).

Identifying spin-down variations through visual inspection of the $\dot{\nu}$ timeseries is relatively straightforward. However, to avoid biases in instances where the fluctuation amplitude is comparable to the derived uncertainties we computed a significance metric for each pulsar. This ‘ \mathcal{K} -metric’ is given by

$$\mathcal{K} = \frac{|\dot{\nu}_{\min}| - |\dot{\nu}_{\max}|}{2\sigma_{\dot{\nu}, \text{mean}}} \quad (4)$$

where $\dot{\nu}_{\min}$ and $\dot{\nu}_{\max}$ refer to the minimum and maximum inferred absolute spin-down rates derived from the Gaussian process regression, and $\sigma_{\dot{\nu}, \text{mean}}$ is the mean spin-down uncertainty computed via equations 9 and 10 of Brook et al. (2016). We used a threshold of $\mathcal{K} > 1$ for defining when a pulsar displayed substantial spin-down variability. To test the level of correlation between any observed variations in profile shape and spin-down rate, we computed the Spearman rank correlation coefficient between each phase bin of the profile variability map and $\dot{\nu}$ for time-lags ranging between \pm half the length of the per-pulsar observing span (Brook et al. 2016; Shaw et al. 2022; Lower et al. 2023).

4 RESULTS AND ANALYSIS

Our variability analysis identified 238 pulsars that displayed significant ($\mathcal{K} > 1$) changes in $\dot{\nu}$ over time. We present the resulting spin-down timeseries for the 238 variable $\dot{\nu}$ pulsars in Figure 3, and list the recovered Gaussian process hyper-parameters and inferred rotational properties in Tables A1 and A2 in Appendix A. In general, we find the largest changes in spin-down can be broadly described by four different categories:

- (i) quasi-periodic $\dot{\nu}$ variations with one or multiple characteristic period(s),
- (ii) a constantly changing value of $\dot{\nu}$ that does not display clear quasi-periodic behaviour,
- (iii) long-term smooth variations in $\dot{\nu}$ over long timescales and
- (iv) transient increases or decreases in $\dot{\nu}$.

Profile variability maps were generated for 214 pulsars that displayed significant $\dot{\nu}$ variations, which can be found in the Supplementary Materials. One such example is shown in Figure 4 for PSR J1048–5832, where the upper and lower panels present the varying spin spin-down rate and profile shape changes respectively. The remaining 24 of the 238 variable pulsars had insufficient per-epoch S/N to generate accurate variability maps. From these maps, we found that 52 pulsars showed substantial changes in profile shape. We also identified several pulsars that appear to show intense epoch-to-epoch shape variations across the entire profile that are approximately symmetric about the peak. This behaviour can be attributed

to profile jitter, resulting from the finite number of rotations that are recorded in our relatively short, per-pulsar observations. Pulsars that were most strongly affected by this include PSRs J0837–4135, J1430–6623 and J1644–4559, which are not included in the profile shape change analysis.

4.1 Known variable pulsars

Among our sample are 23 pulsars that had been previously identified as displaying correlated profile and spin-down variations, or emission state switching in single-pulse observations. Here we provide brief summaries of how these pulsars have either continued to vary with time, or display newly discovered variability.

PSR J0742–2822 (B0740–28)

Among the initial sample of variable profile/spin-down pulsars reported by Lyne et al. (2010), PSR J0742–2822 has a fast variability timescale of only ~ 135 d. The relationship between changes in profile shape and spin-down rate of this pulsar is complicated. Both are largely uncorrelated on long-time scales, but display an increased levels of correlation following the MJD 55022 glitch (see, Keith et al. 2013), suggested to be a result of glitch-induced coupling between the internal and external dynamics of the pulsar. This behaviour is readily apparent in the variability map as deficits (excess) emission from the leading (dip between leading and trailing) profile components. The increased correlation appears to vanish ~ 330 d before the MJD 56727 glitch, and fails to re-appear in the post-glitch spin-down/shape variations. Similarly, the MJD 59839 glitch also does not result in enhanced correlation between the profile and spin-down rate, indicating the phenomenon identified by Keith et al. (2013) is not a universal feature of the post-glitch behaviour of PSR J0742–2822.

PSR J0729–1448

The main peak in this pulsar’s profile was found to have switched from a brighter emission state to a weak state in MeerKAT observations taken around MJD 59400 by Basu et al. (2024). No clear correlation was identified between this state change and variations in the pulsar spin-down rate. Our less sensitive Murriyang observations do not reveal any noticeable profile shape variations, however the spin-down modelling recovers rapid 0.91% fluctuations in $\dot{\nu}$. A Lomb-Scargle periodogram generated from the spin-down timeseries recovered an apparent quasi-period of ~ 183 d.

PSR J0614+2229 (B0611+22)

This 0.33 s pulsar that has been reported to switch between two emission states: ‘mode A’ where the emission occurs slightly earlier in pulse phase, and ‘mode B’ where it is both weaker and arrives slightly later (Zhang et al. 2020). Our spin-down model displays rapid, short-duration decreases in spin-down rate with a quasi-periodic spacing of ~ 268 d. These spin-down events typically last between 130–200 d with typical amplitudes of $\delta\dot{\nu}/|\dot{\nu}| \sim 1.58\%$. The profile variability map shows the trailing edge of the profile displays changes on a similarly rapid timescale, usually appearing as an excess of emission whenever the pulsar is in the lower spin-down state that is only mildly correlated with the spin-down timeseries. An excess of emission in this part of the profile would point to the pulsar preferentially emitting in ‘mode B’ between the quasi-periodic decreases in spin-down rate.

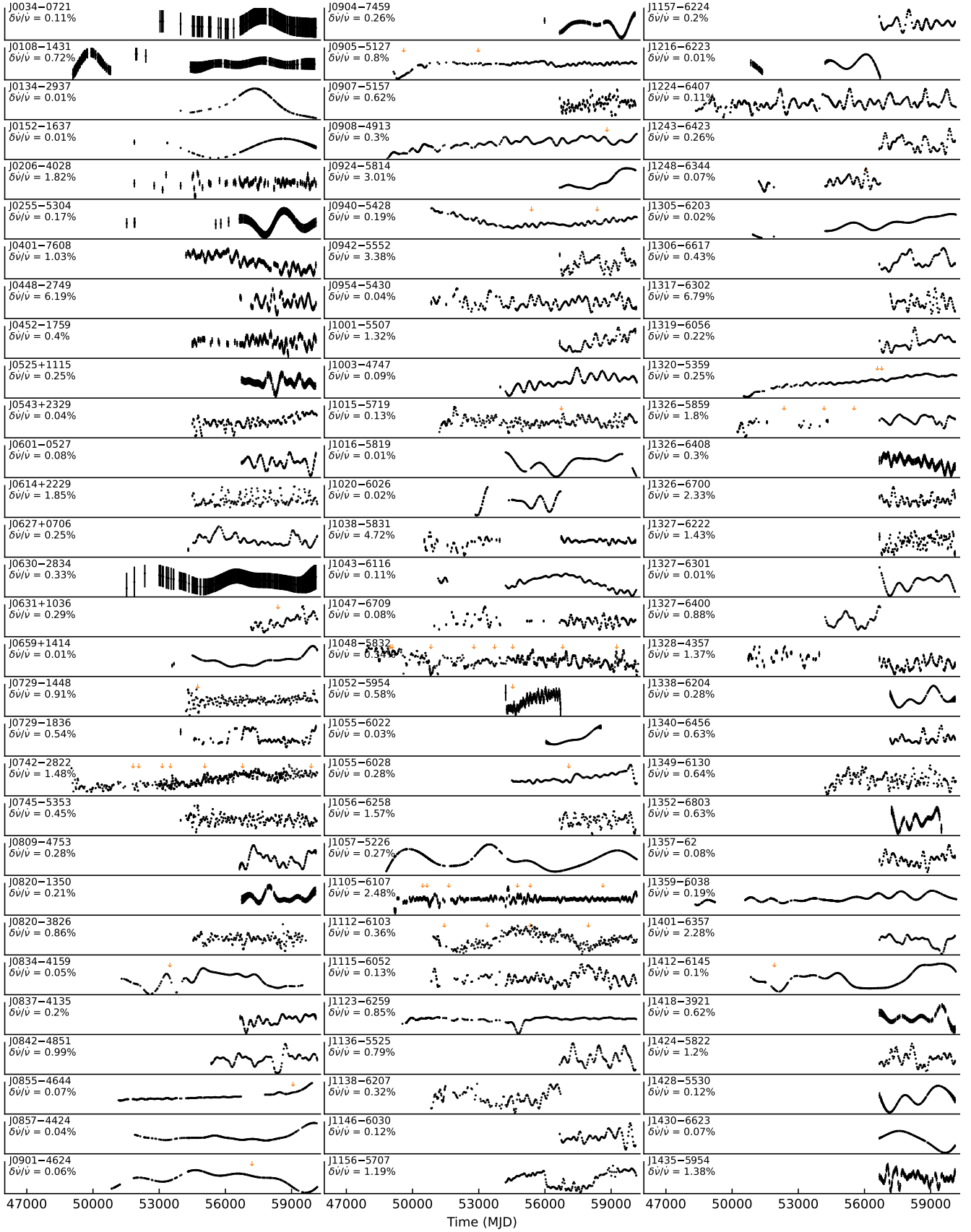


Figure 3. Spin-down timeseries for the 238 pulsars that displayed significant variability. Labels on the left-hand side of each panel indicates the pulsar J2000 name and the percentage difference between the minimum and maximum value of $\dot{\nu}$. The downward pointing arrows indicate the epochs of detected glitches.

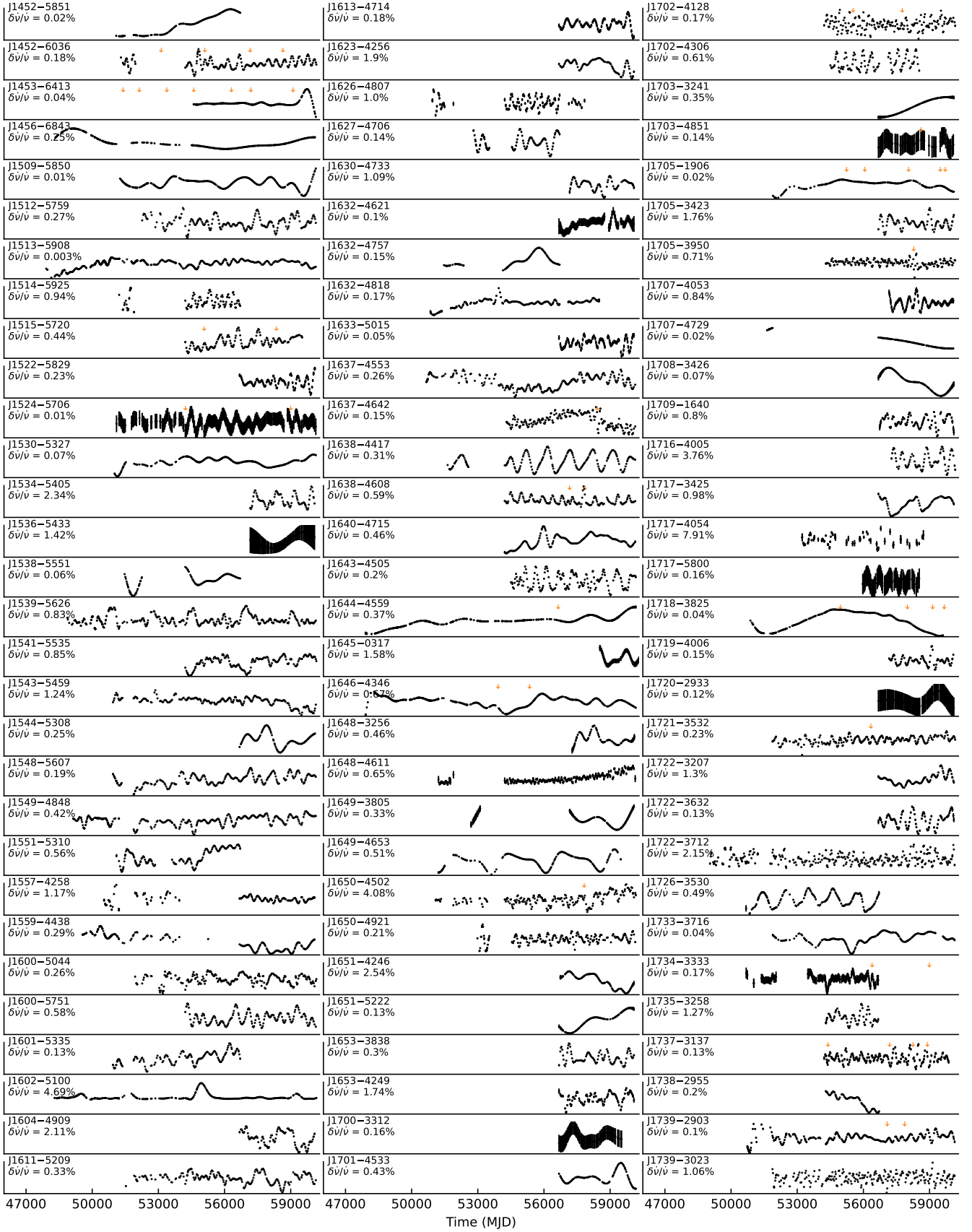


Figure 3 – continued

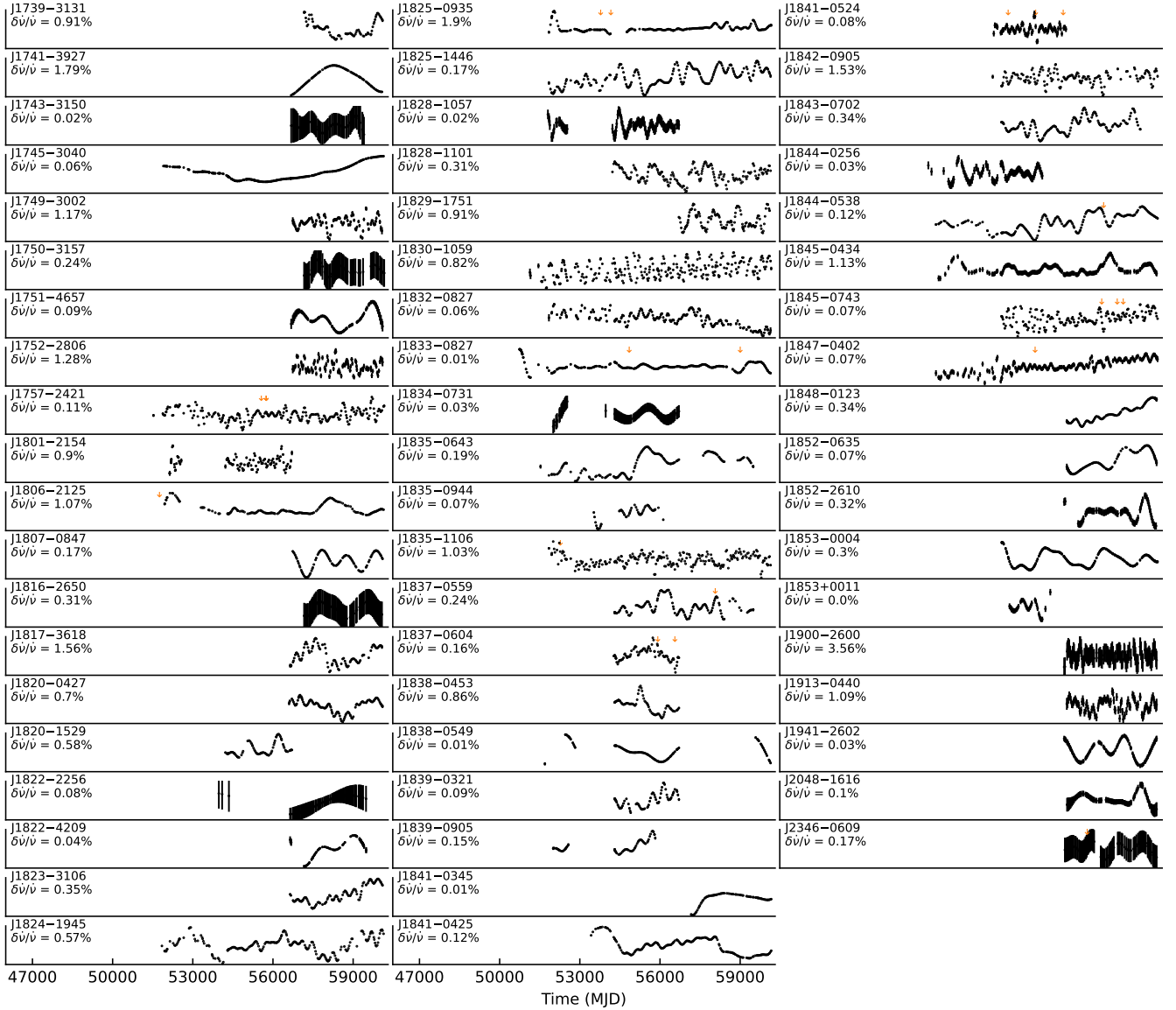


Figure 3 – continued

PSR J0908–4913 (B0906–49)

Rocketing away from the putative supernova remnant G270.4–1.0 (Johnston & Lower 2021), this orthogonally rotating pulsar was found by Brook et al. (2016) to display correlated changes in the leading edge of the main pulse and both inter-pulse components. All three of these profile components display simultaneous excesses and deficits of emission, which are also reflected in our updated profile variability map. Our profile/spin-down correlation map shows a positive correlation between the changes in these profile components that lag corresponding spin-down variations by ~ 300 d, while the more rapid changes in the peak of the main-pulse being uncorrelated with spin down rate. Similar cross-talk between emission originating from antipodal magnetic poles was previously identified in the single-pulse mode switching of PSRs J1057–5226, J1705–1906

and J1825–0935⁶ (Weltevred et al. 2007, 2012; Fowler & Wright 1982), indicating emission state-switching is a global phenomenon that affects the plasma content of the entire magnetosphere. We also detect more rapid variations in the primary peak of the main-pulse, though this may be the result of profile jitter shifting the exact peak of the profile from epoch-to-epoch. A small glitch occurred in PSR J0908–4913 on MJD 58765 (Lower et al. 2021), which does not appear to have had a noticeable impact on the post-glitch profile shape or spin-down variability.

PSR J0940–5428

This pulsar was noted by Brook et al. (2016) as an example where changes in spin-down over time are not necessarily linked to substan-

⁶ Note that model fits to the linear polarisation position angle swing of PSR J1825–0935 are consistent with both an aligned or orthogonal rotator (Johnston et al. 2023).

tial changes in profile shape, which also holds true for our extended monitoring. Our profile variability map does pick up some low-level changes in the leading half of the brighter, secondary profile component. However it does not appear correlated with corresponding changes in spin-down rate.

PSR J1001–5507 (B0959–54)

Long-term monitoring of PSR J1001–5507 by [Chukwude & Buchner \(2012\)](#) using the 26 m telescope at the Hartebeesthoek Radio Astronomy Observatory (HartRAO) revealed this pulsar underwent a transition from a low to high spin-down state between MJD 48500–49300 with a $\delta\dot{\nu}/|\dot{\nu}| \sim 1.3\%$. This coincided with the appearance of a bump in the leading edge of the pulse profile. The spin-down timeseries that we recover for PSR J1001–5507 in Figure 3 is initially consistent with the pulsar being in the high spin-down state, remaining somewhat flat until around MJD 58000, after which it appears to follow a linear decrease that continues to the last observation. On top of the secular spin-down evolution there is a clear quasi-periodic process which shows up two peaks in the Lomb-Scargle periodogram at 511 d and 1428 d. We also detect substantial changes in profile shape throughout our observing campaign, largely appearing as increased/decreased emission from the leading edge of the main peak and precursor bump. These variations appear to be largely uncorrelated with the short-term quasi-periodic changes in spin-down rate.

PSR J1048–5832 (B1046–58)

This bright gamma-ray pulsar, PSR J1048–5832 is known to display quasi-periodic switching between a weak and strong emission state every ~ 17 rotations ([Yan et al. 2020](#)). Our spin-down model and profile variability map in Figure 4 shows this variable emission behaviour also extends to longer timescales. The profile variations appear confined to the leading shoulder and primary profile components, each displaying continuous evolution with time similar what is observed in the main peaks of PSRs J0908–4913, J1600–5400 and J1602–5100. It is therefore not surprising that the time-averaged inter-glitch profiles highlighted by ([Liu et al. 2024](#)) appear different to one another. The spin-down variations are qualitatively complex, though a Lomb-Scargle periodogram recovers a strong quasi-period at ~ 480 d. Our observed changes in the profile shape are only weakly correlated with $\dot{\nu}$ on a similar timescale.

PSR J1057–5226 (B1055–52)

An orthogonally rotating pulsar, PSR J1057–5226 is known to display simultaneous, short-timescale emission state switching across both its main pulse and inter pulse ([Biggs 1990](#); [Weltevrede et al. 2012](#)). The spin-down rate of this pulsar varies smoothly over time by $\delta\dot{\nu}/|\dot{\nu}| \sim 0.27\%$, with no clear quasi-periodicity picked up in the Lomb-Scargle periodogram. Our profile variability map reveals that inter-observation changes in the pulse profile of this pulsar are largely restricted to the main pulse, where the brightest peak displays rapid fluctuations in intensity, while the more central component has a long-term decay in intensity superimposed on similar rapid fluctuations. This slow variation is strongly anti-correlated with the spin-down timeseries.

PSR J1105–6107

This 63 ms pulsar with a double-peaked profile was noted by [Brook et al. \(2016\)](#) as displaying a significant deficit (excess) in emission peak from the leading (trailing) peak around \sim MJD 56500, coinciding with an increased spin-down rate. Our extended dataset reveals that this event was short-lived, lasting only ~ 200 d. A similar yet smaller scale profile/spin-down event occurred around MJD 57900. By far the largest changes in the rotation and emission characteristics of PSR J1105–6107 took place between MJD 54200–55600, where a substantial deficit in emission from both profile components occurs at the same time as several large fluctuations in spin-down rate and both moderate ($\Delta\nu_g/\nu \sim 29.5 \times 10^{-9}$) and large ($\Delta\nu_g/\nu \sim 950 \times 10^{-9}$) glitches on MJDs 54711 and 55300.

PSR J1326–5859 (B1323–58)

Timing of this pulsar at HartRAO over a 13 yr revealed its timing residuals displayed oscillatory variations with a best-fit quasi-period of 2560 d ([Frescura & Flanagan 2003](#)). Gaussian process regression analysis of the HartRAO timing by [Maritz et al. \(2015\)](#) showed this behaviour can be explained by quasi-periodic spin-down variations occurring on this timescale. Our analysis of the Murriyang observations clearly recovers the long-term quasi-periodic changes in spin-down rate of PSR J1326–5859. However, the periodogram reveals a sharp quasi-period of only 1272 d, approximately half the period found by [Frescura & Flanagan \(2003\)](#). This pulsar also displays significant profile shape changes, though the high amplitude, rapid variations either side of the main peak are likely a result of profile jitter as an excess on one side of the peak is always accompanied by a deficit on the other. The more subtle long-term changes in the precursor and tail components appear to be genuine state changes in the pulsar emission. The precursor component changes are weakly correlated with variations in the spin-down rate at zero-lag while changes in the tail lag the spin-down rate by ~ 500 d.

Curiously, the precursor component appears to be absent in the HartRAO pulse profiles presented in [Maritz et al. \(2015\)](#), which were generated by averaging data between MJD 48000–49500, yet appears in our earliest archival Murriyang observation on MJD 49589. It is possible that a profile shape-change event in the gap occurred between reported profiles, similar to the one exhibited by PSR J0738–4042 albeit without an accompanying large alteration in spin-down state ([Karastergiou et al. 2011](#); [Brook et al. 2014](#)). Another possibility is that the precursor is blended into the leading edge of the main profile component by dispersion measure smearing in the HartRAO data. The high dispersion measure of 287 pc cm^{-3} would introduce a 3.1 ms delay at 1.6 GHz, which is comparable to the precursor component width. We also note that HartRAO employed a single-polarization (right-hand circular) receiver during this period. Differences in detected elliptical polarization at different parallactic angles may have contributed to apparent changes in profile shape. A more detailed analysis of the HartRAO dataset may resolve this mystery.

PSR J1326–6700 (B1322–66)

[Wen et al. \(2020\)](#) found that this pulsar switches between at least three distinct emission states in its single pulses. These include a bright mode where the profile is comprised of three overlapping sub-components, a weak state where emission from the central and trailing component are suppressed, and occasional nulls. In terms of its long-term variability, we find PSR J1326–6700 displays distinct

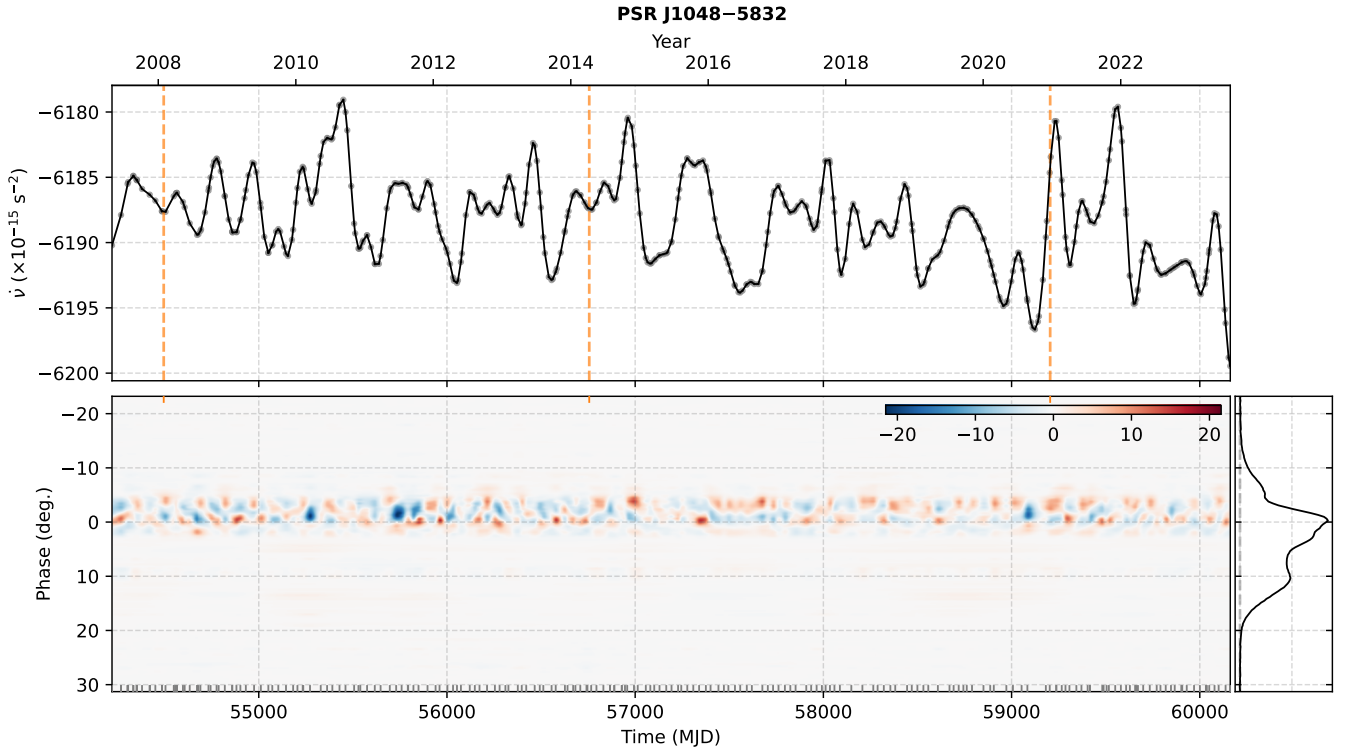


Figure 4. Rotation and emission changes in the known variable pulsar PSR J1048–5832. Top panel shows the spin-down timeseries, lower panel the profile variability map with the median profile depicted on the right. Orange dashed lines in the top panel indicate the epochs of glitch events. The short orange tick on the upper part of the variability map indicates the epochs of detected glitches, while the grey ticks along the bottom are the observation epochs at which the individual profiles were obtained.

sinusoidal variations in its spin-down rate, albeit of varying amplitude, with a quasi-period of ~ 427 d. These changes in spin-down are weakly correlated with deviations away from the median profile shape on the same timescale. The shape changes are likely a result of PSR J1326–6700 the pulsar switching between preferentially emitting in one emission mode (bright or weak), like many of the pulsars presented by Lyne et al. (2010).

PSR J1359–6038 (B1356–60)

Identified by Brook et al. (2016) as a variable pulsar, the Gaussian-like profile of PSR J1359–6038 often displays periods of excess emission on the right-hand slope that are correlated with transient decreases in spin-down rate that gradually decay back toward a steady state. An extreme broadening of both the left and right hand sides of the profile coinciding with a sudden $\sim 0.14\%$ drop in spin-down occurred between MJD 56450–56650 (Brook et al. 2016). Despite the much larger overall alteration in pulse shape, the spin-down rate change associated with this event is of comparable amplitude to those that coincide with the less substantial profile shape changes.

PSR J1401–6357 (B1358–63)

This 0.84 s pulsar exhibits both sub-pulse drifting and nulling, which were identified in single-pulse data collected using the Parkes UWL in 2018 (Chen et al. 2023). Over longer timescales, the blended two-component profile displays slow variations across the leading edge and rapid switching between excesses and deficits of emission over the peak and trailing shoulder. Extended periods in the emission

deficit state appear to coincide with two transient increases in $\dot{\nu}$ took place between MJD 57251–57887 and MJD 58891–59758, with respective peak amplitudes of $\delta\dot{\nu}/|\dot{\nu}| \sim 0.9\%$ and $\sim 1.7\%$. This is reflected in our correlation analysis, which shows a strong positive correlation between the changes in trailing shoulder emission and the spin-down timeseries.

PSR J1600–5044 (B1557–50)

This is another pulsar with spin-down variations that were initially identified in HartRAO observations (Chukwude et al. 2003) and profile shape changes by Brook et al. (2016). The profile shape variations are largely confined to the leading and trailing edges, appearing quite subtle when compared to other bright variable pulsars. As noted by Brook et al. (2016), the largest shape change occurred at the beginning of the Parkes young pulsar monitoring project in mid-2007, appearing as a strong deficit of emission either side of the profile peak in our variability map. The spin-down timeseries is dominated by triangular ‘saw-tooth’ shaped variations, where an initial decrease in $\dot{\nu}$ is followed by a prolonged linear increase until the next decrease. This is superimposed on a higher-frequency fluctuation in spin down that is not well resolved. The profile shape and spin-down changes are only weakly correlated. A Lomb-Scargle periodogram formed from the spin-down timeseries shows a strong peak at 1535 d, which matches the approximate delay between the largest spin-down events.

PSR J1602–5100 (B1558–50)

This is one of the best examples of a pulsar that displays a strong change in profile shape that coincides with a transient spin-down event in the Parkes data analysed by Brook et al. (2016). The spin-down rate of this pulsar decreased by $\delta\dot{\nu}/|\dot{\nu}| \sim 4.5\%$ over a 958 d period between MJD 54600–55400 at the same time as a decrease in the emission from the main profile component and the appearance of two sub-peaks in the lower intensity trailing component. This event identified by Brook et al. (2016) remains the most intense profile shape/spin-down event to have occurred in this pulsar to date. A similar, albeit weaker, appearance of the transient sub-peaks occurred between MJD 59005–59543 and coincided with a short decrease in pulsar spin-down rate. Two additional spin-down events of similar amplitude to this most recent change spanning MJD 49090–49715 and MJD 51383–5200 are also readily apparent in the legacy timing data (see Figure 3). The archival profiles are of insufficient quality to reliably confirm or rule out profile shape changes associated with these old events. There is no obvious quasi-period in the spacing between subsequent events, and no such periodicity is evident in a periodogram computed from the spin-down timeseries.

PSR J1645–0317 (B1642–03)

Cyclical variations in the timing of PSR J1645–0317 were initially identified by the Jet Propulsion Laboratory pulsar timing programme (Cordes & Downs 1985), which was interpreted as potential evidence the pulsar was undergoing free precession (Shabanova et al. 2001). Later analysis suggested this behaviour resulted from a series of ‘peculiar’, small-amplitude ($\Delta\nu_g/\nu \sim 10^{-9}$) glitches that were each separated in time by ~ 600 d (Shabanova 2009). Like many of the bright pulsars among our sample, the variability map for PSR J1645–0317 displays rapid, intense variations across the main peak of its pulse profile that likely originates from pulse jitter. However, there are also less intense, secular changes in the intensity of its precursor component. The precursor changes are strongly correlated with quasi-periodic changes in the spin-down rate on a timescale of approximately 610 d, with an excess of emission occurring when the pulsar is in a low spin-down state and a deficit in the high state. A longer timescale quasi-period of ~ 1425 d is also apparent in the spin-down timeseries and Lomb-Scargle periodogram. The 610 d quasi-period almost exactly matches the average spacing between the glitch-like events reported by Shabanova (2009). While there is a cuspy feature in our PSR J1645–0317 timing residuals, the turnover is drawn out over many observations as opposed to a sharp glitch-like discontinuity. Hence, the timing events that were previously reported as being glitches are likely to be misclassified spin-down variations. Similar such events in other pulsars, alongside random fluctuations in pulsar spin due to timing noise, have previously been misidentified as small glitches (Lower et al. 2020, 2023).

PSR J1705–1906 (B1702–19)

This is a 0.3 s orthogonal rotator that was found to display ‘on/off’ sub-pulse modulation across both its the main and inter pulse (Weltevrede et al. 2007). Like PSR J1057–5226, the spin-down rate of PSR J1705–1906 varies slowly over time, with an apparent, dominant quasi-period of ~ 2645 d. Our profile variability map does not recover any shape variations that are substantially different from fluctuations in the off-pulse noise, suggesting the rapid state switching every 10.4 rotations identified by Weltevrede et al. (2007) must be stable over long time scales. This is unlike other state switching pulsars, where

the profile shape changes recovered in the profile variability maps reflect the pulsar preferentially spending more time in one emission state than the other.

PSR J1703–4851

This 1.4 s pulsar was noted by Johnston et al. (2021) as switching between two distinct emission states: a ‘weak’ state where the profile consists of three approximately equal intensity sub-components and a ‘bright’ mode where the central component is up to an order of magnitude brighter than in the weak-state. Our spin-down model displays small variations with time of up to $\delta\dot{\nu} \sim 0.14\%$, albeit with large uncertainties, that is only weakly correlated with changes in profile shape. A small glitch with an amplitude of $\Delta\nu_g/\nu = 11.21(5) \times 10^{-9}$ and change in spin-down rate of $\Delta\dot{\nu}_g/\dot{\nu} = 3.0(2) \times 10^{-3}$ occurred around MJD 58570. Curiously, the profile variability map shows the bright state appears to have been more prevalent in observations taken before MJD 58750. It is unclear if the two phenomena are related since the bright-mode deficit lags the glitch by ~ 100 d.

PSR J1705–3950

This pulsar was noted by Basu et al. (2024) as displaying alternating fluctuations in intensity between the two peaks of its profile in long-term monitoring observations with MeerKAT. This behaviour appears to be a variant of that identified in the Lyne et al. (2010) sample, where the apparent switching between profile component intensities is due to the pulsar preferentially emitting from one component over the other (see the single-pulse data in Figure 5 of Basu et al. 2024). The switching in component intensities is marginally visible in our profile variability map. Our spin-down timeseries reveals the pulsar initially displayed clear quasi-periodic variability with two peaks in the Lomb-Scargle periodogram at 157 d and 314 d. This behaviour was seemingly interrupted by a glitch that occurred around MJD 58236, after which the quasi-periodicity becomes less defined, which may partially explain the lack of correlation with the emission state changes.

PSR J1717–4054

Situated somewhere between nulling and intermittent pulsars, PSR J1717–4054 exhibits three distinct null states lasting a few to tens of rotations during ‘active states’, and long inactive states that last many thousands of rotations (Kerr et al. 2014). As a result of its quasi-intermittency, we have comparatively few detections of this pulsar throughout our timing programme which results in the Gaussian process regression fits to its timing and profile residuals returning largely stochastic variations in both. There is a weak anti-correlation between the profile variability and the spin-down model. The $\delta\dot{\nu}/|\dot{\nu}| \sim 7.91\%$ displayed by this pulsar is the largest among our sample.

PSR J1741–3927 (B1737–39)

The main peak and trailing shoulder components of this pulsar were noted by Basu et al. (2024) as displaying correlated fluctuations in intensity, where an increase in the emission peak corresponded to a deficit in trailing shoulder emission, and vice-versa. No spin-down variability was reported in their analysis of PSR J1741–3927, however this appears to have been a result of the short timing baseline of the MeerKAT Thousand Pulsar Array, as our $\dot{\nu}$ timeseries shows

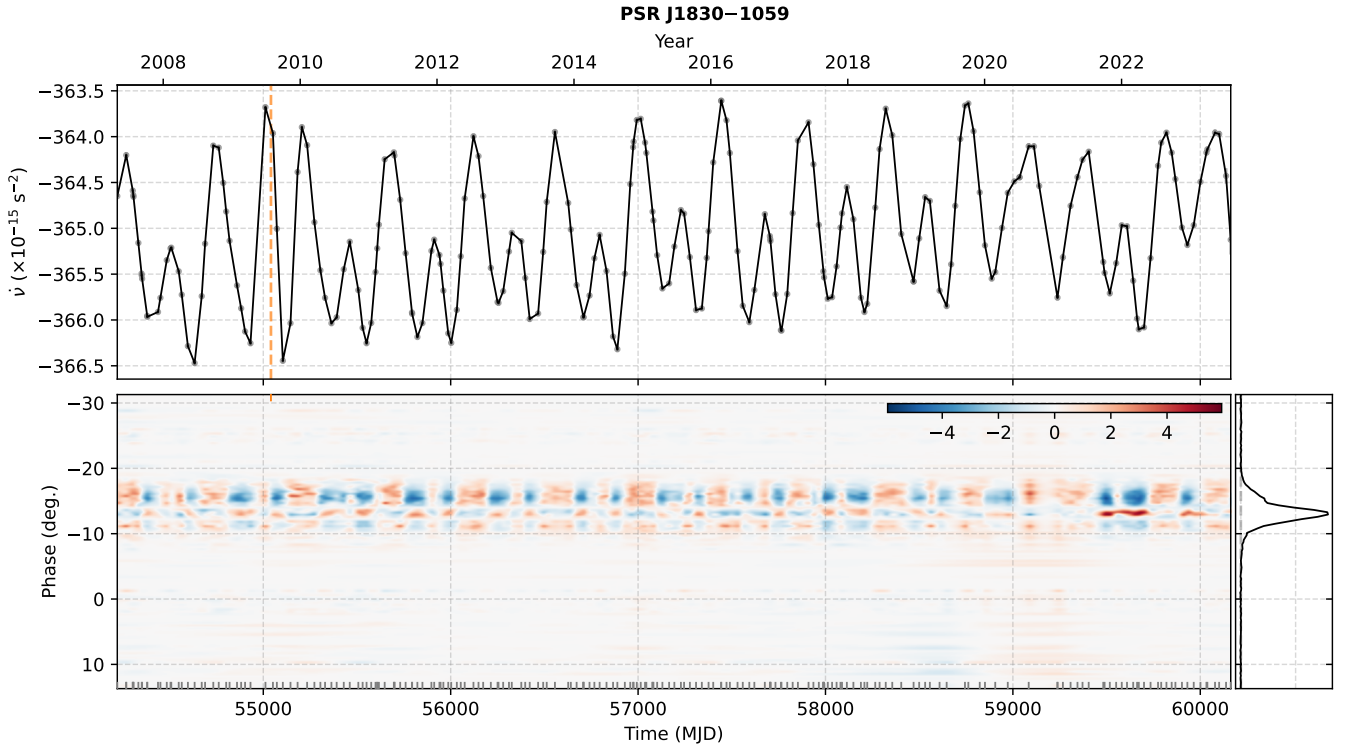


Figure 5. Spin-down timeseries and profile variability map for PSR J1830–1059. As Figure 4 otherwise.

a clear long-term fluctuation over our 10 yr of Murriyang observations. The profile variability map that we generated also shows the main peak undergoing clear, rapid variations on a timescale of a few hundred days, though we do not see similar anti-correlated changes in the trailing shoulder component. Instead, both the leading and trailing shoulders appear to undergo a secular increase in intensity that is correlated with the long-term change in $\dot{\nu}$ at a 1000 d lag.

PSR J1825–0935 (B1822–09)

A 0.77 s pulsar, PSR J1825–0935 is a well studied emission/spin-down mode-switching pulsar. Its radio emission switches between a ‘bright mode’ where a precursor component in the main pulse becomes active and the inter-pulse is suppressed, and a ‘quiet’ mode where the precursor component is inactive and the inter-pulse is active (Fowler et al. 1981). Single-pulse studies have shown that the switching in the main- and inter-pulse components occurs simultaneously indicating a strong degree of information exchange between the emission above both magnetic poles (Fowler & Wright 1982). Unlike several other mode-changing pulsars, the emission state-switching does not appear to extend to X-ray energies (Hermesen et al. 2017). Lyne et al. (2010) demonstrated that previously reported ‘slow glitches’ in the timing of PSR J1825–0935 (Shabanova 2005) corresponded to brief periods where the pulsar was in a low- $\dot{\nu}$ state and preferentially emitted in the bright mode. Our Parkes timing of PSR J1825–0935 only covers the last spin-down event described in Lyne et al. (2010), where the spin-down decreased by $\delta\dot{\nu}/|\dot{\nu}| \sim 2.7\%$. This event does not overlap with our profile variability map. There is also a gap in our timing between MJD 54144–54762, immediately following a moderately sized ($\Delta\nu_g/\nu \sim 1.17 \times 10^{-7}$; Lower et al. 2021) glitch on MJD 54115. Three small events with respective fractional decreases in spin-down of $\delta\dot{\nu}/|\dot{\nu}| \sim 0.6\%$, $\sim 0.4\%$ and

$\sim 1.1\%$ respectively that took place over MJD 57881–58222, MJD 58358–58669 and MJD 59344–59640. The last of these events was followed by an enhancement in the spin-down rate by $\delta\dot{\nu}/|\dot{\nu}| \sim 0.3\%$ between MJD 59640–60131 that coincided with the pulsar spending an extended period of time in the quiet emission mode, a first for PSR J1825–0935.

PSR J1830–1059 (B1828–11)

This is one of the best known mode-changing pulsars that displays highly correlated emission/profile variations. Initially thought to be evidence of free precession (Stairs et al. 2000), PSR J1830–1059 smoothly varies between three distinct spin-down states (high, medium and low, see Figure 5) with a min/max $\delta\dot{\nu}/|\dot{\nu}| \sim 0.8\%$ on timescales of approximately 500 and 220 d. Lyne et al. (2010) showed these changes in spin-down were correlated with changes in the profile shape, later revealed to be due to the pulsar spending preferentially more time in one of two extreme pulse shapes: a single bright component or a two-component profile consisting of a precursor bump at the leading edge of a bright peak (Stairs et al. 2019). Both the highly quasi-periodic spin-down rate and profile shape variations are easily recovered in our Gaussian process analysis of the Parkes data, which we show in Figure 5. A small $\Delta\nu_g/\nu \sim 6.3 \times 10^{-9}$ glitch was reported to have occurred on MJD 55040 (Basu et al. 2022), which lines up with a period in our spin-down timeseries where a large decrease in $\dot{\nu}$ occurred instead of an anticipated small change. Curiously, the modulation pattern in the spin-down timeseries appears to have changed after \sim MJD 59100. Instead of alternating between large and small changes in spin-down every 221 d, the pattern has become somewhat chaotic. Two large decreases in spin down occurred without an intervening small change, followed by a small change, and then two large changes. At the same time, the radio pro-

file spent extended periods of time in the two or single component states. While the more recent profile variations appear to have recovered back to the pre-MJD 59100 state, it is unclear yet whether the spin-down modulation has returned back to its ‘normal’ alternating between large/small spin-down state changes.

4.2 New pulsars with both profile and spin-down variations

Alongside the known variable pulsars, we have discovered another 28 pulsars that show fluctuations in both profile shape and spin-down rate. Here we summarise the kind of variations detected in the radio emission and spin-down properties of these pulsars.

PSR J0134–2937

This pulsar displays a slow, smooth change in $\dot{\nu}$ by $\sim 0.01\%$ over our 16 yr of Parkes monitoring. It also displays significant profile variability that is confined to the peak and trailing edge. These shape changes are uncorrelated with the spin-down timeseries, occurring on a substantially shorter timescale than the corresponding changes in $\dot{\nu}$. We note that this pulsar does exhibit a substantial amount of diffractive scintillation due to multi-path propagation in the interstellar medium. However, apparent scintillation-induced shape variations would affect the entire profile, as opposed to the relatively restricted region of the profile that we observe to vary.

PSR J0255–5304 (B0254–53)

The radio profile of this pulsar has two peaks that we found to exhibit substantial variability. The leading component shows both fast and slow changes, while the trailing component only varies slowly with time. In contrast, the spin-down rate varies smoothly over time, with a potential quasi-period of ~ 1648 d. Our correlation map suggests that the profile variations lag the changing spin-down rate by 500–1000 d.

PSR J0543+2329 (B0540+23)

This pulsar displays rapid changes in both profile shape and spin-down rate. Our profile variability map indicated the shape variations are largely due to longitudinal shifts in the central part of the profile that are not strongly correlated with changing spin-down. The periodogram computed from the spin-down timeseries has two peaks either side of 1 yr, which may be an artifact of a position offset in the timing model.

PSR J0630–2834 (B0628–28)

This pulsar displays a broadly Gaussian shaped radio profile, albeit with many blended sub-components. Its spin-down timeseries in Figure 3 exhibits slow $\delta\dot{\nu}/|\dot{\nu}| \sim 0.72\%$ fluctuations over 23.5 yr of timing. This is contrasted by the profile variability map, which shows rapid changes across much of the profile peak that appear somewhat uniform across the smaller sub-components. Our cross-correlation analysis returns no substantial positive or negative correlation between the profile variability map and the spin-down timeseries.

PSR J0631+1036

The profile of this pulsar is comprised of four sub-components: two dominant peaks that are flanked by weaker leading and trailing components. Our derived profile variability map reveals small, transient changes in the two dominant components that appear as a deficit in the leading bright peak and an excess in the trailing peak. These shape changes appear to coincide with short-duration decreases in spin-down rate. However, there is no strong correlation between the variability map and $\dot{\nu}$ timeseries, which displays seemingly chaotic, short-term variations on top of a longer-term linear decrease. The Lomb-Scargle periodogram generated from the $\dot{\nu}$ model fails to recover a substantial quasi-period.

PSR J0729–1836 (B0727–18)

This pulsar switches between two quasi-stable spin-down states with $\delta\dot{\nu}/|\dot{\nu}| \sim 0.54\%$, similar to what is seen in PSR J2043+2740 though without clear correlated changes in profile shape (Lyne et al. 2010; Shaw et al. 2022). Its profile shape variations are confined to the leading peak and trailing edge of the profile. However, unlike the variations seen in PSR J2043+2740, our correlation map shows these changes in emission are only weakly anti-correlated with the switches between spin-down states.

PSR J0820–1350 (B0818–13)

This is a slower 1.3 s pulsar, PSR J0820–1350 displays a blended double-peaked profile and a bump in the leading edge. The secondary peak has a substantial amount of rapid variability with time. These rapid profile variations are in contrast with the slow shifts in spin-down rate by $\delta\dot{\nu}/|\dot{\nu}| \sim 0.21\%$ over time. Our Lomb-Scargle periodogram analysis recovers a possible quasi-period of ~ 1281 d in the spin-down timeseries for this pulsar.

PSR J0942–5552 (B0940–55)

This pulsar displays correlated profile and spin-down variations that fluctuate on relatively long timescales of 2–3 years. We find profile shape changes occurring in the leading precursor component, right-hand shoulder of the main peak and the trailing component. Excess emission from these regions are observed when the pulsar is in a lower spin-down state. Small deficits of emission occur when the spin-down rate is higher. Our periodicity analysis detects a substantial amount of power at a 1 yr quasi-period, which likely results from a small positional offset in the timing model from the true sky location.

PSR J1056–6258 (B1054–62)

Similar to PSR J0742–2822, this pulsar displays a complicated relationship between its highly variable profile shape and spin-down rate. The spin-down rate shows rapid changes with time, with quasi-periods of 456 d and 177 d. The entire profile is affected by shape variations that appear strongest across the peak, which also vary on short timescales. Emission and spin-down processes appear to be uncorrelated with one another similar to the pre-glitch behaviour of PSR J0742–2822.

PSR J1224–6407 (B1221–63)

This is a bright, 0.22 s radio pulsar that displays two strong quasi-periods in its long-term spin down rate at ~ 427 d and ~ 747 d. Our profile variability map shows rapid changes across much of the profile on timescales that are shorter than both detected quasi-periods in the spin-down timeseries, indicating the two processes are largely decoupled from one another. The strongest of these variations occur in the precursor component, which appear uncorrelated with the spin-down rate, as opposed to variations in the profile peak which are mildly correlated with $\dot{\nu}$.

PSR J1243–6423 (B1240–64)

Similar to PSR J1224–6407, this pulsar displays substantial profile shape variations on a more rapid timescale than the observed changes in spin-down rate. Our correlation analysis indicates there is a ~ 200 d lag between changes in $\dot{\nu}$ and the bump in the main profile component changes, and a ~ 400 d lag with changes in the trailing edge. The spin-down timeseries displays two distinct quasi periods at ~ 626 d and ~ 1203 d. Figure 6 shows a set of archival single-pulse data collected by Murriyang on MJD 57600, which reveals the radio emission of PSR J1243–6423 switches between at least two distinct states. This includes a bright state, where emission is detected from across the profile, and a weak state where the emission primarily originates from a low-flux density trailing profile component. There are also nulls in between several switches between emission state. This nulling behaviour was previously identified in single pulse data collected by the Molonglo Observatory Synthesis Telescope (Biggs 1986). Comparing the on-pulse flux density against the root-mean-square (RMS) of the off-pulse region in Figure 6 returned an approximate nulling fraction of 0.12, a factor of three higher than the previously reported value of ≤ 0.04 (Biggs 1992). This could be due to a preference for null pulses when PSR J1243–6423 is in a particular spin-down state, similar to what is seen among other emission state-switching pulsars.

PSR J1327–6222 (B1323–62)

PSR J1327–6222 is another pulsar that displays rapid, albeit seemingly uncorrelated, variations in both its radio profile shape and spin-down rate over time. The profile shape changes appear in both components of the blended, two-peaked profile with no clear quasi-stable states that the pulsar switches between. Given the rapid changes in both profile shape and spin-down, it is possible our approximately monthly observing cadence is unable to fully resolve any underlying quasi-stable states. These somewhat random profile shape changes are interspersed with brief periods of enhanced emission from a bump in the trailing shoulder, the two most prominent of which occurred around MJD 58915 and MJD 59768.

PSR J1328–4357 (B1325–43)

This is a pulsar with a blended two-component profile with shape variations that are predominantly restricted to increased/decreased emission from the trailing component. These shape variations are uncorrelated with the changing spin-down rate, which has a dominant quasi-period that peaks near 365 d. Given the somewhat ragged appearing spin-down timeseries, this quasi-period may be indicative of a strong degeneracy between an incorrectly modelled pulsar position with a near-annual quasi-periodic process.

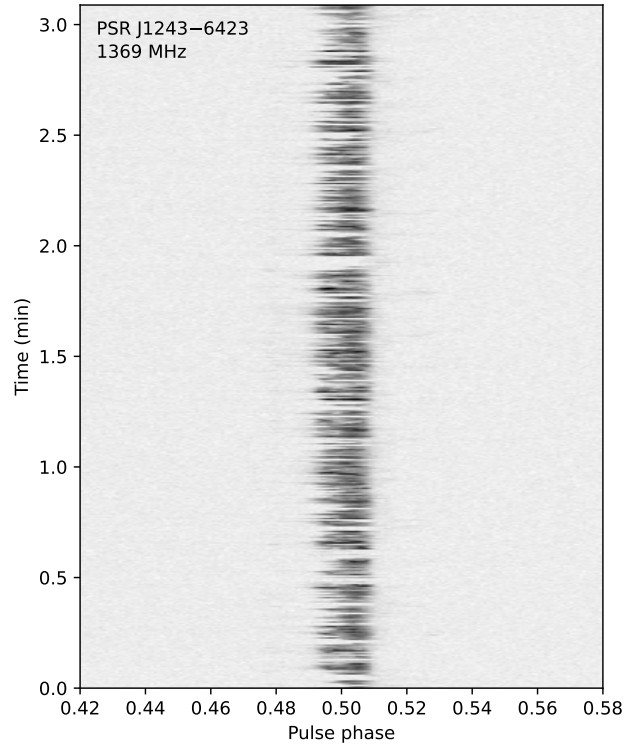


Figure 6. Stack of 482 single pulses from PSR J1243–6423 recorded using the Parkes 20-cm multibeam receiver on MJD 57600. Nulls and weak radio pulses are clearly visible as gaps among the normally bright emission from this pulsar.

PSR J1428–5530 (B1424–55)

This pulsar displays slow changes in spin-down rate with an amplitude of $\delta\dot{\nu}/|\dot{\nu}| \sim 0.12\%$. However its variable profile shape fluctuates on a much shorter month-long timescales. The observed profile variations appear as increases in width and are most prominent in the trailing edge of the overall Gaussian shape. These changes in the trailing edge are moderately correlated with the spin-down timeseries. Inspection of the profile variability map shows the enhanced emission from this part of the profile appears more prevalent with the pulsar is in a lower spin-down state.

PSR J1453–6413 (B1449–64)

This is a 0.18 s pulsar that has undergone four glitches since the beginning of our timing programme in 2007. The spin-down timeseries of PSR J1453–6413 is largely flat, except for two noteworthy fluctuations in $\dot{\nu}$, one that took place between MJD 57057–58645 and another that began around MJD 59182 and is ongoing. These events appear to be associated with excess emission from the leading bump in the pulse profile, though our correlation analysis suggests there is only a weak positive correlation between the variability map at these pulse phases and the spin-down timeseries. The more rapid profile shape changes that occur in the leading edge of the profile peak are uncorrelated with the changes in $\dot{\nu}$. It is unclear if these profile/spin-down events are related to the small amplitude glitches that took place several hundred days prior to their onset.

PSR J1456–6843 (B1451–68)

PSR J1456–6843 is an example of a pulsar where changes in profile shape are not associated with variations in $\dot{\nu}$. It has a complicated, albeit symmetric pulse profile that appears comprised of multiple blended components. Our variability map shows these components each varying randomly over time, which according to the correlation map is decoupled from the substantially slower $\delta\dot{\nu}/|\dot{\nu}| \sim 0.75\%$ change in spin-down rate over time.

PSR J1559–4438 (B1556–44)

This pulsar has a triple-component radio profile, with low intensity precursor and trailing components and a bright central component that has a ‘shoulder’ on its trailing edge. All three components display shape variations different timescales. The precursor and trailing components both show simultaneous excess and suppressed emission that is correlated with the changing spin-down rate of the pulsar. Emission from the leading edge of the central component varies on a similar timescale, but lags changes in the precursor/trailing components by ~ 400 d. The shoulder on the central component displays more rapid variations, yet appears to preferentially emit in a weak state in concert with the precursor and trailing components. Changes across the central component peak are anti-correlated with the varying spin-down rate and are out of phase with changes in the other components by half a cycle. While the spin-down rate of PSR J1559–4438 visually appears to display both long and short timescale variations, with the more rapid changes appearing quasi-periodic, no substantial peaks are detected in the corresponding Lomb-Scargle periodogram.

PSR J1604–4909 (B1600–49)

Another triple-component pulsar, where the changes in intensity displayed by the bright central peak are highly correlated with step-like changes in spin-down rate. The shape changes are characterised by the appearance of an excess bump in the central component peak whenever the pulsar is in a low spin-down rate, which rapidly disappears over the ~ 200 d transition to the high spin-down state. This is somewhat reminiscent of the transient variations reported in PSR J2043+2740 (Lyne et al. 2010; Shaw et al. 2022), however the changes in PSR J1604–4909 display a ~ 1698 d cycle between emission/spin-down states. While there is an apparent shorter timescale process that is superimposed on the spin-down timeseries, our Lomb-Scargle periodogram does not recover any significant power at periods other than that associated with the long-term process.

PSR J1703–3241 (B1700–32)

The spin-down rate for this pulsar displays a gradual decrease over eight years of Parkes monitoring. This is in contrast to the profile variability map, which shows rapid changes in emission across its two dominant sub-components, with the brighter leading peak showing the strongest intensity fluctuations. As expected, these changes in profile shape are uncorrelated with the decrease in $\dot{\nu}$.

PSR J1709–1640 (B1706–16)

This 0.65 s pulsar has a relatively simple radio profile that displays substantial fluctuations in intensity across its trailing edge. These changes in profile shape appear to be weakly correlated with variations in $\dot{\nu}$, albeit with a ~ 100 d lag. The Lomb-Scargle periodogram

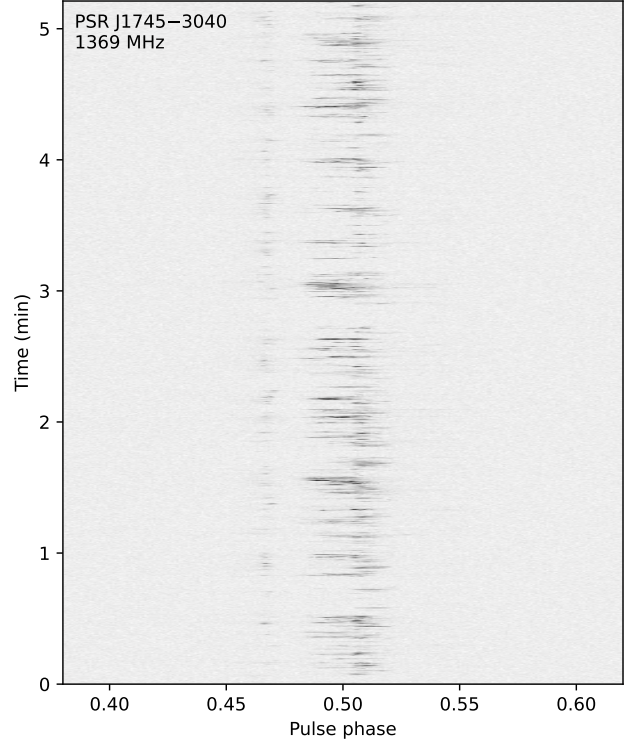


Figure 7. A set of 850 single pulses from PSR J1745–3040 recorded using the Parkes 20-cm multibeam receiver on MJD 56466. The ‘off’ emission state appears as gaps in the detected radio emission.

computed from the spin-down timeseries displays a strong peak at 359 d, which could be a result of a near-1 yr quasi-period beating with a small discrepancy in the pulsar position in the timing model.

PSR J1745–3040 (B1742–30)

PSR J1745–3040 is a bright gamma-ray pulsar with a 0.37 s spin period. It has a two-component radio profile with the brighter trailing component consisting of a bright peak and a leading bump. Both components display substantial epoch-to-epoch changes in intensity in the profile variability map that are uncorrelated with the slow, secular changes in $\dot{\nu}$ over time. This variability appears to be a result of both our short observation times and emission state switching in the single pulses of PSR J1745–3040, behaviour that is also seen in similarly bright pulsars such as PSRs J1048–5832 and J1243–6423. In Figure 7 we present a stack of single pulses detected by Murriyang, where the pulsar clearly switches between on and off emission states. When the pulsar is in the ‘on’ state, we detect radio emission from both profile components, occasionally interspersed with very bright bursts from the main peak of the second component. Whereas the ‘off’ state appears to be extended nulls, where no radio emission is detected down to the sensitivity limit of the instrument. A simple comparison between the mean on-pulse flux density and the off-pulse RMS reveals an approximate nulling fraction of 0.51 during the observation presented in Figure 7. Unlike the other pulsars among our sample that display similar behaviour, there does not appear to be a strong association between for the pulsar preferentially emitting in one emission state over the other and the changes in $\dot{\nu}$ over time. This may however, simply be due to the much lower frequency fluctuation timescale of $\dot{\nu}$ and relatively high nulling fraction of this pulsar.

PSR J1751–4657 (B1747–46)

The radio profile of this pulsar consists of a blended, two-component profile that displays rapid fluctuations in intensity confined to the brighter, leading peak. These intensity changes are mildly correlated with the slowly varying spin-down rate. There is a persistent emission deficit that coincided with the pulsar being in a high spin-down state between MJD 58122–59248.

PSR J1752–2806 (B1749–28)

Similar to PSR J0742–2822, this pulsar also displays both rapid variations in profile shape and spin-down rate with a low Q-factor quasi-period of ~ 157 d. The shape changes affect the entire profile to some degree, but are strongest at the peak. Some of this variability may therefore be the result of profile jitter. However, the shape changes are correlated with the rapidly varying spin-down rate, albeit with a ~ 50 d lag. No glitches have been detected in the timing of PSR J1752–2806 to date.

PSR J1820–0427 (B1818–04)

The profile of PSR J1820–0427 is relatively simple, consisting of a bright peak with both leading and trailing shoulders of emission. Our profile variability map reveals changes in intensity within the leading shoulder and peak that are uncorrelated with the detected fluctuations in the pulsar spin-down rate. This is despite the transient increase in spin-down rate of $\delta\dot{\nu}/\dot{\nu} \sim 0.7\%$ that occurred between MJD 58169–59088.

PSR J1824–1945 (B1821–19)

The radio profile of PSR J1824–1945 displays rapid shape variations in spite of a slowly changing spin-down rate. Much of the rapid changes either side of the profile peak can be attributed to epoch-to-epoch jitter, with a deficit of emission on one side being countered by an excess on the other. There is however a clear correlation between the slowed intensity changes across the profile peak itself and the spin-down rate at a lag of ~ 1000 d. Inspection of the $\dot{\nu}$ model in Figure 3 reveals two slow, transient increases in spin-down rate that took place between MJD 53616–54441 and MJD 57564–58852 with $\delta\dot{\nu}/|\dot{\nu}| \sim 0.3\%$ and $\sim 0.2\%$ respectively. A small offset in the pulsar position in our timing model is likely to be responsible for the high frequency fluctuation in $\dot{\nu}$ that is superimposed on the slow variations with time.

PSR J1829–1751 (B1826–17)

This pulsar displays a triple peaked profile where all three components have approximately equal intensity. Our profile variability map shows that these components all display varying levels of intensity fluctuations, with the leading and trailing components mirroring one another. The spin-down timeseries reveals a quasi-periodic switching between high and low spin-down states every ~ 807 d, which is weakly anti-correlated with changes in the trailing profile component. Visually both the leading and trailing components display an excess of emission when PSR J1829–1751 is in the high spin-down state, and a deficit when in the low state. A higher-fluctuation frequency quasi-period in the spin-down rate may be linked to the peak in periodogram power at 1 yr, likely resulting from an incorrect position in the timing model.

PSR J1845–0434 (B1842–04)

The 0.49 s radio pulsar PSR J1845–0434 displays a two-component profile consisting of a bright leading peak and a trailing shoulder. Its spin-down timeseries reveals it undergoes transient decreases in spin-down rate by $\delta\dot{\nu}/|\dot{\nu}| \sim 0.1\text{--}0.9\%$ that last 228–975 d. Each event is separated in time by approximately 1000–2000 d. The first and fourth decreases in spin-down rate appear to coincide with an excess of emission from the trailing shoulder component, despite the overall profile variability map covering this segment being only weakly correlated with the $\dot{\nu}$ timeseries. Curiously, the recovery stage of the second spin-down event that we detect appears to also coincide with an excess in emission from the shoulder component, while the third and fifth events do not have any corresponding profile shape change.

PSR J1913–0440 (B1911–04)

PSR J1913–0440 is another bright radio pulsar with profile shape changes confined to the trailing edge of its profile. Its changes appear to be weakly anti-correlated with high fluctuation frequency variations in the spin-down timeseries, for which our periodicity analysis failed to recover a corresponding (quasi-)period. Instead only the lower frequency variation with a quasi-period of ~ 1066 d was recovered. Similar to PSR J1327–6222, our monthly observing cadence may be insufficient to fully resolve the short-time scale quasi-periodicity.

PSR J2048–1616 (B2045–16)

This bright 22 mJy pulsar (at 1.4 GHz) with a triple component profile, where all three components display seemingly random fluctuations in relative intensity. Like many of our newly identified profile/spin-down varying pulsars, the component shape changes take place on a more rapid timescale compared to the slowly changing value of $\dot{\nu}$. However, there is a weak anti-correlation between the variability map and the spin-down rate across all three components. The Lomb-Scargle periodogram computed from the $\dot{\nu}$ timeseries recovered a quasi-period of ~ 1015 d.

4.3 Other noteworthy pulsars*PSR J1513–5908 (B1509–58)*

An unusual young, energetic pulsar surrounded by a wind nebula in the supernova remnant SNR G320.4–1.2 (see, [Gaensler et al. 2002](#) and references therein). In spite of its relative youth, the long-term timing of PSR J1513–5908 is uncharacteristically stable, enabling measurements of both its braking index of $n = 2.832 \pm 0.003$ and higher-order braking index of $m = 17.6 \pm 1.9$ ([Livingstone & Kaspi 2011](#)). It has also not glitched in over 30 years of timing ([Parthasarathy et al. 2020](#)), counter to the expected glitch rate of 0.9 yr^{-1} for pulsars with similar rotational properties ([Lower et al. 2021](#)). After correcting for the spin-frequency of PSR J1513–5908 and its first, second and third derivatives, our Gaussian process fit to its timing residuals reveals short timescale fluctuations in $\dot{\nu}$ with a low Q-factor quasi-period of ~ 307 d. This short-term behaviour is superimposed on a longer timescale, smooth change in spin-down, where the amplitude of $\delta\dot{\nu}/|\dot{\nu}| \sim 0.03\%$ is the smallest out of our entire sample. No changes in profile shape were identified, owing to our relatively short integration times and its weak profile.

PSR J1734–3333

This high magnetic field strength pulsar with an unusually low braking index of $n = 1.2 \pm 0.2$ (Espinoza et al. 2011; Lower et al. 2021). Subtracting the linear slope induced by the $\dot{\nu}$ term leaves a predominantly flat spin-down timeseries for most of its 1997–2014 timing history. However, there are several transient changes in $\dot{\nu}$ occurring between MJD 53489–53729, MJD 54270–54550 and MJD 55425–55597. The second and largest event appears qualitatively similar in direction and shape to a recent transient spin-down change identified in X-ray timing of PSR J0540–6919 (B0540–69; Espinoza et al. 2024), albeit with an order of magnitude larger fractional increase in spin-down rate of $\delta\dot{\nu}/|\dot{\nu}| \sim 0.1\%$. No profile shape changes are detected alongside any of these spin-down events. However, this is not surprising given the relatively weak and scatter-broadened profile of PSR J1734–3333 at 1.4 GHz.

PSR J1806–2125

This pulsar underwent a giant glitch sometime between MJD 50850–52250 (Hobbs et al. 2002). Although this event occurred prior to our first Murriyang timing measurements, we clearly detected the exponential recovery from it in the pulsar timing residuals. Fitting for only the decaying component of the glitch using TEMPO2 at a nominal glitch epoch of MJD 51708, we inferred a $\Delta\nu_d/\nu = 402(27) \times 10^{-9}$ with an exponential recovery timescale of approximately 490 d. While no further glitch events have occurred in this pulsar over the preceding 22 yr of timing, its spin-down rate displays several transient decreases by about $\delta\dot{\nu}/|\dot{\nu}| \sim 0.1$ – 0.3% between MJDs 54379–55051, 55372–55703, 56220–56837 and MJD 59737 onwards. A much larger transient spin-down event took place over MJD 57536–59079, where the pulsar was spinning down 0.9% slower than average. Curiously, all four of the events detected in full share a similar morphology, consisting of a rapid initial decrease in spin-down rate, followed by a near linear increase back to the ‘steady’ value. A higher-frequency quasi-period appears super-imposed on top of these events. Both the low ~ 0.8 mJy flux density of PSR 1806–2125 at 1.4 GHz and short per-epoch observations preclude us from detecting clear changes in profile shape associated with variations in spin-down.

5 DISCUSSION

We have identified 238 pulsars that exhibit substantial variations in their spin-down rates, of which 52 also display changes in profile shape, meaning that we have assembled the largest sample of variable pulsars to date. The propensity of these behaviours confirms previous suggestions that radio emission and spin-down state switching is commonplace among the broader pulsar population. With this large sample on hand we can also investigate how the amplitude of these effects scales with the average pulsar spin and spin-down rate, in addition to exploring the origins of specific sub-types of profile/spin-down rate variability.

5.1 Scaling relations across the population

While a direct causal relationship between the observed spin-down variability in pulsars and external or internal physical processes is yet to be established, we can explore how this behaviour scales phenomenologically with various pulsar properties. In Figure 8 we present the measured min/max difference in spin-down rate against the corresponding ‘weak’ (minimum) spin-down rate value for the

238 variable pulsars in our sample, alongside values from several previous works. Lyne et al. (2010) noted that their sample of 17 correlated profile/spin-down state switching pulsars appeared to follow a simple power-law relation, where $\delta\dot{\nu} \propto 0.01|\dot{\nu}_{\text{weak}}|$. A somewhat shallower power-law relation of $\log_{10}(\delta\dot{\nu}/|\dot{\nu}_{\text{weak}}|) \propto 0.84 \pm 0.02$ was recovered using extended timing of the same pulsar sample by Shaw et al. (2022). While there is a substantial number of pulsars in Figure 8 that reside about the original Lyne et al. (2010) relation (shown in black), about half of our larger sample are situated between one to three orders of magnitude below the relation. This is particularly true for pulsars with both higher and lower weak spin-down rates than those among the Lyne et al. (2010) sample.

Drawing on previous works to study similar relations between pulsar properties and stochastic timing noise strength (Dewey & Cordes 1989; Hobbs et al. 2010; Shannon & Cordes 2010; Parthasarathy et al. 2019; Lower et al. 2020), we compared how $\delta\dot{\nu}$ scales with $|\dot{\nu}_{\text{weak}}|$ through fitting a power-law of the form

$$\delta\dot{\nu} = 10^\xi |\dot{\nu}_{\text{weak}}|^b, \quad (5)$$

where ξ is an arbitrary scaling parameter and b is the scaling index of $\dot{\nu}$. We determined the posterior distributions for the model parameters using Bayesian parameter estimation with a Gaussian likelihood function of the form

$$\mathcal{L}(d|\theta) = \prod_i^{N_{\text{psr}}} \frac{1}{\sqrt{2\pi\sigma_i^2}} \exp \left[-\frac{(d_i - \mu(\theta))^2}{2\sigma_i^2} \right], \quad (6)$$

where d is the data, μ is the power-law model, θ is the model parameters, $\sigma_i^2 = \sigma_{\delta\dot{\nu},i}^2 + \sigma_Q^2$ is the per-pulsar uncertainties on $\dot{\nu}$ with an additional error in quadrature term added to account for scatter in our measurements. The model parameters were sampled using BILBY as a wrapper for the DYNesty nested sampling algorithm (Ashton et al. 2019; Speagle 2020). The resulting relationship is represented by the pink line in Figure 8, where

$$\delta\dot{\nu} = 10^{-4.5 \pm 0.5} |\dot{\nu}_{\text{weak}}|^{0.85 \pm 0.04}. \quad (7)$$

This is shallower than the aforementioned relation from Lyne et al. (2010), but consistent with that inferred by Shaw et al. (2022) at the 68% confidence interval. The power-law amplitude by comparison is substantially lower, resulting from the larger number of pulsars with lower $\delta\dot{\nu}$ than those analysed by Lyne et al. (2010) and Shaw et al. (2022).

We also tested whether $\delta\dot{\nu}$ preferentially scales according to various derived pulsar parameters, such as characteristic age (τ_c), implied surface dipole magnetic field strength (B_{surf}) and rate of rotational kinetic energy loss (\dot{E}). This was achieved by including a dependence on ν in the right-hand side of the scaling relation in Equation 5 as

$$\delta\dot{\nu} = 10^\xi \nu^a |\dot{\nu}|^b. \quad (8)$$

Using the same Gaussian likelihood function as before, we found the change in spin-down rate follows the scaling relation

$$\delta\dot{\nu} = 10^{-4.1 \pm 0.7} \nu^{-0.18 \pm 0.17} |\dot{\nu}|^{0.88 \pm 0.05}, \quad (9)$$

which is close to being consistent with the same $\delta\dot{\nu} \propto |\dot{\nu}|$ scaling relation from Equation 7. The posterior distribution for the ν scaling parameter overlaps with zero at the 95% confidence interval, indicating there is little dependence between the amount of spin-down variability in a given pulsar and its spin frequency.

5.2 Implications for precision timing experiments

Millisecond pulsars are known to display emission state switching on short timescales (Mahajan et al. 2018; Miles et al. 2022; Nathan

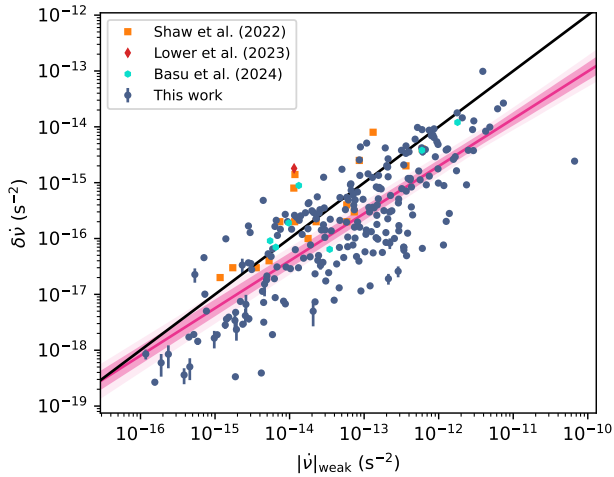


Figure 8. Relationship between spin-down variability and weak spin-down state. Values for the pulsars studied by Shaw et al. (2022) are shown in orange, the red diamond indicates PSR J0738–4042 (Lower et al. 2023), pulsars from Basu et al. (2024) are the teal hexagons, and our measurements are plotted in blue. Note, there are several pulsars in common between these datasets as indicated by overlapping points. The black line is the $\delta\dot{\nu} \propto 0.01|\dot{\nu}|_{\text{weak}}$ relation from Lyne et al. (2010). The pink line is the median a-posteriori fit to the blue points with the pink shading indicating the 68% and 97% confidence intervals.

et al. 2023) and transient profile shape changes (Shannon et al. 2016; Lam et al. 2018; Goncharov et al. 2021; Jennings et al. 2024), with the latter effect requiring either profile-domain timing techniques to correct for them or careful removal of the corresponding signal in the timing residuals (see, e.g. Shannon et al. 2016). The propensity of spin-down rate variations among our pulsar sample and clear positive scaling in variability amplitude with $\dot{\nu}$ suggests that this phenomenon may also be both present and detectable among the millisecond pulsar population. Accurately correcting for these effects is particularly important for precision timing experiments aiming to detect the stochastic gravitational-wave background.

Recent hints of such a gravitational-wave background signal among pulsar timing experiments have revealed an unexpectedly large amplitude given previous upper limits (Agazie et al. 2023a; EPTA Collaboration et al. 2023b; Xu et al. 2023; Reardon et al. 2023; Miles et al. 2025b), which appears to be increasing with time (Reardon et al. 2023). It is presently unclear whether this is a genuine feature of the common signal, in which case it would be inconsistent with expectations for an isotropic gravitational-wave background, but could be the result of an unmodelled process intrinsic to the observed millisecond pulsars. Spin-down rate changes similar to those among our P574 pulsars would manifest as a form of non-stationary timing noise, for which the red power-law models that are typically used to account for timing noise have been demonstrated as insufficient for fully characterising the resulting timing variations (Keith & Niu 2023; Lower et al. 2023).

Assuming the rotational characteristics of millisecond pulsars follow the same scaling as the young pulsar population, our results can be used to predict the expected spin-down rate variability among the pulsars currently monitored by pulsar timing arrays. The spin-down rates of the pulsars included in the upcoming third data release of the International Pulsar Timing Array (K. Liu, private communication; Zic et al. 2023; EPTA Collaboration et al. 2023a; Agazie et al. 2023b; Miles et al. 2025a) largely range be-

tween $\dot{\nu} = -10^{-16} \text{ s}^{-2}$ and -10^{-14} s^{-2} , alongside several noteworthy outliers such as PSR B1937+21 with its high spin-down rate of $-4.3 \times 10^{-14} \text{ s}^{-2}$. If the variable spin-down rate process is active among them, then from Figure 8 we would expect these pulsars to display changes in $\dot{\nu}$ with amplitudes ranging between $\delta\dot{\nu} = 10^{-19}$ to 10^{-15} s^{-2} . This would be easily discernable using the Gaussian process regression framework that we employed.

5.3 Quasi-periodic variability

Among our broader sample there exists a sub-group of 45 pulsars that display striking quasi-periodic oscillations in their spin-down timeseries. These pulsars were predominantly identified through a combination of visual inspection of their timing residuals, spin-down timeseries and Lomb-Scargle periodograms. This group includes five that were previously identified by Lyne et al. (2010) and Kerr et al. (2016). Modulation periods (\mathcal{P}) listed in Table 1 were recovered from Lomb-Scargle periodograms generated from their spin-down timeseries. We failed to recover the sub-annual periodicities of 120 d and 123 d in PSRs J1646–4346 and J1825–1446 that were found by Kerr et al. (2016). This may be due to a combination of our extended timing baselines and differences in methodology. Ten of the pulsars in Table 1 display both long and short modulation timescales that may be harmonically related. The ‘long’ modulation periods in PSRs J1136–5525, J1243–6423, J1649–4653, J1705–4306 and J1830–1059 are either close to or exactly twice the duration of the corresponding ‘short’ periods in these pulsars. Hence, the short periods may be second harmonics. In comparison the dual modulation timescales in PSRs J1056–6258 J1224–6407, J1326–6700, J1600–5751 and J1722–3712 display approximate fractional relations of 5/2, 7/4, 9/5, 3/2 and 7/5 respectively.

Quasi-periodicities in the timing of several pulsars have been known about for decades, with free-precession often being invoked as the ‘clock’ responsible for driving the oscillations (e.g. Stairs et al. 2000). Free precession has also been postulated as the driver of the helical structure in the X-ray jet from the Vela pulsar (Durant et al. 2013) and periodic variations in the inferred magnetic inclination angle of a radio-loud magnetar (Desvignes et al. 2024). The discovery of short-timescale mode switching in these variable pulsars has been argued as evidence against free-precession with the correlation between profile shape and spin-down changes resulting from pulsars preferentially spending a greater amount of time in one magnetospheric state over another (Lyne et al. 2010; Stairs et al. 2019). However, Jones (2012) pointed out that free-precession may act as a trigger for the delicately balanced pulsar magnetospheres to move between different emission states. In doing so, the observational effects of precession are amplified.

Several possible scaling relations between the free-precession induced modulation quasi-periods (\mathcal{P}) were derived by Jones (2012) for various mechanisms that could result in deviations in the neutron star shape away from axisymmetry. Relaxation of the crust or magnetic deformation were excluded as possible mechanisms on the basis that the resulting modulation periods were far in excess of those observed among the Lyne et al. (2010) sample. Precession driven by elastic strain gives rise to a simple relation with spin period (P) of $P/\mathcal{P} = 5 \times 10^{-9}$, which both the Lyne et al. (2010) and an extended sample analysed by Kerr et al. (2016) largely follow. Yet this relation does not appear to hold for our much larger quasi-periodic pulsar sample in Table 1. Our larger sample of modulation periods shown in Figure 9 does not display a strong dependence on the pulsar spin period. The amount of scatter becomes even larger when considering the apparent quasi-periods among the full sample of pulsars shown in

Table 1. List of pulsars with highly quasi-periodic spin-down variations and their associated modulation periods.

PSR	$\mathcal{P}_{\text{short}}$ (d)	$\mathcal{P}_{\text{long}}$ (d)	$\mathcal{P}_{\text{single}}$ (d)
J0255–5304 (B0254–53)	-	-	1648
J0614+2229 (B0611+22)	-	-	268
J1056–6258 (B1054–62)	177	457	-
J1136–5525 (B1133–55)	598	1141	-
J1224–6407 (B1221–63)	427	747	-
J1243–6423 (B1240–64)	626	1203	-
J1306–6617 (B1303–66)	-	-	1522
J1326–5859 (B1323–58)	-	-	1272
J1326–6700 (B1322–66)	232	437	-
J1327–6301 (B1323–627)	-	-	712
J1327–6400	-	-	1505
J1352–6803	-	-	508
J1418–3921	-	-	911
J1428–5530 (B1424–55)	-	-	1395
J1514–5925	-	-	258
J1534–5405 (B1530–539)	-	-	856
J1548–5607	-	-	1056
J1600–5044 (B1557–50)	-	-	1549
J1600–5751 (B1556–57)	477	739	-
J1601–5335	-	-	1098
J1626–4807	-	-	277
J1637–4642	-	-	187
J1611–5209 (B1607–52)	-	-	1671
J1638–4417	-	-	982
J1638–4608	-	-	478
J1649–4653	1214	2541	-
J1702–4306	-	-	392
J1705–3950	157	314	-
J1716–4005	-	-	627
J1717–3425 (B1714–34)	-	-	1422
J1717–5800	-	-	562
J1726–3530	-	-	1066
J1722–3632	-	-	438
J1722–3712	105	148	-
J1739–3023	-	-	235
J1801–2154	-	-	170
J1807–0847 (B1804–08)	-	-	988
J1816–2650 (B1813–26)	-	-	1765
J1829–1751 (B1826–17)	-	-	807
J1830–1059 (B1828–11)	221	456	-
J1835–0944	-	-	524
J1853–0004	-	-	2118
J1853+0011	-	-	484
J1941–2602 (B1937–26)	-	-	1098
J2346–0609	-	-	966

grey. The Spearman rank correlation coefficient of $r_s = 0.03$ (p-value = 0.8) indicates no correlation between these two values. Performing a power-law fit to our sample of modulation periods and spin-periods returns the scaling relation

$$\mathcal{P} = 10^{0.3 \pm 0.1} \text{ yr} \left(\frac{P}{1 \text{ s}} \right)^{0.2 \pm 0.2}, \quad (10)$$

which is inconsistent with the free-precession relation. While it is consistent with the $\mathcal{P} \approx 1.4 \text{ yr} (P/1 \text{ s})^{1/2} (\lambda/10^6 \text{ cm})$ scaling relation predicted for Tkachenko waves when assuming an oscillation wavelength of $2 \times 10^6 \text{ cm}$ at the 95% confidence interval (see figure 5 in Jones 2012), this is likely just a coincidence given the scatter among our measurements. We find similar inconsistencies with the

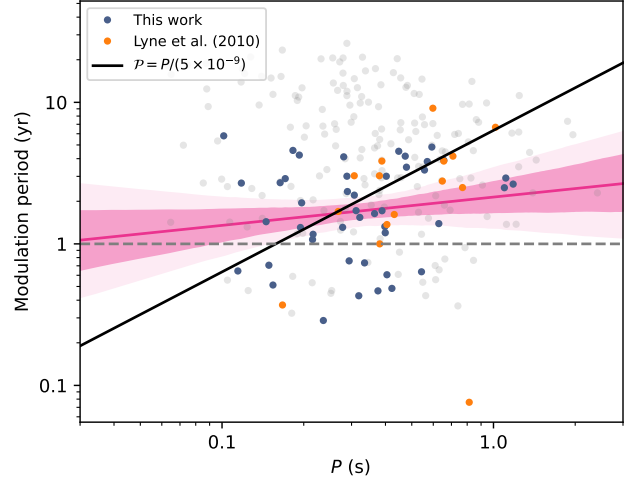


Figure 9. Comparison of spin-down modulation period with P . Grey points are the dominant quasi-periods of all pulsars indicated by their Lomb-Scargle periodograms. Dark blue points indicate the highly quasi-periodic pulsars listed in Table 1, while the orange points are from Table 15 of Lyne et al. (2010). The solid black curve is the $P/\mathcal{P} = 5 \times 10^{-9}$ relation for freely precessing pulsars from Jones (2012), while the pink line and shading indicates our median fit along with the 68% and 95% confidence intervals. The dashed horizontal line indicates a quasi-period of 1 yr.

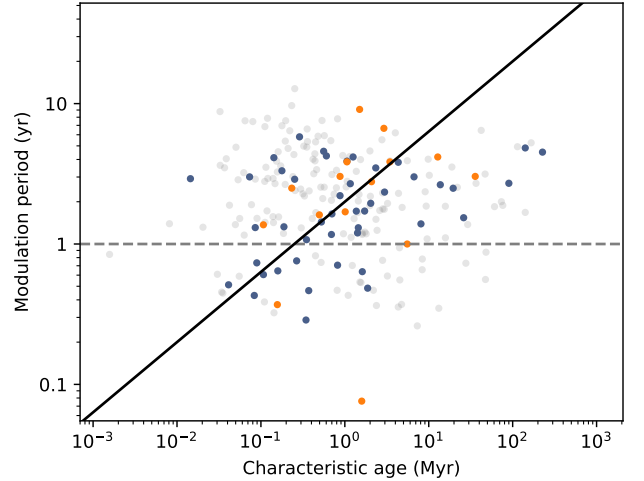


Figure 10. As Figure 9, but for pulsar characteristic age (τ_c). The solid black line indicates the relation from equation 42 of Jones (2012) for $H_c = 10^{15} \text{ G}$.

proposed scaling with τ_c for precession due to a superconducting core. In Figure 10 we show the highly scattered measurements do not follow the predicted relationship, with a Spearman coefficient of $r_s = 0.04$ (p-value = 0.8). We also do not recover the relation with \dot{E} tentatively identified by Kerr et al. (2016), as shown in Figure 11 where $r_s = -0.02$ (p-value = 0.9).

The lack of consistency between our much larger sample of pulsars with quasi-period $\dot{\nu}$ variations and these predicted relations suggests that simple models of elastic strain or superconductivity driven free precession are not the dominant drivers of this behaviour. Jones (2012) noted that the relationships with P required all pulsars display similar levels of strain in their crusts, while superconductivity

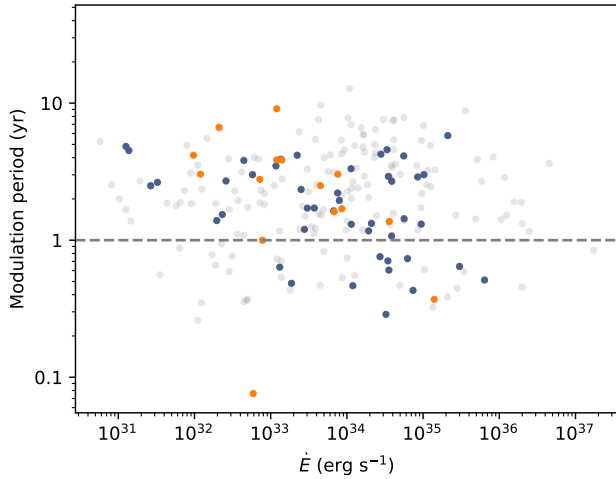


Figure 11. As Figure 9, but for spin-down energy (\dot{E}).

necessitated that the entire star undergo precession. Relaxing these assumptions would resolve these two issues, but would be difficult to falsify. Another complicating factor is the presence of glitches among many of these pulsars, which can arise from interactions between the internal superfluid and the crust. Pinning of superfluid vortices within the crust is expected to dampen free-precession on relatively short timescales (Jones & Andersson 2001; Link & Epstein 2001; Jones et al. 2017). Non-radial oscillation modes of varying velocities and amplitudes have been suggested as an alternate means of driving changes in pulsar emission and spin-down, though without a clear mechanism (Rosen et al. 2011). Hall waves launched by transient events both in the superfluid core and crust of neutron stars have been recently proposed as a means of generating long-term quasi-periodic oscillations in $\dot{\nu}$ that affect the inferred pulsar braking index (Bransgrove et al. 2025). The periods of the waves investigated are significantly longer (1–100 kyr) than the quasi-periodic processes we observe, but shorter period waves could be launched by starquakes acting as glitch triggers (Bransgrove et al. 2020).

5.4 Transient events and interactions with planetesimals

One mechanism that has been previously highlighted as a means for triggering both short-lived transient and persistent step-changes in $\dot{\nu}$ are interactions between a pulsar and infalling small objects, such as asteroids (Brook et al. 2014, 2016; Lower et al. 2023). In this scenario, a minor body falls towards the pulsar and is vaporised by the extreme high-energy electromagnetic radiation environment and intense particle wind surrounding the neutron star. The ionised remains of this object are then funnelled onto the magnetic poles of the pulsar, altering the plasma content which in-turn enhances/attenuates the existing radio emission, or activates new regions above the magnetic poles. These modifications to the magnetospheric plasma will also alter the torque acting to slow the neutron star over time. The altered emission and spin-down would then decay back to the original state as the excess of charged particles from the ionised body dissipates. Assuming the infalling object is completely ionised, we can infer the resulting change in magnetospheric charged particle density from the step change in $\dot{\nu}$ via (Kramer et al. 2006)

$$\Delta\rho = \frac{3I\delta\dot{\nu}}{R_{\text{pc}}^4 B_0}, \quad (11)$$

where $I = 10^{45} \text{ g cm}^2$ is the canonical neutron star moment of inertia, $R_{\text{pc}} = \sqrt{2\pi R^3 \dot{\nu}/c}$ is the polar cap radius (we assume a standard neutron star radius of $R = 10^6 \text{ cm}$) and $B_0 = 3.2 \times 10^{19} \text{ G} \sqrt{-\dot{\nu}/\nu^3}$ is the surface magnetic field strength assuming the pulsar is spinning down purely via dipole radiation. The mass of the ionised minor body can then be determined from (Brook et al. 2014)

$$m = c \Delta\rho R_{\text{pc}} \Delta t, \quad (12)$$

where c is the vacuum speed of light and Δt is the duration in which the pulsar remains in the altered spin-down state.

Out of the 238 pulsars in Figure 3 with variable spin-down rates, we were able to visually identify 68 individual transient spin-down events in 26 pulsars. The absolute size and duration of these $\dot{\nu}$ events along with the inferred asteroid masses are listed in Table A3. We caution that this sample is incomplete to small transient changes in $\dot{\nu}$, which are inherently difficult to distinguish from other stochastic variations and sinusoidal changes in $\dot{\nu}$ arising from residual positional offsets. Comparing the putative asteroid masses, the smallest resulted in the second event in PSR J1833–0827 with $m \sim 2.6 \times 10^{11} \text{ g}$. The third (MJD 54600–55400) event in PSR J1602–5100 is the largest with a mass of $5.32 \times 10^{14} \text{ g}$. This is however smaller than the $\sim 3 \times 10^{15} \text{ g}$ mass inferred for the large 2005 spin-down/profile event detected in PSR J0738–4042 (Brook et al. 2014; Lower et al. 2023). Under the simplifying assumption that these objects were approximately spherical and C-type (carbonaceous) asteroids with a density of $\sim 1.57 \text{ g cm}^{-3}$ (Carry 2012), the computed diameters range between 6.8×10^3 to $7.5 \times 10^4 \text{ cm}$ and $1.5 \times 10^6 \text{ cm}$ for the 2005 event in PSR J0738–4042. Objects within this size range are exceedingly common among main-belt asteroids in the Solar System (Durda et al. 1998). If these transient spin-down events are indeed the result of pulsar-asteroid interactions, then their prevalence implies that debris discs and asteroids orbiting pulsars should be relatively common. Previous searches for planetesimals orbiting pulsars have largely been unsuccessful, though the lowest accessible mass ranges of these searches have been predominantly limited by the achieved timing precision. Surveys of hundreds of slow pulsars placed stringent limits on the presence of orbiting bodies larger than the mass of Mercury (Kerr et al. 2015; Nițu et al. 2022), while analyses of millisecond pulsar timing arrays have pushed these limits to between ~ 0.001 –1 Lunar masses (Behrens et al. 2020; Nițu et al. 2024). These limits are several orders of magnitude higher than the putative asteroid masses listed in Table A3.

Exactly where these asteroids would have originated remains an open question. Fall-back of supernova material and relic discs from the progenitor stellar system are both popular mechanisms for producing asteroid belts around pulsars (Michel 1988). However the high kick velocities measured across the pulsar population present a challenge to these scenarios (Hobbs et al. 2005). Stripping of material from a (former) companion star by a kicked neutron star is one means of forming a disc around high-velocity pulsars, though the expected rate of such interactions is vanishingly small for natal kicks below $\lesssim 600 \text{ km s}^{-1}$ (see Figure 10 in Hirai & Podsiadlowski 2022). The longevity of debris discs around pulsars and condensation rate of objects is also subject to other factors, such as a reduction in pulsar wind energy due to pulsar spin-down evolution (Menou et al. 2001).

Interactions with free-floating interstellar objects (ISOs) similar to 1I/Oumuamua and 2I/Borisov may present another possible origin for these events. Direct impacts between minor bodies and neutron stars have been proposed as a potential mechanism for producing both gamma-ray bursts (GRBs; Newman & Cox 1980) and fast radio bursts (FRBs; Geng & Huang 2015; Dai et al. 2016). The ISO/neutron star collision rate of $\sim 10^7 \text{ Gpc}^{-3} \text{ yr}^{-1}$ (or $\sim 10^{-7} \text{ yr}^{-1}$ for an individual

neutron star) derived by [Pham et al. \(2024\)](#) is consistent with the observed all-sky FRB rate of $(7^{+9}_{-6}) \times 10^7 \text{ Gpc}^{-3} \text{ yr}^{-1}$ ([Bochenek et al. 2020](#)). Such collisions would avoid the challenges associated with forming or retaining asteroid belts around high-velocity pulsars. To test this scenario we computed the rate of observed transient spin-down events occur in our pulsar sample. For $n_{|\delta\dot{\nu}|} = 70$ events observed in $f_{|\delta\dot{\nu}|} = 27/260$ pulsars (note, this includes the two events in PSR J0738–4042) over a total accumulated monitoring time of $T_{\text{acc}} = 4095.6 \text{ yr}$, the rate can be derived as

$$N_{|\delta\dot{\nu}|} \propto (n_{|\delta\dot{\nu}|}/T_{\text{acc}}) \times f_{|\delta\dot{\nu}|} \sim 0.002 \text{ yr}^{-1}. \quad (13)$$

This is over four orders of magnitude higher than the per-pulsar rate from [Pham et al. \(2024\)](#). While their rate is an underestimate due to not taking into account interactions between infalling ISOs and pulsar radiation beams or evaporation from high-energy flux and particle winds, it would likely remain difficult to fully reconcile the difference. Many of these pulsars display repeat transient spin-down events which is also inconsistent with the implied per-pulsar ISO collision rate. Other tests, such as the detection of FRBs from our pulsar sample, are impractical given the short duration of our Parkes observations and monthly cadence. There are however no reports of GRBs detected by all-sky monitors as having originated from any of our pulsars.

Gravitational scattering of ISOs on hyperbolic encounters can produce cuspy signals in pulsar timing residuals, where the sharpness and sign of the cusp depends on the viewing geometry and periastron distance, and the amplitude on the ISO mass ([Jennings et al. 2020a](#)). Close encounters of around 1 AU can produce signals that can appear indistinguishable from a glitch given a low observation cadence. More distant interactions would result in a more rounded peak, strikingly similar to those associated with the timing events in several pulsars displayed in Figure 2. However, given the linear scaling between the timing perturbation and ISO mass (Equation 16 in [Jennings et al. 2020a](#)), we can infer that interactions ISOs with masses equivalent to that of gas giant planets (i.e $\sim 10^{-4} M_{\odot}$) would be required to reproduce the peaks of between 10's-100's of milliseconds seen among our pulsar sample. It is also unclear how such distant encounters would alter the radio emission mechanism of the pulsar.

6 CONCLUSIONS

We have used a combination of Gaussian process regression and Bayesian inference techniques to demonstrate that variations in profile shape and spin-down rate are pervasive among the population of radio pulsars. Our sample of 238 pulsars with significant fluctuations in spin-down and 52 pulsars that display profile shape changes is the largest assembled to date. These include 29 pulsars for which we describe the links between their variable emission and spin-down for the first time. Using the inferred min/max differences in spin-down rate timeseries, we demonstrated the $\dot{\nu}$ variability amplitude scales with spin-down rate according to $\delta\dot{\nu} \propto 10^{-4.5} |\dot{\nu}_{\text{weak}}|^{0.85}$. No substantial dependence on spin-frequency was identified, which could have strong implications for the prevalence of these behaviours in millisecond pulsars if they follow the a similar scaling relation with spin-down rate. Manifestation of spin-down variations in millisecond pulsar timing arrays could leak into the detected common signal seen, as the resulting non-stationary noise process are not well characterised by standard power-law red noise models. Properly accounting for this effect may both improve gravitational-wave searches, and resolve challenges surrounding the apparent time-dependence of

the putative gravitational-wave signal, motivating the application of the spin-down modelling to determine whether this effect is present among these pulsars.

Alongside this, we showed that the various expected scaling relations from models of free-precession, a popular mechanism for producing highly quasi-periodic changes in profile shape and spin-down, are unable to fully account for the large spread in modulation periods seen among a sub-group of 45 pulsars that display extremely (quasi-)periodic spin-down rate (and occasionally, profile shape) variations. This lends weight towards a magnetospheric state-switching origin for the quasi-periodic effects. We also re-examined interactions between pulsars and infalling planetesimals as a means of producing transient changes in profile and spin-down rate among 26 pulsars. Direct collisions and hyperbolic flybys of interstellar objects are ruled out, with the rate of transient spin-down events among these pulsars being four orders of magnitude higher than the theoretical impact rate, whereas repeat flybys of Jupiter-mass objects are required to explain the multiple large transient events seen in individual pulsars. Disruption of infalling asteroids from debris disks orbiting these pulsars remains a valid explanation. Assuming C-type composition asteroids, the masses and radii inferred from the amplitude and duration of these events are consistent with planetesimals that are prevalent in our Solar System. Future direct detections of thermal emission from asteroid belts and debris disks around these pulsars via deep infrared or sub-mm observations would lend substantial weight towards this hypothesis. A purely magnetospheric origin for these behaviours cannot be ruled out at present.

An apparent deficit in the number of pulsars displaying profile shape changes, despite showing clear $\dot{\nu}$ variations, is largely due to a combination of relatively low per-epoch signal-to-noise ratios, short observations resulting in stochastic jitter-dominated shape changes and smearing of profile components by scatter-broadening in the interstellar medium. Similar challenges to identifying profile-shape changing pulsars have been faced by other large-scale timing programmes. This includes the Thousand Pulsar Array on MeerKAT, where few new shape-changing pulsars have been identified to date despite the substantially higher telescope gain over Murriyang ([Basu et al. 2024](#)). Increasing this population could be achieved through a re-optimisation of existing programmes and those proposed to take place using the SKA. Lengthening the duration of each pulsar observation would reduce the impact of pulse-to-pulse jitter, and make such programmes sensitive to more subtle shape changes.

ACKNOWLEDGEMENTS

Murriyang, the Parkes radio telescope, is part of the Australia Telescope National Facility (<https://ror.org/05qajvd42>) which is funded by the Australian Government for operation as a National Facility managed by CSIRO. We acknowledge the Wiradjuri people as the traditional owners of the Observatory site. This project was supported by resources and expertise provided by CSIRO IMT Scientific Computing. Some of the data analysis behind this work was performed using the OzSTAR national HPC facility, which is funded by Swinburne University of Technology and the National Collaborative Research Infrastructure Strategy (NCRIS). MEL is supported by an Australian Research Council (ARC) Discovery Early Career Research Award DE250100508. PRB is supported by the UK Science and Technology Facilities Council (STFC), grant number ST/W000946/1. RMS acknowledges support through ARC Future Fellowship FT190100155. Part of the work was undertaken with support from the ARC Centre of Excellence for Gravitational Wave Dis-

covery (OzGrav; CE170100004 and CE230100016). Work at NRL is supported by NASA. Pulsar research at the Jodrell Bank Centre for Astrophysics is supported by a consolidated grant from the UK STFC. This work has made use of NASA's Astrophysics Data System, and the following open-source software packages that were not cited elsewhere: `MATPLOTLIB` (Hunter 2007), `NUMPY` (Harris et al. 2020) and `SCIPY` (Virtanen et al. 2020). MEL is grateful to the hospitality of St Edmund Hall during visits to Oxford throughout this project.

DATA AVAILABILITY

The raw data is available to download via the CSIRO Data Access Portal (<https://data.csiro.au/>) following an 18-month proprietary period. Other data products are available upon reasonable request to the corresponding author.

REFERENCES

- Agazie G., et al., 2023a, *ApJ*, **951**, L8
- Agazie G., et al., 2023b, *ApJ*, **951**, L8
- Akbal O., Gügürcinoğlu E., Şaşmaz Muş S., Alpar M. A., 2015, *MNRAS*, **449**, 933
- Ambikasaran S., Foreman-Mackey D., Greengard L., Hogg D. W., O'Neil M., 2015, *IEEE Transactions on Pattern Analysis and Machine Intelligence*, **38**, 252
- Ashton G., et al., 2019, *ApJS*, **241**, 27
- Backer D. C., 1970a, *Nature*, **228**, 42
- Backer D. C., 1970b, *Nature*, **228**, 752
- Backer D. C., 1970c, *Nature*, **228**, 1297
- Basu A., et al., 2022, *MNRAS*, **510**, 4049
- Basu A., et al., 2024, *MNRAS*, **528**, 7458
- Behrens E. A., et al., 2020, *ApJ*, **893**, L8
- Biggs J. D., 1986, PhD thesis, The University of Sydney, Australia
- Biggs J. D., 1990, *MNRAS*, **246**, 341
- Biggs J. D., 1992, *ApJ*, **394**, 574
- Bochenek C. D., Ravi V., Belov K. V., Hallinan G., Kocz J., Kulkarni S. R., McKenna D. L., 2020, *Nature*, **587**, 59
- Bransgrove A., Beloborodov A. M., Levin Y., 2020, *ApJ*, **897**, 173
- Bransgrove A., Levin Y., Beloborodov A. M., 2025, *ApJ*, **979**, 144
- Brook P. R., Karastergiou A., Buchner S., Roberts S. J., Keith M. J., Johnston S., Shannon R. M., 2014, *ApJ*, **780**, L31
- Brook P. R., Karastergiou A., Johnston S., Kerr M., Shannon R. M., Roberts S. J., 2016, *MNRAS*, **456**, 1374
- Brook P. R., et al., 2018, *ApJ*, **868**, 122
- Carry B., 2012, *Planet. Space Sci.*, **73**, 98
- Chen J. L., et al., 2023, *MNRAS*, **519**, 2709
- Chukwude A. E., Buchner S., 2012, *ApJ*, **745**, 40
- Chukwude A. E., Ubachukwu A. A., Okeke P. N., 2003, *A&A*, **399**, 231
- Cordes J. M., Downs G. S., 1985, *ApJS*, **59**, 343
- Cordes J. M., Greenstein G., 1981, *ApJ*, **245**, 1060
- Dai Z. G., Wang J. S., Wu X. F., Huang Y. F., 2016, *ApJ*, **829**, 27
- Desvignes G., et al., 2024, *Nature Astronomy*, **8**, 617
- Detweiler S., 1979, *ApJ*, **234**, 1100
- Dewey R. J., Cordes J. M., 1989, in Ögelman H., van den Heuvel E. P. J., eds, *NATO Advanced Study Institute (ASI) Series C Vol. 262, Timing Neutron Stars*. p. 119, doi:10.1007/978-94-009-2273-0_7
- Durant M., Kargaltsev O., Pavlov G. G., Kropotina J., Levenfish K., 2013, *ApJ*, **763**, 72
- Durda D. D., Greenberg R., Jedicke R., 1998, *Icarus*, **135**, 431
- EPTA Collaboration et al., 2023a, *A&A*, **678**, A48
- EPTA Collaboration et al., 2023b, *A&A*, **678**, A50
- Espinoza C. M., Lyne A. G., Kramer M., Manchester R. N., Kaspi V. M., 2011, *ApJ*, **741**, L13
- Espinoza C. M., Kuiper L., Ho W. C. G., Antonopoulou D., Arzoumanian Z., Harding A. K., Ray P. S., Younes G., 2024, *arXiv e-prints*, p. arXiv:2409.10759
- Fowler L. A., Wright G. A. E., 1982, *A&A*, **109**, 279
- Fowler L. A., Wright G. A. E., Morris D., 1981, *A&A*, **93**, 54
- Freire P. C. C., Wex N., 2024, *Living Reviews in Relativity*, **27**, 5
- Frescura F., Flanagan C. S., 2003, in Bailes M., Nice D. J., Thorsett S. E., eds, *Astronomical Society of the Pacific Conference Series Vol. 302, Radio Pulsars*. p. 237
- Gaensler B. M., Arons J., Kaspi V. M., Pivovarov M. J., Kawai N., Tamura K., 2002, *ApJ*, **569**, 878
- Geng J. J., Huang Y. F., 2015, *ApJ*, **809**, 24
- Goncharov B., et al., 2021, *MNRAS*, **502**, 478
- Granet C., et al., 2001, in *IEEE Antennas and Propagation Society International Symposium. 2001 Digest. Held in conjunction with: USNC/URSI National Radio Science Meeting (Cat. No.01CH37229)*. pp 296–299, doi:10.1109/APS.2001.959722
- Granet C., Bowen M., Reynolds J., Davis I. M., Kot J. S., Pope G., 2011, in *Proceedings of the 5th European Conference on Antennas and Propagation (EUCAP)*. pp 918–920
- Harris C. R., et al., 2020, *Nature*, **585**, 357
- Hermesen W., et al., 2013, *Science*, **339**, 436
- Hermesen W., et al., 2017, *MNRAS*, **466**, 1688
- Hermesen W., et al., 2018, *MNRAS*, **480**, 3655
- Hirai R., Podsiadlowski P., 2022, *MNRAS*, **517**, 4544
- Hobbs G., et al., 2002, *MNRAS*, **333**, L7
- Hobbs G., Lorimer D. R., Lyne A. G., Kramer M., 2005, *MNRAS*, **360**, 974
- Hobbs G. B., Edwards R. T., Manchester R. N., 2006, *MNRAS*, **369**, 655
- Hobbs G., Lyne A. G., Kramer M., 2010, *MNRAS*, **402**, 1027
- Hobbs G., et al., 2011, *Publ. Astron. Soc. Australia*, **28**, 202
- Hobbs G., et al., 2020, *Publ. Astron. Soc. Australia*, **37**, e012
- Hotan A. W., van Straten W., Manchester R. N., 2004, *Publ. Astron. Soc. Australia*, **21**, 302
- Hunter J. D., 2007, *Computing in Science & Engineering*, **9**, 90
- Jennings R. J., Cordes J. M., Chatterjee S., 2020a, *ApJ*, **889**, 145
- Jennings R. J., Cordes J. M., Chatterjee S., 2020b, *ApJ*, **904**, 191
- Jennings R. J., et al., 2024, *ApJ*, **964**, 179
- Johnston S., Lower M. E., 2021, *MNRAS*, **507**, L41
- Johnston S., van Straten W., Kramer M., Bailes M., 2001, *ApJ*, **549**, L101
- Johnston S., et al., 2021, *MNRAS*, **502**, 1253
- Johnston S., Kramer M., Karastergiou A., Keith M. J., Oswald L. S., Parthasarathy A., Weltevrede P., 2023, *MNRAS*, **520**, 4801
- Jones D. I., 2012, *MNRAS*, **420**, 2325
- Jones D. I., Andersson N., 2001, *MNRAS*, **324**, 811
- Jones D. I., Ashton G., Prix R., 2017, *Phys. Rev. Lett.*, **118**, 261101
- Karastergiou A., Roberts S. J., Johnston S., Lee H., Weltevrede P., Kramer M., 2011, *MNRAS*, **415**, 251
- Keith M. J., Nitu I. C., 2023, *MNRAS*, **523**, 4603
- Keith M. J., Shannon R. M., Johnston S., 2013, *MNRAS*, **432**, 3080
- Kerr M., Hobbs G., Shannon R. M., Kiczynski M., Hollow R., Johnston S., 2014, *MNRAS*, **445**, 320
- Kerr M., Johnston S., Hobbs G., Shannon R. M., 2015, *ApJ*, **809**, L11
- Kerr M., Hobbs G., Johnston S., Shannon R. M., 2016, *MNRAS*, **455**, 1845
- Kramer M., Champion D. J., 2013, *Classical and Quantum Gravity*, **30**, 224009
- Kramer M., Lyne A. G., O'Brien J. T., Jordan C. A., Lorimer D. R., 2006, *Science*, **312**, 549
- Lam M. T., et al., 2018, *ApJ*, **861**, 132
- Lentati L., Alexander P., Hobson M. P., Feroz F., van Haasteren R., Lee K. J., Shannon R. M., 2014, *MNRAS*, **437**, 3004
- Li X.-D., 2006, *ApJ*, **646**, L139
- Link B., Epstein R. I., 2001, *ApJ*, **556**, 392
- Liu P., et al., 2024, *MNRAS*, **533**, 4274
- Livingstone M. A., Kaspi V. M., 2011, *ApJ*, **742**, 31
- Lower M. E., et al., 2020, *MNRAS*, **494**, 228
- Lower M. E., et al., 2021, *MNRAS*, **508**, 3251
- Lower M. E., et al., 2023, *MNRAS*, **524**, 5904
- Lyne A. G., 1971, *MNRAS*, **153**, 27P

- Lyne A., Hobbs G., Kramer M., Stairs I., Stappers B., 2010, *Science*, **329**, 408
- Mahajan N., van Kerkwijk M. H., Main R., Pen U.-L., 2018, *ApJ*, **867**, L2
- Manchester R. N., IPTA 2013, *Classical and Quantum Gravity*, **30**, 224010
- Manchester R. N., Hobbs G. B., Teoh A., Hobbs M., 2005, *AJ*, **129**, 1993
- Manchester R. N., et al., 2013, *Publ. Astron. Soc. Australia*, **30**, e017
- Maritz J., Meintjes P. J., Sarah B., Lewandowska N., 2015, in 3rd Annual Conference on High Energy Astrophysics in Southern Africa (HEASA2015), p. 30, doi:10.22323/1.241.0030
- McLaughlin M. A., 2013, *Classical and Quantum Gravity*, **30**, 224008
- Menou K., Perna R., Hernquist L., 2001, *ApJ*, **559**, 1032
- Michel F. C., 1988, *Nature*, **333**, 644
- Miles M. T., Shannon R. M., Bailes M., Reardon D. J., Buchner S., Middleton H., Spiewak R., 2022, *MNRAS*, **510**, 5908
- Miles M. T., et al., 2025a, *MNRAS*, **536**, 1467
- Miles M. T., et al., 2025b, *MNRAS*, **536**, 1489
- Namkham N., Jaroenjittichai P., Johnston S., 2019, *MNRAS*, **487**, 5854
- Nathan R. S., Miles M. T., Ashton G., Lasky P. D., Thrane E., Reardon D. J., Shannon R. M., Cameron A. D., 2023, *MNRAS*, **523**, 4405
- Newman M. J., Cox A. N., 1980, *ApJ*, **242**, 319
- Nițu I. C., Keith M. J., Stappers B. W., Lyne A. G., Mickaliger M. B., 2022, *MNRAS*, **512**, 2446
- Nițu I. C., et al., 2024, *MNRAS*, **534**, 1753
- Palfreyman J., Dickey J. M., Hotan A., Ellingsen S., van Straten W., 2018, *Nature*, **556**, 219
- Parthasarathy A., et al., 2019, *MNRAS*, **489**, 3810
- Parthasarathy A., et al., 2020, *MNRAS*, **494**, 2012
- Pedregosa F., et al., 2011, *Journal of Machine Learning Research*, **12**, 2825
- Petroff E., Keith M. J., Johnston S., van Straten W., Shannon R. M., 2013, *MNRAS*, **435**, 1610
- Pham D., Hopkins M. J., Lintott C., Bannister M. T., Rein H., 2024, *arXiv e-prints*, p. arXiv:2411.09135
- Reardon D. J., et al., 2023, *ApJ*, **951**, L6
- Rosen R., McLaughlin M. A., Thompson S. E., 2011, *ApJ*, **728**, L19
- Sazhin M. V., 1978, *Soviet Ast.*, **22**, 36
- Shabanova T. V., 2005, *MNRAS*, **356**, 1435
- Shabanova T. V., 2009, *ApJ*, **700**, 1009
- Shabanova T. V., Lyne A. G., Urama J. O., 2001, *ApJ*, **552**, 321
- Shannon R. M., Cordes J. M., 2010, *ApJ*, **725**, 1607
- Shannon R. M., et al., 2013, *ApJ*, **766**, 5
- Shannon R. M., et al., 2016, *ApJ*, **828**, L1
- Shaw B., et al., 2022, *MNRAS*, **513**, 5861
- Smith D. A., et al., 2023, *ApJ*, **958**, 191
- Speagle J. S., 2020, *MNRAS*, **493**, 3132
- Stairs I. H., Lyne A. G., Shemar S. L., 2000, *Nature*, **406**, 484
- Stairs I. H., et al., 2019, *MNRAS*, **485**, 3230
- Staveley-Smith L., et al., 1996, *Publ. Astron. Soc. Australia*, **13**, 243
- Virtanen P., et al., 2020, *Nature Methods*, **17**, 261
- Weltevrede P., Wright G. A. E., Stappers B. W., 2007, *A&A*, **467**, 1163
- Weltevrede P., et al., 2010, *Publ. Astron. Soc. Australia*, **27**, 64
- Weltevrede P., Johnston S., Espinoza C. M., 2011, *MNRAS*, **411**, 1917
- Weltevrede P., Wright G., Johnston S., 2012, *MNRAS*, **424**, 843
- Wen Z. G., et al., 2020, *ApJ*, **904**, 72
- Xu H., et al., 2023, *Research in Astronomy and Astrophysics*, **23**, 075024
- Yan W. M., Manchester R. N., Wang N., Wen Z. G., Yuan J. P., Lee K. J., Chen J. L., 2020, *MNRAS*, **491**, 4634
- Yuan Y., Levin Y., Bransgrove A., Philippov A., 2021, *ApJ*, **908**, 176
- Zhang Y. R., Wang H. G., Huang X. J., Chen J. L., 2020, *ApJ*, **890**, 31
- Zic A., et al., 2023, *Publ. Astron. Soc. Australia*, **40**, e049
- van Straten W., Demorest P., Osłowski S., 2012, *Astronomical Research and Technology*, **9**, 237

APPENDIX A: SPIN-DOWN MODEL PARAMETERS AND INFERRED MAGNETOSPHERIC PROPERTIES

Tables listing the best fit model parameters for the timing residual Gaussian process regression fits, pulsar rotational and derived magnetospheric parameters, and transient spin-down event/asteroid properties.

This paper has been typeset from a \LaTeX file prepared by the author.

Table A1. Results of our Gaussian process fits, including preferred model, Bayesian information criterion, maximum likelihood hyperparameters and corresponding \mathcal{K} -metric. The σ_2^2 and λ_2 parameters are left blank for pulsars where only a single kernel was preferred.

PSR	MJD range	N_{ToA}	ΔBIC	σ_1^2 (s)	λ_1 (d)	σ_2^2 (s)	λ_2 (d)	σ_N^2 (s)	$\ln \mathcal{K}$
J0034-0721	53040-60102	164	10.2	8.9×10^{-7}	915.8	-	-	1.2×10^{-5}	9.5
J0108-1431	49091-60037	312	5.5	9.4×10^{-7}	857.3	-	-	1.1×10^{-6}	8.7
J0134-2937	53972-60101	136	7.3	6.5×10^{-8}	1787.8	-	-	1.9×10^{-12}	18.4
J0152-1637	51874-60102	134	9.7	3.4×10^{-6}	2304.5	-	-	2.4×10^{-8}	13.9
J0206-4028	51874-60102	134	-22.7	5.3×10^{-3}	1945.1	1.0×10^{-7}	63.4	4.6×10^{-8}	7.2
J0255-5304	51530-60100	539	11.8	2.1×10^{-9}	476.8	-	-	4.2×10^{-8}	10.9
J0401-7608	54220-60100	230	-16.7	7.7×10^{-3}	1156.4	4.9×10^{-8}	96.1	8.6×10^{-8}	9.1
J0448-2749	56670-60102	114	9.5	1.2×10^{-7}	119.3	-	-	6.8×10^{-8}	7.0
J0452-1759	54505-60102	168	-4.5	3.6×10^{-8}	66.0	2.6×10^{-5}	446.2	4.3×10^{-8}	9.7
J0525+1115	56741-60078	119	9.4	7.9×10^{-10}	168.8	-	-	5.8×10^{-9}	9.7
J0543+2329	54505-60137	173	-18.9	1.9×10^{-3}	1097.7	1.7×10^{-8}	72.0	1.7×10^{-8}	12.8
J0601-0527	56741-60102	110	8.7	2.6×10^{-8}	200.3	-	-	4.6×10^{-9}	11.6
J0614+2229	54505-60162	174	-170.8	1.9×10^{-4}	65.9	3.0×10^{-1}	359.0	4.0×10^{-7}	10.3
J0627+0706	54318-60162	181	-72.0	4.5×10^{-6}	155.3	8.7×10^{-3}	569.4	5.1×10^{-8}	12.2
J0630-2834	51525-60102	209	-11.2	7.2×10^{-4}	671.6	-	-	3.1×10^{-4}	8.6
J0631+1036	57165-60162	89	-20.9	4.7	1649.3	1.2×10^{-4}	117.6	1.3×10^{-5}	11.2
J0659+1414	53587-60162	177	5.9	8.1×10^{-4}	781.1	-	-	3.8×10^{-7}	15.5
J0729-1448	54220-60162	206	-215.4	2.0×10^{-4}	62.0	2.7	943.3	2.7×10^{-6}	10.9
J0729-1836	53974-60102	167	-61.9	1.3×10^{-2}	539.8	1.3×10^{-6}	94.5	9.5×10^{-8}	10.6
J0742-2822	49025-60162	819	-1688.2	2.3×10^{-5}	62.0	$7.1e+01$	1047.6	1.1×10^{-8}	13.1
J0745-5353	53974-60137	224	-35.0	3.0×10^{-8}	62.0	1.0×10^{-4}	863.0	1.1×10^{-8}	10.9
J0809-4753	56641-60102	116	-1.6	4.0×10^{-8}	144.9	1.8×10^{-5}	479.7	8.3×10^{-9}	10.8
J0820-1350	56746-60078	128	3.1	3.0×10^{-7}	351.1	-	-	5.8×10^{-8}	9.9
J0820-3826	54548-59642	169	-0.9	6.3×10^{-6}	201.6	2.5×10^{-7}	62.0	1.1×10^{-7}	10.8
J0834-4159	51299-59489	229	-21.0	1.0×10^{-2}	2451.9	2.9×10^{-6}	377.5	1.2×10^{-7}	15.0
J0837-4135	56671-60100	117	-11.3	2.8×10^{-8}	137.7	4.8×10^{-5}	627.5	4.1×10^{-9}	10.5
J0842-4851	55363-60162	155	-23.5	9.7×10^{-7}	146.1	5.2×10^{-4}	376.9	2.1×10^{-8}	10.8
J0855-4644	51159-59931	312	-37.8	9.0×10^{-1}	1478.3	1.6×10^{-7}	163.3	1.2×10^{-7}	15.8
J0857-4424	51900-60137	272	-7.0	1.3×10^{-6}	450.0	5.1×10^{-2}	1616.1	8.0×10^{-8}	15.4
J0901-4624	50850-60162	254	-155.7	3.2×10^{-1}	1488.5	8.7×10^{-2}	1898.7	7.1×10^{-6}	15.6
J0904-7459	55984-60078	119	9.6	4.9×10^{-7}	438.8	-	-	3.1×10^{-7}	9.9
J0905-5127	49139-60137	340	-251.5	3.7×10^{-6}	113.0	4.9×10^{-1}	812.0	6.1×10^{-8}	12.3
J0907-5157	56671-60100	139	-17.7	3.2×10^{-4}	941.6	4.4×10^{-8}	62.0	2.4×10^{-8}	9.9
J0908-4913	48861-60162	425	-201.2	2.0×10^{-4}	248.5	$5.8e+01$	2131.8	4.9×10^{-7}	14.8
J0924-5814	56671-60100	137	-4.8	2.6×10^{-5}	358.1	9.4×10^{-1}	1541.7	9.0×10^{-7}	10.1
J0940-5428	50850-60162	319	-270.4	4.3×10^{-5}	150.9	$8.0e+01$	2051.9	5.0×10^{-7}	14.8
J0942-5552	56671-60100	114	-22.2	8.3×10^{-3}	208.8	1.3×10^{-6}	62.0	3.9×10^{-8}	9.3
J0954-5430	50849-60137	252	-59.6	1.8×10^{-4}	722.8	5.1×10^{-7}	144.8	4.8×10^{-8}	13.1
J1001-5507	56671-60100	112	-56.3	4.4×10^{-5}	140.9	6.0×10^{-1}	1151.1	3.4×10^{-8}	9.9
J1003-4747	53974-60162	243	-13.7	3.1×10^{-8}	192.6	1.8×10^{-4}	1431.3	2.5×10^{-8}	12.5
J1015-5719	51216-60162	320	-274.9	1.2×10^{-5}	97.9	2.9×10^{-2}	637.8	1.0×10^{-7}	14.2
J1016-5819	54220-60137	181	3.9	1.3×10^{-6}	776.9	-	-	3.2×10^{-8}	15.9
J1020-6026	52854-56708	111	9.4	3.3×10^{-6}	354.7	-	-	1.1×10^{-6}	13.9
J1038-5831	50537-60100	170	-88.6	7.3×10^{-7}	110.5	1.5×10^{-2}	1005.3	8.6×10^{-8}	7.8
J1043-6116	51159-60137	231	-52.1	2.4×10^{-2}	1493.4	1.2×10^{-7}	154.8	1.3×10^{-8}	13.4
J1047-6709	50986-60100	154	-3.0	6.5×10^{-6}	841.8	8.5×10^{-9}	102.9	1.1×10^{-8}	12.0
J1048-5832	47910-60223	732	-587.8	9.8×10^{-5}	69.2	4.4	532.9	5.6×10^{-7}	13.9
J1052-5954	54220-56708	103	-15.1	6.6×10^{-1}	1003.5	4.9×10^{-4}	62.0	1.5×10^{-5}	8.8
J1055-6022	56053-58531	82	5.9	1.4×10^{-2}	938.3	-	-	3.1×10^{-6}	12.8
J1055-6028	54506-60162	205	-39.0	5.8×10^{-4}	179.7	3.1	1184.1	8.9×10^{-6}	13.3
J1056-6258	56671-60100	111	-26.8	4.0×10^{-5}	381.2	1.0×10^{-6}	86.0	1.1×10^{-8}	9.5
J1057-5226	48814-60162	552	-379.4	5.9×10^{-2}	1249.0	1.3×10^{-10}	2152.5	3.2×10^{-6}	15.3
J1105-6107	49176-60162	415	-414.5	3.0×10^{-5}	80.9	2.1×10^{-2}	62.0	8.1×10^{-1}	8.5
J1112-6103	50940-60162	364	-332.8	2.8×10^{-5}	66.3	7.6	958.5	2.2×10^{-7}	14.0
J1115-6052	50850-60137	248	-87.7	1.1×10^{-7}	110.3	4.7×10^{-4}	927.4	3.1×10^{-8}	12.3
J1123-6259	49542-60137	412	-99.6	1.3×10^{-5}	236.9	3.1×10^{-2}	1046.4	1.1×10^{-7}	12.8
J1136-5525	56672-60100	117	5.5	8.8×10^{-5}	204.0	-	-	2.8×10^{-8}	11.7
J1138-6207	50850-56708	168	-108.7	5.0×10^{-6}	104.2	5.0×10^{-2}	750.6	1.8×10^{-7}	12.8
J1146-6030	56672-60100	112	-2.5	7.3×10^{-6}	716.9	4.4×10^{-8}	142.5	2.4×10^{-9}	11.9
J1156-5707	54220-60137	208	-63.2	1.2×10^{-5}	87.8	1.1	623.0	7.6×10^{-7}	10.9

Table A1 – continued

PSR	MJD range	N_{ToA}	ΔBIC	σ_1^2 (s)	λ_1 (d)	σ_2^2 (s)	λ_2 (d)	σ_N^2 (s)	$\ln \mathcal{K}$
J1157–6224	56672–60100	135	8.0	6.2×10^{-7}	191.1	-	-	5.0×10^{-8}	11.3
J1216–6223	50852–56708	108	8.1	9.6×10^{-4}	1112.4	-	-	5.4×10^{-7}	14.3
J1224–6407	48361–60137	700	-227.8	1.5×10^{-2}	3000.0	9.3×10^{-7}	169.7	1.9×10^{-9}	14.6
J1243–6423	56672–60100	129	-17.9	3.3×10^{-7}	131.5	1.0×10^{-4}	507.9	4.3×10^{-9}	11.6
J1248–6344	51215–56709	123	-8.6	1.3×10^{-6}	130.4	1.8×10^{-3}	1021.4	6.7×10^{-7}	12.4
J1305–6203	50941–60137	208	-1.9	2.9×10^{-5}	751.7	1.2×10^{-1}	3000.0	4.5×10^{-7}	15.1
J1306–6617	56672–60100	109	-7.8	1.1×10^{-3}	669.0	6.4×10^{-7}	157.9	7.0×10^{-8}	10.7
J1317–6302	57165–60100	97	0.1	3.1×10^{-7}	128.6	-	-	2.7×10^{-8}	7.7
J1319–6056	56682–60100	109	-12.2	7.5×10^{-8}	164.6	8.0×10^{-5}	895.9	4.7×10^{-9}	11.7
J1320–5359	50537–60162	298	-73.4	1.1	1993.0	1.8×10^{-7}	171.7	2.2×10^{-8}	13.5
J1326–5859	50242–60100	165	-80.2	8.6×10^{-2}	1828.5	2.0×10^{-5}	191.5	2.4×10^{-8}	10.5
J1326–6408	56682–60100	136	-5.6	1.8×10^{-3}	1526.9	2.0×10^{-8}	99.9	2.5×10^{-8}	9.4
J1326–6700	56682–60100	137	-35.4	9.9×10^{-4}	711.6	7.8×10^{-6}	112.3	2.3×10^{-7}	8.9
J1327–6222	56682–60100	134	-89.1	6.4×10^{-6}	62.0	5.6×10^{-2}	666.1	6.4×10^{-8}	9.3
J1327–6301	56682–60100	110	2.6	4.7×10^{-7}	452.2	-	-	4.2×10^{-9}	14.4
J1327–6400	54220–56709	82	0.0	9.0×10^{-3}	224.7	-	-	4.7×10^{-7}	12.0
J1328–4357	50739–60100	184	-130.3	3.1×10^{-7}	95.5	3.6×10^{-2}	1104.9	3.3×10^{-8}	9.3
J1338–6204	57165–60100	96	4.1	2.6×10^{-4}	553.6	-	-	4.4×10^{-7}	10.7
J1340–6456	57165–60100	120	-3.1	9.8×10^{-5}	391.2	1.6×10^{-6}	124.6	4.1×10^{-7}	9.9
J1349–6130	54220–60137	227	-110.4	7.8×10^{-7}	88.3	7.1×10^{-4}	472.6	2.6×10^{-8}	11.1
J1352–6803	57228–59489	71	7.5	5.1×10^{-6}	249.2	-	-	4.5×10^{-7}	8.4
J1357–62	56682–60100	111	-15.6	1.2×10^{-7}	117.7	5.0×10^{-4}	900.8	1.1×10^{-8}	11.9
J1359–6038	47914–60162	611	-421.2	1.3	1519.9	9.8×10^{-6}	154.3	1.3×10^{-8}	14.6
J1401–6357	56682–60100	111	-32.0	2.4×10^{-5}	165.7	3.2×10^{-2}	578.5	5.7×10^{-8}	10.1
J1412–6145	50850–60137	327	-133.0	3.1×10^{-1}	801.3	2.7×10^{-13}	1090.9	1.6×10^{-6}	15.9
J1418–3921	56682–60100	84	8.9	5.1×10^{-6}	385.8	-	-	5.1×10^{-7}	7.9
J1424–5822	56682–60100	110	-27.3	4.8×10^{-7}	98.1	2.3×10^{-4}	390.0	2.1×10^{-8}	10.1
J1428–5530	56682–60100	112	9.0	1.8×10^{-5}	703.6	-	-	1.5×10^{-7}	11.8
J1430–6623	56682–60100	112	4.6	2.7×10^{-5}	1069.3	-	-	2.6×10^{-9}	13.7
J1435–5954	56682–60100	105	-6.8	2.2×10^{-7}	87.6	8.4×10^{-5}	670.6	1.8×10^{-7}	8.1
J1452–5851	51088–56709	155	-1.6	1.9×10^{-1}	3000.0	6.8×10^{-6}	568.6	4.5×10^{-7}	15.2
J1452–6036	51303–60162	230	-82.2	3.1×10^{-8}	120.5	5.6×10^{-5}	904.0	3.6×10^{-9}	12.8
J1453–6413	54597–60137	221	-34.0	6.2×10^{-6}	378.7	-	-	4.2×10^{-7}	13.3
J1456–6843	48331–60100	351	0.8	6.6×10^{-5}	1938.8	-	-	5.8×10^{-8}	13.4
J1509–5850	51262–60137	296	-2.0	1.1×10^{-5}	560.7	-	-	2.7×10^{-7}	16.9
J1512–5759	52266–60137	233	-127.7	7.7×10^{-3}	790.5	6.4×10^{-6}	147.9	4.9×10^{-9}	14.2
J1513–5908	47914–60137	548	-220.9	1.6×10^{-5}	156.2	9.7×10^{-1}	1164.5	6.2×10^{-7}	18.3
J1514–5925	51221–56709	122	-27.2	5.6×10^{-6}	102.6	3.8×10^{-3}	1179.1	1.7×10^{-7}	10.7
J1515–5720	54220–59517	170	-47.7	7.1×10^{-3}	989.5	4.1×10^{-6}	153.9	5.0×10^{-8}	11.7
J1522–5829	56682–60100	108	7.2	8.4×10^{-8}	125.4	-	-	1.5×10^{-8}	10.4
J1524–5706	51101–60137	246	-17.7	9.4×10^{-5}	970.8	3.7×10^{-7}	135.2	4.1×10^{-7}	12.9
J1530–5327	51014–60137	284	-0.1	5.5×10^{-6}	403.4	1.9×10^{-3}	1741.3	1.8×10^{-7}	13.5
J1534–5405	57165–60078	91	3.7	2.4×10^{-5}	156.4	-	-	1.4×10^{-8}	10.2
J1536–5433	57165–60078	93	4.9	4.2×10^{-2}	1264.4	-	-	2.3×10^{-3}	7.2
J1538–5551	51467–56709	122	9.6	2.3×10^{-5}	489.8	-	-	3.8×10^{-7}	14.3
J1539–5626	48874–60137	415	-144.6	6.5×10^{-7}	98.3	9.0×10^{-4}	383.3	3.1×10^{-8}	11.7
J1541–5535	54220–60162	195	-165.7	6.5×10^{-1}	435.7	6.3×10^{-5}	98.1	3.9×10^{-7}	12.0
J1543–5459	50941–60137	260	-201.7	6.7×10^{-5}	113.5	2.2	661.9	2.9×10^{-7}	11.7
J1544–5308	56682–60100	111	7.1	6.1×10^{-8}	479.6	-	-	1.4×10^{-9}	12.2
J1548–5607	50941–60137	266	-146.1	4.0×10^{-2}	1209.7	8.5×10^{-6}	189.1	5.4×10^{-8}	13.8
J1549–4848	49139–60137	402	-222.7	2.3×10^{-5}	176.5	1.6×10^{-1}	1433.4	1.0×10^{-7}	12.9
J1551–5310	51099–56709	181	-59.5	$3.4e+01$	1157.0	4.5×10^{-3}	187.5	5.7×10^{-6}	12.0
J1557–4258	50539–60079	164	-69.4	3.8×10^{-8}	138.2	1.2×10^{-4}	2026.4	2.4×10^{-9}	10.0
J1559–4438	49559–60079	239	-76.7	5.4×10^{-3}	1897.9	1.1×10^{-7}	233.9	1.2×10^{-8}	12.4
J1600–5044	51945–60162	260	-66.8	2.4×10^{-8}	62.0	2.5×10^{-4}	367.0	5.5×10^{-9}	12.2
J1600–5751	54221–60137	194	-40.1	2.1×10^{-6}	158.6	3.4×10^{-4}	676.1	3.0×10^{-8}	11.8
J1601–5335	50941–56709	155	-54.2	1.5×10^{-5}	147.0	8.1×10^{-2}	649.1	3.3×10^{-7}	12.9
J1602–5100	48296–60162	366	-46.3	2.4×10^{-2}	317.8	4.3	849.8	7.9×10^{-5}	10.1
J1604–4909	56682–60079	108	-37.4	6.2×10^{-4}	657.1	3.1×10^{-7}	112.2	3.1×10^{-9}	10.0
J1611–5209	51526–60137	227	-164.7	7.5×10^{-7}	122.8	1.8×10^{-3}	637.1	2.4×10^{-9}	13.3
J1613–4714	56682–60079	104	4.6	3.5×10^{-8}	171.2	-	-	1.2×10^{-8}	10.2

Table A1 – *continued*

PSR	MJD range	N_{ToA}	ΔBIC	σ_1^2 (s)	λ_1 (d)	σ_2^2 (s)	λ_2 (d)	σ_N^2 (s)	$\ln \mathcal{K}$
J1623–4256	56682–60079	106	−8.1	3.1×10^{-6}	191.6	1.7×10^{-3}	833.0	3.1×10^{-8}	9.8
J1626–4807	50941–57840	135	−49.8	2.2×10^{-5}	75.0	2.1×10^{-2}	1064.1	6.3×10^{-6}	9.2
J1627–4706	52807–56709	121	9.6	1.3×10^{-6}	183.9	-	-	7.4×10^{-7}	11.5
J1630–4733	57165–60079	86	5.8	1.6×10^{-3}	243.7	-	-	1.5×10^{-6}	10.1
J1632–4621	56682–60079	101	−12.4	2.5×10^{-3}	876.0	4.2×10^{-7}	129.5	1.0×10^{-7}	10.2
J1632–4757	51467–56709	116	0.9	9.0×10^{-3}	697.4	-	-	1.8×10^{-6}	13.6
J1632–4818	50853–58500	206	−97.3	$1.0e+01$	1384.2	1.3×10^{-4}	145.1	7.2×10^{-6}	11.9
J1633–5015	56682–60079	96	−2.1	4.2×10^{-9}	90.4	5.5×10^{-7}	500.0	3.3×10^{-9}	11.6
J1637–4553	50669–60137	302	−261.6	2.7×10^{-2}	1145.0	3.1×10^{-7}	125.1	9.2×10^{-9}	13.6
J1637–4642	54303–60137	206	−128.6	6.2×10^{-1}	806.5	3.4×10^{-6}	67.8	4.0×10^{-7}	12.9
J1638–4417	51634–60137	226	−0.4	8.8×10^{-6}	263.1	3.4×10^{-3}	3000.0	1.2×10^{-7}	13.0
J1638–4608	54221–60137	189	−114.2	9.1×10^{-5}	106.1	1.7×10^{-1}	1037.6	1.3×10^{-7}	12.2
J1640–4715	54221–60137	189	−33.7	2.9×10^{-4}	251.0	1.0	1426.4	1.1×10^{-6}	11.9
J1643–4505	54506–60162	176	−12.0	7.5×10^{-7}	73.7	8.4×10^{-5}	203.0	1.6×10^{-7}	12.0
J1644–4559	47913–60162	471	−149.1	$2.2e+01$	3000.0	2.8×10^{-2}	1045.2	3.1×10^{-4}	12.5
J1645–0317	58532–60317	58	1.5	2.1×10^{-4}	233.6	-	-	9.2×10^{-5}	7.2
J1646–4346	47913–60162	456	−518.2	$2.5e+01$	649.3	2.1	533.3	2.8×10^{-4}	13.6
J1648–3256	57277–60100	84	2.6	2.8×10^{-5}	355.3	-	-	1.1×10^{-7}	10.2
J1648–4611	51217–60137	216	0.9	$3.9e+02$	2557.9	-	-	5.7×10^{-4}	9.5
J1649–3805	52695–60079	108	9.4	1.6×10^{-6}	950.4	-	-	2.8×10^{-8}	10.6
J1649–4653	51215–59482	206	10.3	5.7×10^{-2}	586.7	-	-	5.3×10^{-6}	12.6
J1650–4502	51087–60162	222	−291.5	2.3×10^{-5}	71.5	1.1	444.8	1.7×10^{-7}	9.7
J1650–4921	52983–60137	205	−54.1	4.1×10^{-8}	80.9	5.5×10^{-4}	1903.7	2.7×10^{-8}	11.6
J1651–4246	56741–60079	107	−7.4	3.0×10^{-5}	264.2	1.3×10^{-1}	1172.0	8.8×10^{-7}	8.9
J1651–5222	56682–60079	100	8.2	1.0×10^{-4}	1089.5	-	-	3.4×10^{-8}	12.5
J1653–3838	56682–60079	105	0.5	4.4×10^{-6}	174.2	-	-	3.3×10^{-9}	11.7
J1653–4249	56682–60079	103	−19.8	4.0×10^{-7}	79.4	2.8×10^{-4}	345.8	3.2×10^{-8}	8.7
J1700–3312	56682–59517	78	8.4	8.2×10^{-7}	320.8	-	-	1.0×10^{-6}	9.0
J1701–4533	56682–60162	100	9.2	4.0×10^{-6}	482.6	-	-	4.4×10^{-8}	11.2
J1702–4128	54221–60162	191	−125.0	3.1×10^{-6}	63.6	1.8×10^{-2}	794.9	2.4×10^{-7}	12.3
J1702–4306	54506–58532	116	−20.6	9.3×10^{-3}	1078.1	1.1×10^{-5}	100.9	1.2×10^{-7}	11.0
J1703–3241	56682–60101	116	9.5	9.3×10^{-4}	2761.4	-	-	3.8×10^{-8}	11.4
J1703–4851	56682–60079	71	8.5	3.1×10^{-7}	180.8	-	-	5.9×10^{-7}	8.1
J1705–1906	51901–60101	211	−44.7	1.1×10^{-4}	869.0	1.4×10^{-16}	182.0	8.3×10^{-9}	15.5
J1705–3423	56682–60101	109	8.3	4.0×10^{-6}	154.0	-	-	1.6×10^{-8}	10.3
J1705–3950	54303–60162	189	−157.3	6.5×10^{-2}	831.0	8.9×10^{-6}	62.0	6.3×10^{-7}	10.8
J1707–4053	57166–60079	91	6.6	3.9×10^{-7}	139.3	-	-	5.6×10^{-8}	9.0
J1707–4729	51635–60079	116	6.7	1.5×10^{-3}	3000.0	-	-	1.8×10^{-8}	15.6
J1708–3426	56682–60101	105	9.3	6.0×10^{-5}	993.6	-	-	6.4×10^{-8}	12.8
J1709–1640	56741–60101	97	1.4	5.8×10^{-6}	145.6	-	-	3.8×10^{-8}	9.6
J1716–4005	57276–60162	90	8.2	2.9×10^{-4}	180.6	-	-	3.1×10^{-7}	9.5
J1717–3425	56682–60101	104	−18.9	6.1×10^{-6}	183.4	8.8×10^{-3}	673.2	2.4×10^{-8}	10.8
J1717–4054	53225–58720	93	−72.5	1.1×10^{-2}	583.9	9.8×10^{-6}	90.1	6.9×10^{-8}	6.8
J1717–5800	55974–58532	72	8.6	3.1×10^{-9}	98.0	-	-	9.3×10^{-8}	8.7
J1718–3825	50878–59609	269	−81.3	2.4×10^{-7}	289.1	3.2×10^{-1}	1736.0	1.6×10^{-8}	17.6
J1719–4006	57166–60079	93	9.1	2.0×10^{-8}	101.5	-	-	9.6×10^{-9}	11.6
J1720–2933	56682–60101	103	6.8	5.5×10^{-6}	654.1	-	-	1.4×10^{-5}	9.3
J1721–3532	51879–60163	280	−161.2	2.9×10^{-2}	943.1	2.0×10^{-6}	98.0	7.0×10^{-8}	12.4
J1722–3207	56682–60101	108	−21.0	1.6×10^{-4}	868.4	2.9×10^{-8}	138.1	4.2×10^{-9}	9.6
J1722–3632	56682–60101	101	2.6	6.2×10^{-7}	183.0	-	-	1.4×10^{-8}	11.5
J1722–3712	49044–60138	351	−539.3	1.7×10^{-1}	712.5	2.0×10^{-5}	62.0	3.4×10^{-8}	10.7
J1726–3530	50682–56709	190	−57.3	7.5	553.5	9.2×10^{-4}	143.7	1.1×10^{-5}	11.5
J1733–3716	51893–60138	217	−20.0	6.8×10^{-4}	933.8	2.2×10^{-7}	250.9	4.3×10^{-8}	14.0
J1734–3333	50686–56672	179	−0.8	5.0×10^{-2}	303.5	1.5×10^{-4}	70.0	1.5×10^{-4}	10.1
J1735–3258	54304–56672	78	5.3	8.2×10^{-4}	149.7	-	-	5.6×10^{-6}	9.7
J1737–3137	54221–59867	182	7.9	7.9×10^{-6}	83.1	-	-	6.2×10^{-7}	11.6
J1738–2955	54304–56709	82	−15.1	5.6×10^{-1}	899.8	2.9×10^{-5}	163.6	4.2×10^{-7}	12.1
J1739–2903	50739–60138	280	−64.8	7.6×10^{-5}	647.1	1.1×10^{-7}	131.7	1.1×10^{-8}	12.7
J1739–3023	51879–60138	235	−278.2	7.5×10^{-3}	691.3	1.0×10^{-5}	63.6	7.2×10^{-8}	11.9
J1739–3131	57166–60101	80	−36.6	8.8×10^{-2}	458.4	6.1×10^{-6}	93.4	3.7×10^{-8}	9.9
J1741–3927	56682–60079	97	3.6	1.3×10^{-1}	1032.2	-	-	1.1×10^{-7}	11.5

Table A1 – continued

PSR	MJD range	N_{ToA}	ΔBIC	σ_1^2 (s)	λ_1 (d)	σ_2^2 (s)	λ_2 (d)	σ_N^2 (s)	$\ln \mathcal{K}$
J1743–3150	56682-59405	74	7.6	4.3×10^{-6}	307.2	-	-	8.2×10^{-7}	10.6
J1745–3040	51901-60138	299	-21.4	8.8×10^{-2}	2443.8	1.7×10^{-7}	374.5	5.6×10^{-8}	14.7
J1749–3002	56741-60079	97	0.6	1.2×10^{-5}	124.2	-	-	2.2×10^{-7}	8.9
J1750–3157	57166-60163	71	8.5	6.2×10^{-9}	210.0	-	-	4.5×10^{-8}	7.9
J1751–4657	56682-60101	97	9.1	9.6×10^{-7}	524.4	-	-	1.5×10^{-8}	11.3
J1752–2806	56741-60101	107	-12.8	6.5×10^{-7}	62.0	1.8×10^{-4}	357.0	5.9×10^{-8}	8.6
J1757–2421	51529-60162	251	-239.7	3.1×10^{-7}	101.9	3.9×10^{-3}	1064.8	1.3×10^{-8}	13.0
J1801–2154	52135-56709	105	-22.1	5.4×10^{-2}	1353.1	2.0×10^{-5}	81.5	6.2×10^{-7}	9.3
J1806–2125	51946-60138	198	-120.1	4.9×10^{-5}	132.3	$1.4e+01$	649.0	3.0×10^{-6}	11.4
J1807–0847	56741-60101	101	4.2	2.2×10^{-9}	370.7	-	-	2.2×10^{-10}	12.2
J1816–2650	57166-60079	88	9.0	9.2×10^{-9}	282.3	-	-	1.6×10^{-7}	8.1
J1817–3618	56641-60079	96	-24.4	6.5×10^{-4}	602.5	6.3×10^{-7}	131.9	3.5×10^{-8}	9.7
J1820–0427	56603-60101	118	-38.9	3.6×10^{-7}	122.7	5.9×10^{-3}	827.3	1.0×10^{-8}	10.5
J1820–1529	54221-56709	88	8.6	1.2×10^{-2}	317.9	-	-	1.6×10^{-6}	12.1
J1822–2256	53975-59482	87	8.7	3.7×10^{-5}	1963.3	-	-	1.1×10^{-6}	9.8
J1822–4209	56641-59489	57	8.1	6.8×10^{-6}	645.5	-	-	1.0×10^{-7}	10.2
J1823–3106	56641-60101	106	-50.9	1.1×10^{-7}	133.2	4.3×10^{-3}	987.9	1.8×10^{-9}	12.1
J1824–1945	51844-60138	223	-124.0	6.8×10^{-3}	852.4	5.0×10^{-6}	172.5	1.2×10^{-9}	14.0
J1825–0935	51844-60162	255	-136.5	2.6	1322.2	1.7×10^{-3}	186.2	2.7×10^{-6}	10.2
J1825–1446	51844-60138	239	-77.1	6.0×10^{-2}	970.4	1.2×10^{-5}	180.0	3.2×10^{-7}	12.7
J1828–1057	51805-56709	121	9.6	1.4×10^{-7}	95.1	-	-	1.5×10^{-6}	12.2
J1828–1101	54221-60138	197	-101.3	5.0×10^{-6}	80.2	1.0×10^{-2}	340.3	5.4×10^{-8}	13.8
J1829–1751	56708-60101	142	-49.4	2.0×10^{-4}	290.9	8.4×10^{-7}	88.2	1.2×10^{-9}	11.7
J1830–1059	51133-60162	298	-404.8	1.7×10^{-4}	94.1	7.0	1590.7	9.4×10^{-8}	11.6
J1832–0827	51844-60138	208	-163.7	1.5×10^{-7}	104.3	9.4×10^{-3}	775.2	5.7×10^{-9}	12.8
J1833–0827	50748-60138	250	-41.5	5.2×10^{-6}	223.9	-	-	6.5×10^{-6}	14.1
J1834–0731	52003-56709	101	0.0	1.3×10^{-3}	529.0	-	-	8.9×10^{-4}	11.1
J1835–0643	51529-59489	170	-65.1	2.1×10^{-4}	290.3	9.2×10^{-1}	1487.6	6.6×10^{-7}	13.3
J1835–0944	53525-56123	57	2.5	5.5×10^{-5}	285.2	-	-	6.9×10^{-8}	12.8
J1835–1106	51844-60138	241	-256.5	2.7×10^{-5}	62.0	1.7×10^{-1}	501.4	6.7×10^{-8}	11.6
J1837–0559	54304-59489	140	-3.4	1.5×10^{-6}	185.8	1.7×10^{-4}	650.5	4.1×10^{-7}	11.6
J1837–0604	54269-56709	86	-12.6	7.5×10^{-2}	427.8	6.4×10^{-6}	62.0	9.0×10^{-7}	12.5
J1838–0453	54307-56709	87	-27.8	4.1×10^{-4}	140.6	6.6×10^{-1}	503.4	1.0×10^{-6}	11.7
J1838–0549	51692-60138	113	9.5	2.1×10^{-4}	723.6	-	-	5.8×10^{-7}	15.3
J1839–0321	54307-56709	69	-5.0	8.6×10^{-7}	128.9	2.2×10^{-3}	912.5	2.7×10^{-7}	11.7
J1839–0905	52003-55822	70	2.5	1.1×10^{-3}	304.7	-	-	3.4×10^{-7}	11.7
J1841–0345	57166-60163	86	4.9	4.2×10^{-3}	554.2	-	-	2.1×10^{-7}	15.6
J1841–0425	53423-60163	200	-68.5	1.8×10^{-7}	176.8	6.1×10^{-3}	904.5	6.2×10^{-9}	14.2
J1841–0524	54008-56709	86	8.9	2.5×10^{-6}	63.0	-	-	1.7×10^{-6}	11.3
J1842–0905	53969-60138	165	-145.0	7.4×10^{-3}	752.0	1.5×10^{-5}	103.5	4.2×10^{-8}	10.7
J1843–0702	54304-59489	159	-20.2	5.2×10^{-7}	167.7	9.9×10^{-4}	833.0	7.4×10^{-8}	11.8
J1844–0256	51559-55822	119	9.6	2.0×10^{-6}	144.0	-	-	8.4×10^{-6}	12.0
J1844–0538	51844-60138	218	-76.0	1.0×10^{-5}	287.1	6.5×10^{-2}	2259.7	4.9×10^{-8}	13.7
J1845–0434	51945-60101	203	-129.8	1.1×10^{-2}	527.6	8.5×10^{-7}	62.0	7.8×10^{-6}	8.8
J1845–0743	54304-60138	186	-13.1	3.1×10^{-10}	78.8	5.3×10^{-4}	3000.0	2.1×10^{-10}	13.1
J1847–0402	51844-60138	220	-85.6	2.5×10^{-1}	2096.1	6.7×10^{-8}	78.2	2.9×10^{-8}	12.0
J1848–0123	56741-60101	104	-1.0	2.4×10^{-7}	176.7	3.4×10^{-2}	1449.6	3.5×10^{-8}	10.5
J1852–0635	56741-60101	99	3.9	4.3×10^{-4}	579.4	-	-	4.0×10^{-7}	12.5
J1852–2610	56641-60079	84	8.9	2.0×10^{-8}	222.6	-	-	4.0×10^{-8}	8.9
J1853–0004	54307-60138	178	-37.6	1.3×10^{-3}	262.4	-	-	2.5×10^{-3}	10.6
J1853+0011	54598-56123	44	7.6	8.3×10^{-7}	179.0	-	-	4.7×10^{-7}	12.1
J1900–2600	56641-60101	104	9.3	1.4×10^{-8}	62.0	-	-	5.7×10^{-8}	6.1
J1913–0440	56741-60101	100	-10.1	3.4×10^{-8}	62.0	1.0×10^{-5}	318.2	9.1×10^{-9}	8.3
J1941–2602	56641-60101	104	7.0	2.5×10^{-8}	392.3	-	-	1.1×10^{-8}	12.4
J2048–1616	56751-60101	126	9.7	1.1×10^{-6}	359.3	-	-	5.0×10^{-8}	10.4
J2346–0609	56670-60102	93	9.1	6.9×10^{-8}	285.9	-	-	1.7×10^{-7}	9.0

Table A2. Measured pulsar rotational parameters from timing and spin-down modelling, alongside the derived magnetospheric properties.

PSR	ν (Hz)	$\dot{\nu}_{\text{weak}}$ (s ⁻²)	$\dot{\nu}_{\text{strong}}$ (s ⁻²)	$\delta\dot{\nu}$ (s ⁻²)	$\delta\rho$ (mC m ⁻³)	$\delta\rho/\rho_{\text{GJ}}$ (%)
J0034–0721	1.0605	-4.5871×10^{-16}	-4.5922×10^{-16}	5.0505×10^{19}	0.016	0.22
J0108–1431	1.2383	-1.1772×10^{-16}	-1.1874×10^{-16}	8.5542×10^{19}	0.05	1.45
J0134–2937	7.3013	-4.1775×10^{-15}	-4.178×10^{15}	3.9083×10^{19}	0.002	0.02
J0152–1637	1.2009	-1.8745×10^{-15}	-1.8748×10^{-15}	3.3516×10^{19}	0.005	0.04
J0206–4028	1.5859	-2.9555×10^{-15}	-3.0835×10^{-15}	1.28×10^{-16}	1.331	8.67
J0255–5304	2.2336	-1.557×10^{16}	-1.5597×10^{-16}	2.6776×10^{19}	0.01	0.34
J0401–7608	1.834	-5.1618×10^{-15}	-5.2151×10^{-15}	5.332×10^{-17}	0.39	2.07
J0448–2749	2.22	-7.1067×10^{-16}	-7.5614×10^{-16}	4.5471×10^{17}	0.815	12.8
J0452–1759	1.8217	-1.9068×10^{-14}	-1.9145×10^{-14}	7.6809×10^{17}	0.293	0.81
J0525+1115	2.8214	-5.8591×10^{-16}	-5.8735×10^{-16}	1.4444×10^{18}	0.025	0.49
J0543+2329	4.0655	-2.5478×10^{-13}	-2.5488×10^{-13}	1.0017×10^{16}	0.07	0.08
J0601–0527	2.5254	-8.3027×10^{-15}	-8.3106×10^{-15}	7.5536×10^{18}	0.037	0.18
J0614+2229	2.9854	-5.1985×10^{-13}	-5.296×10^{13}	9.7466×10^{15}	5.57	3.75
J0627+0706	2.1013	-1.3134×10^{-13}	-1.3173×10^{-13}	3.6394×10^{16}	0.493	0.55
J0630–2834	0.8036	-4.6181×10^{-15}	-4.6389×10^{-15}	1.5291×10^{17}	0.179	0.66
J0631+1036	3.4744	-1.2595×10^{-12}	-1.2634×10^{-12}	3.8486×10^{15}	1.31	0.61
J0659+1414	2.5979	-3.7089×10^{-13}	-3.7095×10^{-13}	4.9242×10^{17}	0.036	0.03
J0729–1448	3.9728	-1.7676×10^{-12}	-1.7854×10^{-12}	1.7791×10^{14}	4.779	2.01
J0729–1836	1.9602	-7.2595×10^{-14}	-7.2993×10^{-14}	3.965×10^{-16}	0.748	1.09
J0742–2822	5.9966	-5.9794×10^{-13}	-6.0685×10^{-13}	8.9068×10^{15}	3.349	2.98
J0745–5353	4.6547	-4.7279×10^{-14}	-4.749×10^{14}	2.1128×10^{16}	0.321	0.89
J0809–4753	1.8275	-1.0262×10^{-14}	-1.0291×10^{-14}	2.8848×10^{17}	0.15	0.56
J0820–1350	0.8077	-1.3709×10^{-15}	-1.3738×10^{-15}	2.8275×10^{18}	0.06	0.41
J0820–3826	8.0105	-1.5600×10^{-13}	-1.5735×10^{-13}	1.3516×10^{15}	0.861	1.73
J0834–4159	8.2564	-2.9175×10^{-13}	-2.9189×10^{-13}	1.3727×10^{16}	0.063	0.09
J0837–4135	1.3304	-6.2571×10^{-15}	-6.2763×10^{-15}	1.908×10^{-17}	0.149	0.61
J0842–4851	1.5519	-2.2901×10^{-14}	-2.3128×10^{-14}	2.2687×10^{16}	0.857	1.98
J0855–4644	15.4593	-1.7337×10^{-12}	-1.7359×10^{-12}	1.634×10^{-15}	0.225	0.19
J0857–4424	3.0601	-1.9595×10^{-13}	-1.9608×10^{-13}	1.2774×10^{16}	0.117	0.13
J0901–4624	2.2625	-4.4731×10^{-13}	-4.4758×10^{-13}	2.643×10^{-16}	0.187	0.12
J0904–7459	1.8197	-1.5259×10^{-15}	-1.5317×10^{-15}	3.9079×10^{18}	0.053	0.51
J0905–5127	2.8877	-2.0683×10^{-13}	-2.0873×10^{-13}	1.9038×10^{15}	1.754	1.84
J0907–5157	3.9439	-2.8438×10^{-14}	-2.8615×10^{-14}	1.7633×10^{16}	0.375	1.24
J0908–4913	9.366	-1.3239×10^{-12}	-1.3293×10^{-12}	4.0283×10^{15}	0.814	0.61
J0924–5814	1.3523	-8.7446×10^{-15}	-9.0152×10^{-15}	2.7067×10^{16}	1.772	6.19
J0940–5428	11.4227	-4.2665×10^{-12}	-4.2764×10^{-12}	8.3473×10^{15}	0.851	0.39
J0942–5552	1.5051	-5.0436×10^{-14}	-5.2212×10^{-14}	1.7389×10^{15}	4.493	6.9
J0954–5430	2.1148	-1.963×10^{13}	-1.9639×10^{-13}	8.5173×10^{17}	0.094	0.09
J1001–5507	0.6961	-2.4808×10^{-14}	-2.5122×10^{-14}	3.1417×10^{16}	1.702	2.53
J1003–4747	3.2565	-2.1958×10^{-14}	-2.1981×10^{-14}	2.3322×10^{17}	0.062	0.21
J1015–5719	7.1489	-2.9237×10^{-12}	-2.9275×10^{-12}	3.7552×10^{15}	0.585	0.26
J1016–5819	11.3851	-9.0572×10^{-14}	-9.0585×10^{-14}	1.15×10^{-17}	0.008	0.03
J1020–6026	7.1184	-3.4138×10^{-13}	-3.4145×10^{-13}	6.9517×10^{17}	0.032	0.04
J1034–3224	0.8691	-1.5292×10^{-16}	-1.9498×10^{-16}	4.2068×10^{17}	2.598	55.05
J1038–5831	1.5106	-2.8049×10^{-15}	-2.973×10^{15}	1.6809×10^{16}	1.838	11.99
J1043–6116	3.4649	-1.2488×10^{-13}	-1.2503×10^{-13}	1.3276×10^{16}	0.144	0.21
J1047–6709	5.039	-4.2818×10^{-14}	-4.2853×10^{-14}	3.504×10^{-17}	0.054	0.16
J1048–5832	8.0824	-6.176×10^{12}	-6.1995×10^{-12}	2.1044×10^{14}	2.12	0.68
J1052–5954	5.5374	-6.0966×10^{-13}	-6.1322×10^{-13}	3.56×10^{-15}	1.379	1.17
J1055–6022	1.0553	-1.0271×10^{-13}	-1.0277×10^{-13}	5.7855×10^{17}	0.125	0.11
J1055–6028	10.034	-2.9598×10^{-12}	-2.9729×10^{-12}	1.2763×10^{14}	1.667	0.86
J1056–6258	2.3671	-1.9923×10^{-14}	-2.0237×10^{-14}	3.1372×10^{16}	1.028	3.15
J1057–5226	5.0732	-1.4993×10^{-13}	-1.5033×10^{-13}	3.9877×10^{16}	0.326	0.53
J1105–6107	15.8223	-3.9081×10^{-12}	-4.0351×10^{-12}	9.8551×10^{14}	8.922	5.05
J1112–6103	15.3936	-7.3823×10^{-12}	-7.4089×10^{-12}	2.6588×10^{14}	1.776	0.72
J1115–6052	3.8494	-1.0702×10^{-13}	-1.0716×10^{-13}	1.4218×10^{16}	0.158	0.27
J1123–6259	3.6841	-7.1235×10^{-14}	-7.1838×10^{-14}	6.0311×10^{16}	0.838	1.69
J1136–5525	2.7419	-6.1508×10^{-14}	-6.204×10^{14}	4.8972×10^{16}	0.849	1.59
J1138–6207	8.506	-9.0165×10^{-13}	-9.0456×10^{-13}	2.9117×10^{15}	0.749	0.65
J1146–6030	3.658	-2.3903×10^{-14}	-2.3903×10^{14}	4.0681×10^{17}	0.098	0.34
J1156–5707	3.4672	-3.1681×10^{-13}	-3.2061×10^{-13}	3.8013×10^{15}	2.582	2.4

Table A2 – continued

PSR	ν (Hz)	$\dot{\nu}_{\text{weak}}$ (s^{-2})	$\dot{\nu}_{\text{strong}}$ (s^{-2})	$\delta\dot{\nu}$ (s^{-2})	$\delta\rho$ (mC m^{-3})	$\delta\rho/\rho_{\text{GJ}}$ (%)
J1157–6224	2.4967	-2.448×10^{14}	-2.453×10^{14}	4.9665×10^{17}	0.143	0.41
J1216–6223	2.6734	-1.2023×10^{-13}	-1.2025×10^{-13}	1.4214×10^{17}	0.018	0.02
J1224–6407	4.6194	-1.0564×10^{-13}	-1.0576×10^{-13}	1.1901×10^{16}	0.121	0.23
J1243–6423	2.5741	-2.9739×10^{-14}	-2.9853×10^{-14}	1.049×10^{-16}	0.27	0.71
J1248–6344	5.042	-4.2978×10^{-13}	-4.3015×10^{-13}	3.6747×10^{16}	0.178	0.17
J1305–6203	2.3377	-1.7571×10^{-13}	-1.7576×10^{-13}	5.6284×10^{17}	0.063	0.06
J1306–6617	2.114	-2.6671×10^{-14}	-2.6813×10^{-14}	1.4216×10^{16}	0.426	1.07
J1317–6302	3.8275	-1.396×10^{15}	-1.4947×10^{-15}	9.8733×10^{17}	0.962	14.15
J1319–6056	3.5168	-1.8858×10^{-14}	-1.8905×10^{-14}	4.7041×10^{17}	0.13	0.5
J1320–5359	3.5748	-1.1803×10^{-13}	-1.1833×10^{-13}	2.9848×10^{16}	0.327	0.51
J1326–5859	2.0921	-1.4096×10^{-14}	-1.4351×10^{-14}	2.5478×10^{16}	1.056	3.62
J1326–6408	1.2616	-4.9128×10^{-15}	-4.9315×10^{-15}	1.8177×10^{17}	0.164	0.74
J1326–6700	1.8416	-1.7764×10^{-14}	-1.8186×10^{-14}	4.2165×10^{16}	1.66	4.75
J1327–6222	1.887	-6.6467×10^{-14}	-6.742×10^{14}	9.5326×10^{16}	1.916	2.87
J1327–6301	5.0896	-3.9625×10^{-14}	-3.9635×10^{-14}	7.8622×10^{18}	0.012	0.04
J1327–6400	3.5628	-4.0041×10^{-13}	-4.0493×10^{-13}	3.5622×10^{15}	2.123	1.78
J1328–4357	1.8772	-1.0639×10^{-14}	-1.0786×10^{-14}	1.469×10^{-16}	0.74	2.76
J1338–6204	0.8071	-8.9618×10^{-15}	-8.9927×10^{-15}	3.0887×10^{17}	0.259	0.69
J1340–6456	2.6412	-3.5121×10^{-14}	-3.5345×10^{-14}	2.2125×10^{16}	0.517	1.26
J1349–6130	3.8556	-7.5795×10^{-14}	-7.6343×10^{-14}	4.8963×10^{16}	0.645	1.29
J1352–6803	1.5901	-3.1004×10^{-15}	-3.1333×10^{-15}	2.7853×10^{17}	0.282	1.8
J1357–62	2.1941	-7.0788×10^{-14}	-7.0865×10^{-14}	7.6457×10^{17}	0.138	0.22
J1359–6038	7.8426	-3.8912×10^{-13}	-3.9031×10^{-13}	1.1892×10^{15}	0.485	0.61
J1401–6357	1.1865	-2.3534×10^{-14}	-2.4091×10^{-14}	5.5759×10^{16}	2.376	4.74
J1412–6145	3.172	-9.9014×10^{-13}	-9.9113×10^{-13}	9.8202×10^{16}	0.394	0.2
J1418–3921	0.9117	-7.3019×10^{-16}	-7.4512×10^{-16}	1.01×10^{-17}	0.279	2.77
J1424–5822	2.7268	-2.9172×10^{-14}	-2.9525×10^{-14}	3.5319×10^{16}	0.892	2.42
J1428–5530	1.7535	-6.4118×10^{-15}	-6.4205×10^{-15}	8.7534×10^{18}	0.059	0.27
J1430–6623	1.2732	-4.5025×10^{-15}	-4.5057×10^{-15}	3.1709×10^{18}	0.03	0.14
J1435–5954	2.1142	-6.8705×10^{-15}	-6.9841×10^{-15}	1.1361×10^{16}	0.671	3.31
J1452–5851	2.5864	-3.3914×10^{-13}	-3.3921×10^{-13}	7.0226×10^{17}	0.053	0.04
J1452–6036	6.4519	-6.0295×10^{-14}	-6.0401×10^{-14}	1.0611×10^{16}	0.121	0.35
J1453–6413	5.5714	-8.5164×10^{-14}	-8.5231×10^{-14}	3.9409×10^{17}	0.041	0.09
J1456–6843	3.7968	-1.4237×10^{-15}	-1.4273×10^{-15}	3.5961×10^{18}	0.035	0.51
J1509–5850	11.2454	-1.1591×10^{-12}	-1.1592×10^{-12}	7.655×10^{-17}	0.015	0.01
J1512–5759	7.7701	-4.1315×10^{-13}	-4.1427×10^{-13}	1.1244×10^{15}	0.447	0.54
J1513–5908	6.5971	-6.653×10^{11}	-6.6533×10^{-11}	2.4287×10^{15}	0.083	0.01
J1514–5925	6.7205	-1.2933×10^{-13}	-1.3057×10^{-13}	1.2387×10^{15}	0.946	1.92
J1515–5720	3.4886	-7.3891×10^{-14}	-7.4241×10^{-14}	3.269×10^{-16}	0.458	0.89
J1522–5829	2.5294	-1.3148×10^{-14}	-1.3195×10^{-14}	2.9992×10^{17}	0.117	0.46
J1524–5706	0.8959	-2.8601×10^{-13}	-2.8606×10^{-13}	4.2224×10^{17}	0.059	0.03
J1530–5327	3.5848	-6.0115×10^{-14}	-6.0197×10^{-14}	7.1428×10^{17}	0.11	0.24
J1534–5405	3.452	-1.8179×10^{-14}	-1.8717×10^{-14}	4.382×10^{-16}	1.245	4.82
J1536–5433	1.1345	-2.3199×10^{-15}	-2.3534×10^{-15}	3.3453×10^{17}	0.464	2.89
J1538–5551	9.5533	-2.9263×10^{-13}	-2.928×10^{13}	1.7048×10^{16}	0.073	0.12
J1539–5626	4.1085	-8.1444×10^{-14}	-8.2126×10^{-14}	6.8221×10^{16}	0.84	1.68
J1541–5535	3.3802	-8.3736×10^{-13}	-8.4471×10^{-13}	7.1155×10^{15}	3.011	1.7
J1543–5459	2.6516	-3.6452×10^{-13}	-3.6907×10^{-13}	4.5505×10^{15}	3.295	2.5
J1544–5308	5.6006	-1.8893×10^{-15}	-1.8941×10^{-15}	4.7607×10^{18}	0.033	0.5
J1548–5607	5.8501	-3.6702×10^{-13}	-3.6773×10^{-13}	7.0599×10^{16}	0.343	0.38
J1549–4848	3.4679	-1.6938×10^{-13}	-1.7015×10^{-13}	7.7358×10^{16}	0.719	0.91
J1551–5310	2.2053	-9.4577×10^{-13}	-9.5164×10^{-13}	5.4035×10^{15}	2.664	1.14
J1557–4258	3.0378	-3.0261×10^{-15}	-3.0617×10^{-15}	3.5639×10^{17}	0.265	2.36
J1559–4438	3.8902	-1.5411×10^{-14}	-1.5456×10^{-14}	4.4411×10^{17}	0.129	0.58
J1600–5044	5.192	-1.3631×10^{-13}	-1.3666×10^{-13}	3.5436×10^{16}	0.3	0.52
J1600–5751	5.1426	-5.6095×10^{-14}	-5.6434×10^{-14}	3.289×10^{-16}	0.436	1.17
J1601–5335	3.4665	-7.4863×10^{-13}	-7.4994×10^{-13}	1.309×10^{-15}	0.578	0.35
J1602–5100	1.157	-8.9147×10^{-14}	-9.3511×10^{-14}	4.3637×10^{15}	9.673	9.79
J1604–4909	3.0542	-9.3794×10^{-15}	-9.5886×10^{-15}	2.0111×10^{16}	0.846	4.29
J1611–5209	5.4796	-1.5507×10^{-13}	-1.5558×10^{-13}	5.1511×10^{16}	0.398	0.66
J1613–4714	2.6152	-4.3278×10^{-15}	-4.3429×10^{-15}	1.1328×10^{17}	0.076	0.52

Table A2 – *continued*

PSR	ν (Hz)	$\dot{\nu}_{\text{weak}}$ (s^{-2})	$\dot{\nu}_{\text{strong}}$ (s^{-2})	$\delta\dot{\nu}$ (s^{-2})	$\delta\rho$ (mC m^{-3})	$\delta\rho/\rho_{\text{GJ}}$ (%)
J1623–4256	2.7428	-7.5156×10^{-15}	-7.6712×10^{-15}	1.4618×10^{16}	0.725	3.89
J1626–4807	3.4022	-2.0101×10^{-13}	-2.0352×10^{-13}	2.0203×10^{15}	1.739	2.01
J1627–4706	7.105	-8.7275×10^{-14}	-8.7434×10^{-14}	1.5946×10^{16}	0.144	0.37
J1630–4733	1.7362	-6.7028×10^{-14}	-6.7759×10^{-14}	7.3111×10^{16}	1.526	2.18
J1632–4621	0.5851	-2.5973×10^{-14}	-2.6009×10^{-14}	3.2841×10^{17}	0.19	0.25
J1632–4757	4.3751	-2.8825×10^{-13}	-2.8868×10^{-13}	4.3366×10^{16}	0.275	0.3
J1632–4818	1.229	-9.7969×10^{-13}	-9.8162×10^{-13}	1.7697×10^{15}	1.148	0.36
J1633–5015	2.8397	-3.0542×10^{-14}	-3.0559×10^{-14}	1.7368×10^{17}	0.042	0.11
J1637–4553	8.4194	-2.2584×10^{-13}	-2.2643×10^{-13}	5.8993×10^{16}	0.305	0.52
J1637–4642	6.4915	-2.4969×10^{-12}	-2.5007×10^{-12}	3.8041×10^{15}	0.673	0.3
J1638–4417	8.4888	-1.1551×10^{-13}	-1.1587×10^{-13}	3.6137×10^{16}	0.26	0.63
J1638–4608	3.5951	-6.6285×10^{-13}	-6.6677×10^{-13}	3.9201×10^{15}	1.808	1.18
J1640–4715	1.9326	-1.5676×10^{-13}	-1.5761×10^{-13}	7.8772×10^{16}	1.019	1.01
J1643–4505	4.2125	-5.6415×10^{-13}	-5.6527×10^{-13}	1.1235×10^{15}	0.519	0.4
J1644–4559	2.1974	-9.6662×10^{-14}	-9.7236×10^{-14}	5.0387×10^{16}	0.778	1.04
J1646–4346	4.3177	-2.0729×10^{-12}	-2.0887×10^{-12}	1.4498×10^{14}	3.45	1.4
J1648–3256	1.3899	-6.7771×10^{-15}	-6.8167×10^{-15}	3.1028×10^{17}	0.228	0.92
J1648–4611	6.0622	-8.6688×10^{-13}	-8.7342×10^{-13}	6.4177×10^{15}	1.993	1.48
J1649–3805	3.8164	-5.1895×10^{-16}	-5.2105×10^{-16}	1.9137×10^{18}	0.031	0.74
J1649–4653	1.7952	-1.5945×10^{-13}	-1.6037×10^{-13}	8.2232×10^{16}	1.094	1.03
J1650–4502	2.6256	-1.0818×10^{-13}	-1.1329×10^{-13}	5.1148×10^{15}	6.833	9.46
J1650–4921	6.3939	-7.4222×10^{-14}	-7.4437×10^{-14}	1.5966×10^{16}	0.165	0.43
J1651–4246	1.1847	-6.6197×10^{-15}	-6.8316×10^{-15}	2.1194×10^{16}	1.704	6.41
J1651–5222	1.5747	-4.4853×10^{-15}	-4.4926×10^{-15}	7.1664×10^{18}	0.061	0.32
J1653–3838	3.2783	-2.988×10^{14}	-3.0022×10^{-14}	1.4211×10^{16}	0.323	0.95
J1653–4249	1.6325	-1.2529×10^{-14}	-1.2791×10^{-14}	2.3855×10^{16}	1.187	3.81
J1700–3312	0.7362	-2.5514×10^{-15}	-2.5559×10^{-15}	4.1557×10^{18}	0.068	0.33
J1701–4533	3.0969	-4.9632×10^{-15}	-4.9899×10^{-15}	2.1358×10^{17}	0.123	0.86
J1702–4128	5.4904	-1.5756×10^{-12}	-1.5782×10^{-12}	2.6196×10^{15}	0.634	0.33
J1702–4306	4.6402	-2.0983×10^{-13}	-2.111×10^{13}	1.2769×10^{15}	0.921	1.22
J1703–3241	0.8252	-4.4661×10^{-16}	-4.4837×10^{-16}	1.7183×10^{18}	0.064	0.77
J1703–4851	0.7161	-2.5965×10^{-15}	-2.6045×10^{-15}	6.6199×10^{18}	0.109	0.51
J1705–1906	3.3446	-4.627×10^{14}	-4.6289×10^{-14}	1.3092×10^{17}	0.024	0.06
J1705–3423	3.915	-1.6305×10^{-14}	-1.6629×10^{-14}	2.8954×10^{16}	0.816	3.55
J1705–3950	3.1354	-5.9293×10^{-13}	-5.9714×10^{-13}	4.2105×10^{15}	2.198	1.42
J1707–4053	1.7211	-5.6559×10^{-15}	-5.7037×10^{-15}	4.7783×10^{17}	0.345	1.69
J1707–4729	3.7527	-2.1972×10^{-14}	-2.1979×10^{-14}	7.3461×10^{18}	0.018	0.07
J1708–3426	1.4448	-8.7795×10^{-15}	-8.7862×10^{-15}	6.7553×10^{18}	0.043	0.15
J1709–1640	1.5313	-1.4749×10^{-14}	-1.4868×10^{-14}	1.1833×10^{16}	0.561	1.61
J1716–4005	3.2071	-2.8613×10^{-14}	-2.9863×10^{-14}	$1.25e \times 10^{-15}$	2.938	8.74
J1717–3425	1.5237	-2.2604×10^{-14}	-2.2856×10^{-14}	2.2579×10^{16}	0.866	2.0
J1717–4054	1.1265	-4.4306×10^{-15}	-4.9122×10^{-15}	4.8165×10^{16}	4.854	21.75
J1717–5800	3.1076	-1.8488×10^{-15}	-1.8523×10^{-15}	3.4177×10^{18}	0.032	0.37
J1718–3825	13.3914	-2.3627×10^{-12}	-2.3636×10^{-12}	9.1493×10^{16}	0.116	0.08
J1719–4006	5.2884	-4.6593×10^{-14}	-4.6663×10^{-14}	6.9322×10^{17}	0.099	0.3
J1720–2933	1.6117	-1.9367×10^{-15}	-1.9392×10^{-15}	2.3531×10^{18}	0.03	0.24
J1721–3532	3.566	-3.1988×10^{-13}	-3.2066×10^{-13}	7.8186×10^{16}	0.521	0.49
J1722–3207	2.0957	-2.8021×10^{-15}	-2.8389×10^{-15}	3.6735×10^{17}	0.341	2.62
J1722–3632	2.5051	-2.8014×10^{-14}	-2.8052×10^{-14}	3.7386×10^{17}	0.1	0.27
J1722–3712	4.2341	-1.9201×10^{-13}	-1.9621×10^{-13}	4.1921×10^{15}	3.31	4.37
J1726–3530	0.9008	-9.8133×10^{-13}	-9.8653×10^{-13}	4.8357×10^{15}	3.662	0.99
J1733–3716	2.9621	-1.3198×10^{-13}	-1.3203×10^{-13}	5.5262×10^{17}	0.063	0.08
J1734–3333	0.8552	-1.6653×10^{-12}	-1.6682×10^{-12}	2.9033×10^{15}	1.732	0.35
J1735–3258	2.8492	-2.0957×10^{-13}	-2.1224×10^{-13}	2.6726×10^{15}	2.462	2.55
J1737–3137	2.2201	-6.8267×10^{-13}	-6.8359×10^{-13}	9.1501×10^{16}	0.529	0.27
J1738–2955	2.2552	-4.1667×10^{-13}	-4.1788×10^{-13}	1.1906×10^{15}	0.874	0.57
J1739–2903	3.0971	-7.5489×10^{-14}	-7.5591×10^{-14}	1.0192×10^{16}	0.15	0.27
J1739–3023	8.7434	-8.6644×10^{-13}	-8.7565×10^{-13}	9.2074×10^{15}	2.382	2.13
J1739–3131	1.8888	-6.5508×10^{-14}	-6.6769×10^{-14}	9.1904×10^{16}	1.86	2.81
J1741–3927	1.9523	-6.3577×10^{-15}	-6.5699×10^{-15}	1.6451×10^{16}	1.051	5.18
J1743–3150	0.4141	-2.0711×10^{-14}	-2.0717×10^{-14}	4.9927×10^{18}	0.038	0.05

Table A2 – continued

PSR	ν (Hz)	$\dot{\nu}_{\text{weak}}$ (s^{-2})	$\dot{\nu}_{\text{strong}}$ (s^{-2})	$\delta\dot{\nu}$ (s^{-2})	$\delta\rho$ (mC m^{-3})	$\delta\rho/\rho_{\text{GJ}}$ (%)
J1745–3040	2.7216	-7.9006×10^{-14}	-7.9055×10^{-14}	4.7583×10^{17}	0.073	0.12
J1749–3002	1.6397	-2.1035×10^{-14}	-2.1327×10^{-14}	2.9123×10^{16}	1.116	2.77
J1750–3157	1.0985	-2.365×10^{16}	-2.3735×10^{-16}	8.4797×10^{19}	0.037	0.72
J1751–4657	1.3471	-2.3532×10^{-15}	-2.3561×10^{-15}	2.9172×10^{18}	0.037	0.25
J1752–2806	1.7776	-2.55×10^4	-2.5828×10^{-14}	3.2806×10^{16}	1.097	2.57
J1757–2421	4.2716	-2.355×10^{13}	-2.3582×10^{-13}	3.1374×10^{16}	0.223	0.27
J1801–2154	2.6645	-1.1279×10^{-13}	-1.1432×10^{-13}	1.4381×10^{15}	1.868	2.55
J1806–2125	2.0754	-4.8311×10^{-13}	-4.8981×10^{-13}	6.0082×10^{15}	4.272	2.49
J1807–0847	6.1077	-1.0678×10^{-15}	-1.0697×10^{-15}	1.8946×10^{18}	0.017	0.36
J1816–2650	1.6867	-1.8941×10^{-16}	-1.9001×10^{-16}	5.9559×10^{19}	0.024	0.63
J1817–3618	2.5838	-1.3469×10^{-14}	-1.3681×10^{-14}	2.1179×10^{16}	0.808	3.15
J1820–0427	1.672	-1.7633×10^{-14}	-1.7783×10^{-14}	1.4933×10^{16}	0.619	1.69
J1820–1529	3.0007	-3.3998×10^{-13}	-3.4206×10^{-13}	2.0828×10^{15}	1.468	1.23
J1822–2256	0.5335	-3.8464×10^{-16}	-3.8506×10^{-16}	3.6081×10^{19}	0.018	0.19
J1822–4209	2.1905	-2.1905×10^{-15}	-2.1989×10^{-15}	7.4666×10^{18}	0.077	0.68
J1823–3106	3.5205	-3.6254×10^{-14}	-3.6393×10^{-14}	1.3739×10^{16}	0.274	0.76
J1824–1945	5.2816	-1.456×10^{13}	-1.4644×10^{-13}	8.3885×10^{16}	0.681	1.15
J1825–0935	1.3004	-8.6322×10^{-14}	-8.9039×10^{-14}	2.5583×10^{15}	5.436	5.93
J1825–1446	3.5817	-2.9057×10^{-13}	-2.9108×10^{-13}	5.0776×10^{16}	0.354	0.35
J1828–1057	4.0595	-3.4108×10^{-13}	-3.4115×10^{-13}	6.2208×10^{17}	0.038	0.04
J1828–1101	13.878	-2.8475×10^{-12}	-2.8564×10^{-12}	8.9229×10^{15}	1.011	0.63
J1829–1751	3.2559	-5.8497×10^{-14}	-5.9055×10^{-14}	5.4767×10^{16}	0.893	1.87
J1830–1059	2.4687	-3.6361×10^{-13}	-3.6695×10^{-13}	3.3458×10^{15}	2.514	1.84
J1832–0827	1.5448	-1.5245×10^{-13}	-1.5255×10^{-13}	9.736×10^{-17}	0.143	0.13
J1833–0827	11.725	-1.2615×10^{-12}	-1.2617×10^{-12}	2.0269×10^{16}	0.038	0.03
J1834–0731	1.9493	-2.2114×10^{-13}	-2.2126×10^{-13}	8.2658×10^{17}	0.09	0.07
J1835–0643	3.2698	-4.3174×10^{-13}	-4.3257×10^{-13}	8.364×10^{-16}	0.501	0.39
J1835–0944	6.8801	-2.0749×10^{-13}	-2.0778×10^{-13}	2.2544×10^{16}	0.134	0.22
J1835–1106	6.0271	-7.4596×10^{-13}	-7.5692×10^{-13}	8.7082×10^{15}	2.924	2.34
J1837–0559	4.9735	-8.1746×10^{-14}	-8.1943×10^{-14}	1.9722×10^{16}	0.22	0.48
J1837–0604	10.3828	-4.8529×10^{-12}	-4.8668×10^{-12}	9.8949×10^{15}	0.992	0.41
J1838–0453	2.6256	-7.9762×10^{-13}	-8.0456×10^{-13}	6.9416×10^{15}	3.415	1.74
J1838–0549	4.2497	-6.0355×10^{-13}	-6.0363×10^{-13}	6.6549×10^{17}	0.03	0.02
J1839–0321	4.1879	-2.1939×10^{-13}	-2.1968×10^{-13}	2.9832×10^{16}	0.222	0.27
J1839–0905	2.3868	-1.4798×10^{-13}	-1.4839×10^{-13}	2.6045×10^{16}	0.312	0.35
J1841–0345	4.9003	-1.3893×10^{-12}	-1.3898×10^{-12}	2.8099×10^{16}	0.077	0.04
J1841–0425	5.372	-1.8437×10^{-13}	-1.8469×10^{-13}	3.1555×10^{16}	0.226	0.34
J1841–0524	2.2431	-1.1738×10^{-12}	-1.1747×10^{-12}	8.8739×10^{16}	0.389	0.15
J1842–0905	2.9015	-8.7605×10^{-14}	-8.8953×10^{-14}	1.3483×10^{15}	1.904	3.08
J1843–0702	5.2188	-5.8071×10^{-14}	-5.8267×10^{-14}	1.9636×10^{16}	0.254	0.68
J1844–0256	3.6635	-3.8307×10^{-13}	-3.832×10^{13}	1.245×10^{-16}	0.075	0.07
J1844–0538	3.9108	-1.4834×10^{-13}	-1.4852×10^{-13}	1.7892×10^{16}	0.167	0.24
J1845–0434	2.0544	-4.7375×10^{-14}	-4.8011×10^{-14}	5.4168×10^{16}	1.236	2.29
J1845–0743	9.5516	-3.3442×10^{-14}	-3.3466×10^{-14}	2.4427×10^{17}	0.031	0.15
J1847–0402	1.6728	-1.4461×10^{-13}	-1.4471×10^{-13}	1.0355×10^{16}	0.15	0.14
J1848–0123	1.5165	-1.1931×10^{-14}	-1.1998×10^{-14}	6.3189×10^{17}	0.334	1.06
J1852–0635	1.9078	-5.3211×10^{-14}	-5.3258×10^{-14}	4.569×10^{-17}	0.102	0.17
J1852–2610	2.9732	-7.6642×10^{-16}	-7.7192×10^{-16}	5.022×10^{-18}	0.075	1.31
J1853–0004	9.8583	-5.4024×10^{-13}	-5.4225×10^{-13}	1.6194×10^{15}	0.5	0.6
J1853+0011	2.5133	-2.1176×10^{-13}	-2.1181×10^{-13}	1.9095×10^{17}	0.019	0.02
J1900–2600	1.6334	-5.3591×10^{-16}	-5.6064×10^{-16}	2.2679×10^{17}	0.546	8.47
J1913–0440	1.2107	-5.9338×10^{-15}	-5.9989×10^{-15}	6.5064×10^{17}	0.546	2.19
J1941–2602	2.4823	-5.8932×10^{-15}	-5.8951×10^{-15}	1.9036×10^{18}	0.011	0.06
J2048–1616	0.5098	-2.8466×10^{-15}	-2.8515×10^{-15}	3.6578×10^{18}	0.068	0.26
J2346–0609	0.8464	-9.7661×10^{-16}	-9.7826×10^{-16}	1.6473×10^{18}	0.041	0.34

Table A3. Transient spin-down event properties and inferred asteroid masses.

PSR	$ \delta\dot{\nu} $ (10^{-16} s $^{-2}$)	Δt (d)	m (10^{12} g)
J0627+0706	2.877	4153	87.92
-	2.575	889	16.85
J0729-1836	3.166	1462	45.79
-	2.769	296	8.11
J0809-4753	0.233	1385	8.49
-	0.108	524	1.49
-	0.174	518	2.37
J0820-1350	0.02	631	0.89
J0842-4851	0.499	331	2.91
-	0.676	643	7.65
-	1.232	516	11.19
J1123-6259	4.01	569	22.82
J1156-5707	25.04	2348	277.85
J1340-6456	0.608	226	1.95
-	1.739	301	7.44
-	1.814	304	7.84
J1401-6357	2.16	636	23.83
-	4.08	867	61.36
J1412-6145	3.3	1159	10.23
-	7.17	3385	64.91
J1539-5626	4.26	527	20.95
-	3.16	536	15.81
-	4.06	446	16.9
-	2.958	161	4.44
-	4.68	939	41.01
-	3.19	411	12.24
J1541-5535	57.3	509	84.1
-	55.2	1059	168.57
-	26.2	502	37.93
-	26.1	311	23.41
J1602-5100	10.7	625	58.57
-	13.0	624	71.04
-	42.0	958	352.39
-	11.8	538	55.6
J1604-4909	1.447	1351	53.54
-	1.799	968	47.69
J1632-4818	9.19	297	7.36
J1733-3716	0.137	488	0.49
-	0.191	716	1.0
-	0.344	692	1.75
-	0.216	1497	2.38
-	0.183	1619	2.18
J1734-3333	18.37	275	10.45
-	11.01	185	4.21
J1806-2125	16.2	638	38.71
-	8.9	305	10.17
-	9.9	585	21.69
-	46.6	1732	302.26
J1820-0427	0.962	959	18.52
J1820-1529	12.04	508	27.95
-	17.88	556	45.43
J1825-0935	20.44	426	78.13
-	6.04	309	16.75
-	7.3	268	17.55
-	9.62	285	24.6
J1833-0827	0.419	460	0.46
-	0.238	459	0.26
-	0.489	544	0.63
-	0.43	834	0.85
J1835-0643	6.88	4501	125.71
J1838-0453	46.7	469	65.3

Table A3 – continued

PSR	$\delta\dot{\nu}$ (10^{-16} s $^{-2}$)	Δt (d)	m (10^{12} g)
J1841-0345	4.61	2858	29.84
J1845-0434	4.33	879	46.47
-	2.14	542	14.16
-	2.12	911	23.58
-	0.88	296	3.18
-	4.98	1002	60.93
-	2.4	648	18.99